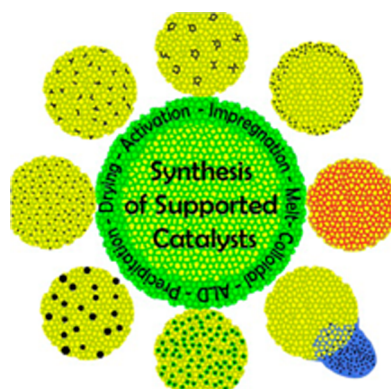


Recent Developments in the Synthesis of Supported Catalysts

Peter Munnik, Petra E. de Jongh, and Krijn P. de Jong*

Inorganic Chemistry and Catalysis, Debye Institute for Nanomaterials Science, Utrecht University, Universiteitsweg 99, 3584 CG Utrecht, The Netherlands



CONTENTS

1. Introduction	6687
2. Catalyst Requirements	6688
3. Precipitation	6689
3.1. Coprecipitation	6689
3.1.1. "Greener" Coprecipitation Methods	6691
3.2. Deposition Precipitation	6691
3.2.1. Gold Catalysts	6692
4. Impregnation and Drying	6693
4.1. Impregnation	6693
4.1.1. Pore Filling	6694
4.2. Adsorption	6694
4.2.1. Outer and Inner Sphere Complex Formation	6695
4.2.2. Metal Distribution	6697
4.3. Drying	6699
4.3.1. Drying of Strongly or Weakly Adsorbing Species	6699
4.3.2. Metal Redistribution at the Nanoscale	6700
4.3.3. Alternative Drying Methods	6701
4.4. Activation	6702
4.4.1. Formation of the Active Phase	6702
4.4.2. Chelating Additives and Other Organic-Containing Precursors	6704
4.4.3. Plasma Activation	6705
5. Emerging Techniques	6706
5.1. Melt Infiltration	6706
5.2. Colloidal Synthesis	6708
5.3. Atomic Layer Deposition	6710
5.3.1. ALD for Nanoparticle Stabilization	6711
6. Conclusion and Outlook	6713
Author Information	6713
Corresponding Author	6713
Notes	6713
Biographies	6713
Acknowledgments	6714
References	6714

1. INTRODUCTION

Heterogeneous catalysis, whereby a gas- or liquid-phase reaction is performed over a solid catalyst, is at the heart of the modern energy and chemical industries. Most chemical processes, both established^{1–3} and emerging,^{4–7} are performed using functional nanomaterials as catalysts. Moreover, upcoming fields such as nanoelectronics and energy conversion and storage are based upon the application of similar nanomaterials. The catalytic activity for these materials often resides with metal (oxide, sulfide) surface sites, and efficient use of the metals and space available requires small particles, located on a mostly inert support to enhance the thermal stability of the catalyst. The field of catalyst synthesis, also known as catalyst preparation or catalyst manufacturing, aims at establishing the desired composition and structure of these materials.

Market studies in 2013 have estimated the total sales of catalysts to be between \$15 and \$19 billion per year, and to rise 4–5% per year.^{8,9} Moreover, the added value catalysts create in the conversion of feedstocks to products such as fuels and chemicals is much larger. Studies have estimated that the cost of the catalyst only represents between 0.1% and 1% of the final product margin, meaning that the total value the catalysis-based industry creates can be estimated to be on the order of trillions of dollars per year.^{10,11} Even so, catalyst synthesis has often been regarded as an art rather than a science, although an exponential increase in the number of scientific papers on supported catalysts testifies to the increased ability to rationally synthesize active, selective, and stable catalysts.¹² Despite this, many of the fundamental mechanisms concerning catalyst synthesis are as yet not fully understood. For example, a recent review highlights the lack of knowledge on the mechanisms and rates of particle formation in supported catalyst synthesis.¹³ Moreover, heterogeneous catalysts for a wide variety of reactions, such as biomass conversion, (de)hydrogenation and oxidation, the Fischer–Tropsch synthesis, ammonia synthesis, deNO_x, hydrodesulfurization, and others, encounter challenges during preparation, activation, and operational use. While very small metal particles are generally desired, the formation of poorly reducible compounds such as transition-metal silicates, aluminates, and titanates often prevents complete reduction of the precursor to the active phase, so that the costly metal is not fully utilized. Alternatively, the particles may be in close proximity to each other, resulting in significant particle growth during operation. During the synthesis of bimetallic or promoted systems, phase segregation or preferential deposition may result in separated phases or one metal covered by the other where an alloy was desired, while macroscopic nonuniform distributions may prevent optional use of the catalyst.

Received: August 29, 2014

Published: June 19, 2015

In this review, we describe recent developments in the synthesis of supported catalysts reported over the past 5–10 years. First, the main requirements of solid catalysts are discussed. Next, recent developments of the two main preparation methods used in industry, precipitation and impregnation, are highlighted. In both of these methods, a metal precursor, mostly an inorganic salt, is the starting point to deposit the active metal onto the support. With precipitation techniques, metal particle growth is induced by supersaturation of the precursor solution, resulting in nucleation and growth of metal particles. This can happen in conjunction with the formation of the support (coprecipitation) or on an existing support (deposition precipitation). With impregnation techniques, the support is contacted with a precursor solution. Low loadings, often for precious metals, are achieved by adsorption of the precursor molecules onto surface groups of the support (ion adsorption) or through the exchange of ions in, for example, zeolites (ion exchange), after which excess precursor is removed. When higher loadings are required, the washing step is skipped and the support is directly dried, so that all precursor ends up on the support (impregnation and drying). Impregnation can be performed to incipient wetness, whereby only the pores of the support are filled with precursor solution, to prevent deposition on the external surface of the catalyst grains and to limit waste. Besides progress in understanding these traditional methods, emerging preparation techniques are discussed in this review. Precursors with low melting points can be heated and contacted directly with the support, such that capillary forces suck up the precursor upon melting (melt infiltration). Particles can also be formed in solution (colloidal route) controlled through use of stabilizing agents or ligands, after which the formed particles are deposited on a support. Vapor deposition involves gaseous metal atoms, clusters, or organics selectively reacting with support surface groups. Finally, we provide an outlook on the anticipated developments in the field of supported catalyst synthesis.

2. CATALYST REQUIREMENTS

Catalysts come in a wide variety to accommodate the large differences in operating conditions, feedstocks, and products, and the catalytically active metals can be deposited on a range of supports, which are generally highly porous and can vary in size from small powders to centimeter-sized pellets. In each case, high activities and selectivities toward the desired products are required. Moreover, the stability of the catalyst is highly important, and processes such as the irreversible growth of particles or poisoning of the active sites have to be prevented.¹⁴ The performance and stability of the catalyst are determined by what we refer to as the “DNA” of the catalyst, that is, the density, nature, and accessibility of the active sites, with the accessibility largely determined by the support pore architecture.

The density of active sites is important to the activity primarily through the number of particles on the support connected to the metal loading. Since industrial reactors are generally limited in size for practical reasons, it is often desirable to use a high density of active sites (high metal loading) to maximize the activity per unit volume. The local particle density, and therefore the distance between particles, can also be important for the stability of the catalysts. Maximizing the spacing between Cu particles proved highly beneficial for the stability of methanol catalysts.¹⁵ Similarly, reducing the size of aggregates of cobalt nanoparticles on silica

gel in Fischer–Tropsch catalysts has been shown to improve catalyst stability.¹⁶

The nature of the active sites has a direct bearing on the surface-specific activity, often referred to as the turnover frequency (TOF), and the catalyst selectivity. This nature is determined by the composition (i.e., type of metal and promoters or bimetallics), size, and shape of the nanoparticles. Reduction of the size of the nanoparticles increases the amount of surface sites per unit weight of metal and generally results in more active catalysts. For structure-sensitive reactions favored by specific surface sites, such as low-coordination sites found on defects, corners, steps, or edges, reduction of the particle size may enhance the TOF.¹⁷ However, maximum weight-based activities at a certain particle size have also been reported. In the dehydrocyclization of *n*-heptane over Pt catalysts, a large increase in TOF was observed with decreasing particle size from 4 to 1.5 nm, whereas further reduction in size resulted in a large decrease.¹⁸ The TOF of Fischer–Tropsch cobalt catalysts was found to be constant for particles larger than 6 nm, while below 6 nm it steeply decreased.^{19,20}

The nature of the metal(s) and the support can also influence the catalyst stability. For example, small Ag particles displayed a much higher adhesion energy when supported on reduced CeO₂ compared to MgO,²¹ and 4 nm bimetallic PtRh particles exhibited higher thermal stability compared to monometallic Pt particles.²² The initial particle size might play a role as well, since 2 nm Pt nanoparticles in polymer electrolyte membrane fuel cells were found to be very unstable, while 5 nm particles exhibited almost no deactivation.²³ Similarly, 3–4 nm Ni particles on silica gel used in the methanation reaction exhibited rapid particle growth resulting in particles up to 100 nm in size, whereas 8–9 nm initial particles remained of a size similar to the pore diameter (10 nm) of the silica gel support.²⁴

Accessibility of active sites calls upon control of the catalyst porosity. This is key for the rate of mass transfer of reactants to and products from the active sites, and affects activity by diffusion rates, selectivity by the extent of secondary reactions, and stability via processes such as coke formation and poisoning. In academia, fine powder grains are often used to ensure good accessibility of the active sites to prevent mass-transfer limitations. However, small grains cause a large pressure drop over a catalyst bed of significant height. Therefore, catalyst support bodies or pellets a few millimeters in size are often used in industry. For these relatively large bodies, the macroscopic distribution of the active sites becomes important, and a useful tool to estimate the degree of mass-transfer limitations in a catalytic system is the Thiele modulus φ :

$$\varphi = \frac{V_p}{A_p} \sqrt{\frac{k_t}{D_e}} \quad (1)$$

where V_p is the volume of the pellet, A_p is the external surface area of the pellet, k_t is the first-order rate constant, and D_e is the effective diffusion coefficient. A φ greater than 0.3 is an indication that diffusion of the reactant through the pores is rate limiting. Thus, for large catalyst bodies, a homogeneous distribution of the active phase is only preferential for relatively slow catalytic reactions, providing reactants time to diffuse to the active sites. If the reaction is fast or if secondary reactions are problematic, a different macroscopic distribution of the active phase might be preferred, such as an eggshell distribution

or an egg-white distribution if the catalyst is prone to attrition. If the reactants contain poisons, an egg-yolk distribution may be favorable so that the poison can be captured at the edge of the catalyst body, where few active sites are present (Figure 1).

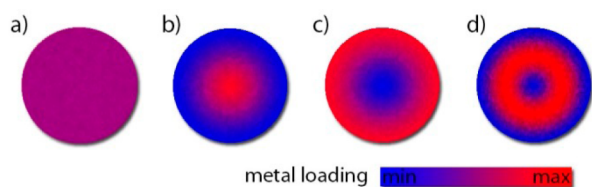


Figure 1. Different types of macroscopic metal distributions across a support body: (a) homogeneous distribution, (b) egg-yolk distribution, (c) eggshell distribution, (d) egg-white distribution (red, high concentration of metal; blue, low concentration of metal).

Common support materials consist of refractory oxides such as SiO_2 , Al_2O_3 , or TiO_2 . These materials exhibit high specific surface areas, high porosities, and high thermal and mechanical stability and come in a variety of pore sizes, while they are mostly chemically inert. Carbon is also widely used, while zeolites are often applied in many oil-refining and petrochemical applications. Recently, an increasing variety of ordered mesoporous materials have been used as model supports.²⁵ Finally, metal organic frameworks are showing an increased use as catalysts or as support for metal (oxide) nanoparticles.²⁶ To maintain activity as well as for practical reasons, the support requires a high mechanical strength and the macroscopic bodies should be resistant to attrition if the catalyst is vigorously agitated such as in fluid bed or slurry bed reactors.

Oxidic supports are commonly produced via sol–gel chemistry, in which a metal precursor (usually a silicate dissolved in water, sometimes a metal alkoxide in an organic solvent) is polymerized in solution, forming polysilicate species. Further condensation leads to the formation of small particles, links between particles, and eventually the formation of a gel. Parameters such as the pH, temperature, growth time, and presence of salts are important to determine the morphology of the oxides formed. Also the drying procedure and further thermal treatment are critical to determine the final porosity of the carrier.²⁷ The surface of oxidic supports generally contains a significant concentration of hydroxyl groups, which act as adsorption sites for metal complexes and are key to many interactions between the metal precursor and the support. Depending on the type of support and the pH of the aqueous solution, these groups can become protonated or deprotonated.²⁸ For each support, in water there exists a pH for which the net charge of these surface groups is zero, so that the net particle charge can be considered nil. Above this pH, more groups are deprotonated and the surface is negatively charged, whereas, below the point of zero charge (PZC), the surface is positively charged due to protonation. Table 1 shows the PZC for several important supports. An extensive list can be found elsewhere.²⁹

Oxidic supports can often (partly) dissolve in acidic or alkaline media. This can have a negative effect on the resulting catalyst, such as with the impregnation of aqueous cobalt nitrate on γ -alumina.³⁰ Partial dissolution of the alumina resulted in loosely bound cobalt particles after drying and thermal treatment, giving rise to attrition during Fischer–Tropsch synthesis and thus contamination of the product stream. However, partial dissolution can also be beneficial. During

Table 1. Point of Zero Charge for Several Important Supports in Aqueous Solution²⁹

support	PZC range	support	PZC range
SiO_2	2–4	$\gamma\text{-Al}_2\text{O}_3$	8–9
oxidized activated carbon	2–4	activated carbon	8–10
TiO_2	5–7		

deposition precipitation of nickel on silica, partial dissolution of the silica has been proposed to facilitate the deposition of a nickel silicate phase, forming small homogeneous particles during subsequent thermal decomposition.³¹ Thus, the solubility of the support may play a role in the synthesis of heterogeneous catalysts, although it is rarely considered explicitly.

3. PRECIPITATION

Precipitation can be induced by a change in conditions such as temperature, pH, or evaporation, and has long been used to produce supported catalysts. Controlled precipitation from a precursor solution follows the principles of nucleation and growth. An initial nucleation boom of tiny crystallites followed by growth without the formation of new nuclei can result in small and quite monodisperse particles. This concept is known as “burst nucleation” and is not only important for precipitation but also key in the synthesis of colloids and can play a role in the synthesis of catalysts via impregnation.

3.1. Coprecipitation

In coprecipitation, salts of the active metal and support are dissolved and mixed such that nucleation and growth of a combined solid precursor of the active metal and support is obtained in a single step. Very high metal loadings of 70 wt % and higher can be achieved while maintaining small particle sizes, and as such, it is the most convenient way to produce catalysts with a high metal weight to volume ratio. Small particles are formed even at these high loadings by creating a very high degree of supersaturation, so that all components nucleate at a high rate and at the same time. This is often realized by mixing two concentrated solutions, the components of which result in an insoluble material when combined. Highly soluble metal nitrates, chlorides, or sulfides can be mixed with basic reagents such as alkali carbonates or hydroxides so that metal carbonates or hydroxides are formed. The low solubility of these compounds causes most of the precursor to precipitate. During coprecipitation, great care has to be taken to prevent local fluctuations in the conditions caused by, for example, temperature gradients, insufficient mixing, or concentration gradients, which can cause additional nucleation events, different or inhomogeneous growth patterns, or the precipitation of different phases. New techniques such as spray-drying and continuous consecutive precipitation can help overcome these practical problems.^{32,33}

Coprecipitation can be utilized to produce catalysts such as nickel alumina for steam reforming³⁴ or iron copper potassium for Fischer–Tropsch synthesis,³⁵ while most recent systematic studies that have led to increased fundamental insight focused on $\text{Cu}/\text{ZnO}/\text{Al}_2\text{O}_3$ catalysts for methanol synthesis. The active sites for this catalyst are metallic copper step sites which are in close contact with Zn.¹ Molar Cu/Zn ratios of 70:30 are most common, while the molar Al_2O_3 content is generally below that of Zn, and preparation is done by combining copper, zinc, and aluminum nitrates and precipitated using alkali (bi)-

carbonates.³⁶ After precipitation and aging, washing steps are necessary to remove residual nitrates and sodium or potassium, which can cause particle sintering and agglomeration during further thermal treatment, leading to a loss of surface area. Titration experiments have shown that precipitation is preferably performed at constant pH. When the pH is slowly increased, sequential precipitation results, whereby Cu is first precipitated followed by Zn.³⁷ Baltes et al. systematically studied the precipitation at different pH values (4.5–10) and temperatures (30–70 °C), while keeping the subsequent treatments the same (1 h of aging, calcination at 300 °C).³⁸ The precipitation conditions had little effect on the Cu/Zn/Al ratio, which was similar in all precipitated samples, and close to that of the initial solution (60:30:10). However, large differences were observed in the Brunauer–Emmett–Teller (BET) and Cu(0) surface areas after reduction at 300 °C in H₂ (Figure 2). The lowest Cu(0) surface areas were found at a very

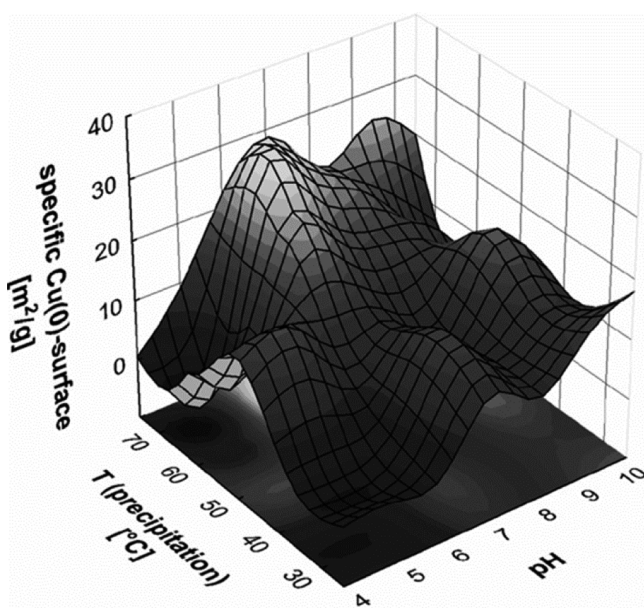


Figure 2. Influence of the pH and temperature during the precipitation of Cu/Zn/Al catalysts on the final specific Cu(0) surface area. After precipitation, all catalysts were aged for 1 h, calcined at 300 °C, and reduced at 300 °C. The final properties of the catalyst were highly dependent on the conditions during precipitation. In general, a higher temperature and a pH between 6 and 7 during precipitation resulted in catalysts with the highest metallic copper surface areas. Adapted with permission from ref 38. Copyright 2008 Elsevier.

low pH, where X-ray diffraction (XRD) revealed large CuO crystallites and ZnO diffraction lines after calcination. High Cu(0) surface areas were generally found at higher precipitation temperatures, with a maximum at a pH of 6–7 at a temperature of >60 °C, in agreement with the results of previous studies. Under these conditions, small CuO particles and some residual zincian malachite, $(\text{Cu,Zn})_2(\text{CO}_3)(\text{OH})_2$, were reported after calcination.³⁸

Zincian malachite has previously been reported to be the desired precursor for the formation of active methanol catalysts.³⁹ The crystalline phase is formed during the aging process after initial precipitation, which generally forms an amorphous product due to the fast kinetics of the precipitation process (Figure 3). The resulting zincian malachite consists of thin needles 5–15 nm in width, and forms the general

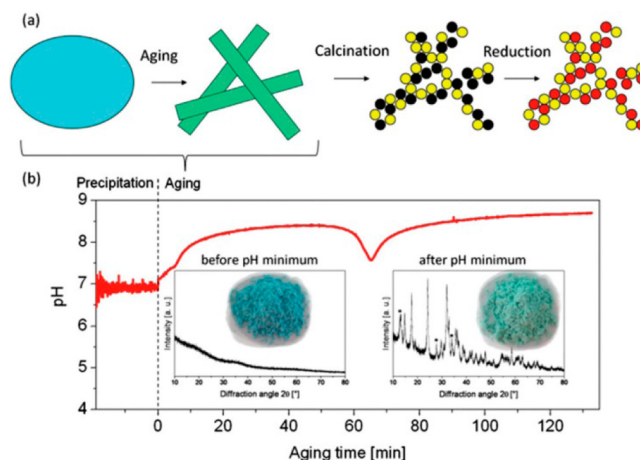


Figure 3. (a) Cartoon of the steps during coprecipitation of Cu/ZnO catalysts. During precipitation, an amorphous material is obtained, which is turned into a crystallite phase during aging. A subsequent calcination step forms small CuO and ZnO particles, the former of which can be reduced. (b) Evolution of the pH during precipitation and aging of a typical Cu/ZnO sample, along with the associated change in color and crystallinity during aging (inset). Adapted with permission from ref 39. Copyright 2012 Royal Society of Chemistry.

mesostructure of the catalyst. By incorporation of Zn, close Cu–Zn interactions enable the formation of small Cu particles during subsequent calcination and reduction.⁴⁰ Zander et al. analyzed the aging process of Cu/Zn (molar ratio 70:30) in detail with in situ energy-dispersive XRD (EDXRD) and UV–vis measurements.³⁹ The precipitate was formed at pH 7 at 65 °C, close to the previously found optimum, and immediately spray-dried to allow separation of the precipitation and aging steps. Subsequently, the aging step was studied in a pH range between 5 and 8, and at temperatures between 50 and 70 °C. Two mechanisms were found for the formation of high Zn incorporation into zincian malachite. At pH > 7, a sodium zinc salt precipitated along with a low Zn content zincian malachite, followed by slow dissolution of the sodium zinc salt and incorporation of the Zn into the zincian malachite during aging. At pH between 5 and 6.5, direct co-condensation of copper and zinc caused direct formation of the zincian malachite, resulting in the highest amount of Zn incorporation (29.2%), close to the total amount added.⁴⁰ A study on different precipitation agents for Cu/Zn/Al precipitated at pH 6 and aged for 2 h showed little difference in the obtained crystalline phases and final BET surface area among sodium, potassium, and ammonium carbonate precipitating agents, although use of sodium hydroxide provided a notably lower surface area.⁴¹

After aging, the zincian malachite precursor is converted into CuO and ZnO particles by a calcination step. Stepwise calcination at 100 °C intervals from 200 to 700 °C showed the best result was usually obtained at 300 °C.³⁸ At this point, most of the copper was present in the form of small CuO particles, while some degree of zincian malachite was still present. Although decomposition of these last traces was possible at higher temperatures, this also resulted in a sharpening of the CuO XRD diffraction line, corresponding to larger CuO particles due to sintering at the increased temperature. Other studies on Cu/Zn/Al coprecipitates also reported an increase in CuO particle size upon increasing the severity of the calcination procedure. Increasing the calcination time at 350 °C from 1 to 3 h increased the CuO particle size

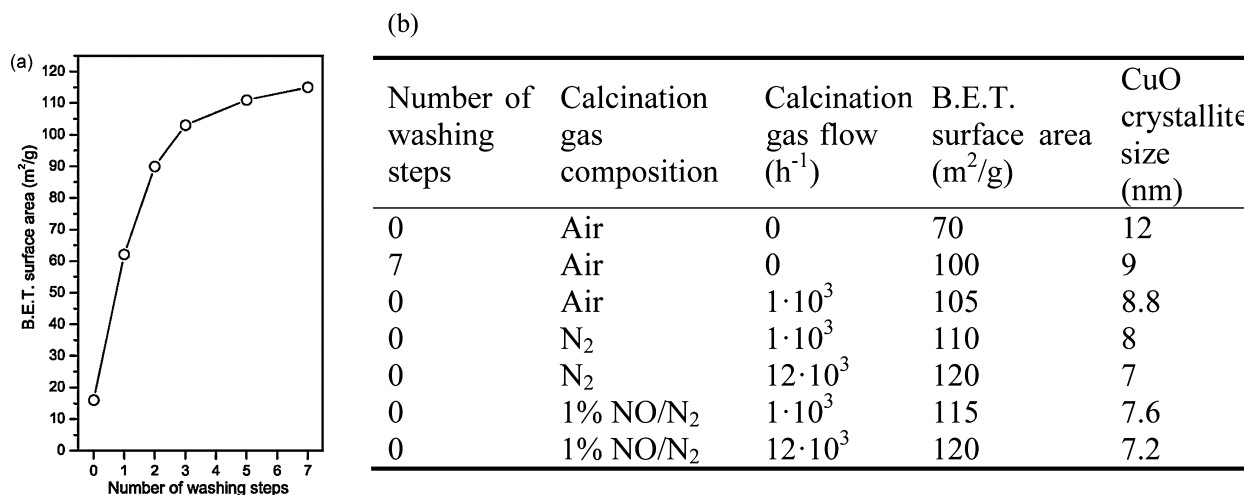


Figure 4. Evolution of the BET surface area of Cu/ZnO/Al₂O₃ catalysts obtained by different washing and calcination treatments after coprecipitation: (a) Na₂CO₃ used as the precipitating agent, followed by calcination in stagnant air, (b) (NH₄)HCO₃ used as the precipitating agent, followed by different numbers of washing steps and calcination treatments. Adapted with permission from ref 47. Copyright 2013 Elsevier.

from 3.0 to 3.7 nm, which increased further to 5.0 nm at 400 °C.⁴² Similarly, increasing the calcination temperature from 400 to 700 °C brought about a gradual increase from 5.3 to 15.8 nm, highlighting the importance of a relatively mild activation treatment.⁴³

Although water is normally used as the solvent for precipitation techniques, high Cu surface areas have been obtained in a solvent mixture of ethylene glycol and water at a ratio of 4:1.⁴⁴ Cu/Zn/Al at a ratio of 3:3:1 was precipitated at pH 5 and 70 °C, aged for 2 h, and calcined at 350 °C. It was postulated that the ethylene glycol works as a surfactant that adsorbs on the surface of growing crystallites, thereby inhibiting further growth so that small particles and high surface areas are obtained. However, mixing other polar solvents with water, such as ethanol, tetrahydrofuran, and 1,4-dioxane, had a negative effect on the Cu surface area.

Microwave irradiation has been investigated as an alternative heat source during the precipitation and aging process of Cu/Zn/Al at a molar ratio of 64:32:4 at pH 7.5–8.⁴⁵ Although microwave irradiation had little effect on the precipitation process, aging at 70–90 °C using microwave irradiation showed an increased incorporation of Zn compared to regular aging at the same temperature, eventually leading to smaller CuO particles after activation.

3.1.1. “Greener” Coprecipitation Methods. Coprecipitation methods generally require numerous washing steps after precipitation to wash out residual nitrates, sodium, potassium, and other compounds to prevent sintering and agglomeration of particles during thermal treatment. This produces large amounts of wastewater contaminated with nitrates, and although this is undesired, precursor salts based on sulfate or chloride instead of nitrate introduce poisons for the methanol catalyst. To circumvent this, metal formates have been investigated as a precursor replacement.⁴⁶ Titration experiments revealed that copper and zinc formates have a higher tendency to simultaneously precipitate, increasing the homogeneity of the metal distribution in the precipitate. In the absence of nitrates, formation of zincian malachite is not possible, and instead, a phase with the general formula (Cu_{1-x}Zn_x)₂(OH)₃HCO₂ was formed. Investigation of the crystal structure revealed a maximum Zn incorporation into the precursor phase of around 20% ($x = 0.2$), somewhat lower

compared to the 20–30% generally found in zincian malachite when using nitrate precursors. Upon coprecipitation of Cu/Zn from formate precursors, 12 nm CuO particles were found, somewhat larger than present in conventional systems. However, this was attributed to the lack of Al₂O₃ in the sample and relatively lower amount of Zn. Even so, the catalyst showed a relatively good activity, possible due to the good interaction of the Cu and Zn phases, showing formates are promising nitrate substitutes.

Alternatively, altering the calcination treatment has been shown to circumvent the need for a multitude of washing steps to remove residual nitrates altogether.⁴⁷ Cu/Zn/Al catalysts with a molar ratio of 55:30:15 were precipitated using Na₂CO₃ or (NH₄)HCO₃ at a pH of 7 and a temperature of 70 °C and aged for 2 h. If no washing was performed, a very low BET surface area of 15 m²/g was found after calcination in stagnant air for the sample precipitated with Na₂CO₃ (Figure 4). This increased significantly with each washing step, to a maximum of 115 m²/g after seven steps, illustrating the importance of removing nitrates and sodium to prevent agglomeration of the resulting copper particles. When (NH₄)HCO₃ was used as the precipitating agent, the values varied from 70 to 100 m²/g after calcination in stagnant air depending on the number of washing steps. However, if the calcination was performed in a high flow of N₂, 120 m²/g was obtained without performance of a single washing step. Moreover, although washing is normally needed to remove sodium from the sample, by using (NH₄)HCO₃, the need for a washing step was circumvented altogether, albeit at less than quantitative precipitation of copper. Alteration of the thermal treatment step has been rarely studied for precipitated catalysts, in contrast to catalysts prepared by impregnation and drying, which is discussed in detail in section 4.4.

3.2. Deposition Precipitation

Similar to coprecipitation, deposition precipitation concerns deposition from a precursor solution through a change of pH, temperature, or evaporation, so that metal compounds are formed with a low solubility, often metal hydroxides. In the case of deposition precipitation, this is done in the presence of an existing support, and the concentration of the new compound is increased gradually to prevent formation of bulk phases in solution. Preferential precipitation on the support can be

achieved because introduction of the support in the solution causes either a reduction of the surface free energy of tiny nuclei or stabilization of the precipitate, decreasing the energy barrier for nucleation. Hence, conditions exist where nucleation can only occur on the support and not in the bulk solution, so that the support surface functions as a seed for nucleation.³¹

Nucleation of the metal species is generally induced by changing the pH so compounds with a low solubility are formed. When this is done by injection of the precipitant (e.g., alkaline solution), great care has to be taken to prevent local concentrations exceeding the critical supersaturation, which would cause bulk precipitation. Because of this, homogeneous deposition precipitation methods are often preferred, whereby precipitation is induced homogeneously throughout the reaction vessel. This can be achieved by adding urea (at room temperature), which when heated to 90 °C will slowly decompose, resulting in the formation of OH⁻, thereby slowly enhancing the pH upon decomposition. Other popular precipitation techniques include the direct reduction of solvated metal ions to the metal⁴⁸ or a gradual reduction of the pH by slow removal of ligands such as ammonia via evaporation.⁴⁹

Classically, deposition precipitation was developed to produce catalysts with metal loadings that exceed those obtained by impregnation which is limited by solubility;⁵⁰ however, few recent studies in this respect are noted. In one, hexachloroplatinic acid was used as a precursor to deposit up to 60 wt % Pt on a high surface area carbon black via deposition of PtCl₆(OH)_y(H₂O)_z species formed by the decomposition of urea.⁵¹ Increasing the urea/Pt molar ratio from 0 to 80 showed a decrease in size of the Pt particles from 5 to 2 nm (Figure 5)

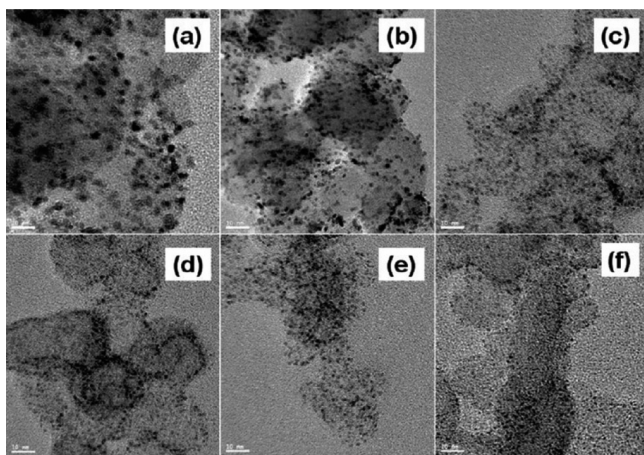


Figure 5. TEM images of 60 wt % Pt/C before reduction, showing the size of the Pt nanoparticle complexes dependent on the amount of urea used during deposition: (a) no urea, (b–f) urea/Pt molar ratio of (b) 5, (c) 10, (d) 20, (e) 40, and (f) 80. Scale bar 10 nm. Adapted from ref 51. Copyright 2009 American Chemical Society.

before reduction. Note that deposition was also possible without addition of urea, suggesting not only precipitation but also adsorption of Pt complexes played a role (see section 4.2). It was postulated that the observed reduction in size was mainly due to electrostatic charge effects: at a higher pH, obtained by more urea addition, Pt complexes with a more negative charge were formed, so that their growth was limited by repulsion. The reduction step was also important for the final metal particle size. When reduction was performed by addition of NaBH₄ at room temperature, the high reduction potential of NaBH₄

resulted in large particles and agglomerates. When ethylene glycol was added at room temperature instead, small monodispersed Pt particles were obtained by in situ formation of acetaldehyde at 120 °C, which functioned as a reducing agent. A separate study focused on the initial pH of the solution for the production of 40 wt % PtRu (equal molar ratio) on carbon black.⁵² Through addition of NaOH, the initial solution was varied between pH 3 and pH 10 before the temperature was raised to 90 °C to start decomposition of urea (urea/PtRu molar ratio of 20). The metal particle size varied from 3.6 nm at pH 3–4 to 2.6 nm at pH 9–10 after reduction in a flow of H₂.

Cobalt has been deposited on silica gel and carbon nanofiber (CNF) supports using deposition precipitation starting from an aqueous solution of cobalt nitrate and urea.⁵³ At a 15 wt % loading of cobalt, the resulting material consisted of mainly cobalt hydrosilicates on silica, whereas on CNF a weak interaction with the precursor resulted in limited nucleation on the support, with both materials exhibiting large cobalt particles after reduction (40 and 25 nm, respectively). Uniform deposition was more successful when cobalt carbonate and a high initial pH were used instead, and precipitation was induced by evaporation of ammonia at 90 °C, slowly lowering the pH. Using this method, much smaller particles of 8 and 13 nm size were obtained for CNF and silica, respectively. Similar results were obtained in a separate study on Co/TiO₂ at loadings varying between 4 and 24 wt %. Although some small 2 nm particles were found using urea and cobalt nitrate, large unsupported particles were observed, resulting in an average of 20 nm particles at 4 wt % Co and 50 nm at 24 wt % on titania. Deposition precipitation onto titania of cobalt carbonate by evaporation of ammonia resulted in a homogeneous distribution of 9 nm particles at 4 wt % Co, growing only to 15 nm for the sample prepared at 24 wt %.⁵⁴ These results show the interaction of the precursor and the support is important to the method of deposition precipitation; when the interaction is too strong, such as with cobalt nitrate and silica, mixed metal–support phases are formed, whereas a too weak interaction, such as with cobalt nitrate and CNF or TiO₂, results in large, unsupported particles. In all reported cases, deposition precipitation of cobalt carbonate by evaporation of ammonia resulted in a more optimal interaction.

3.2.1. Gold Catalysts. Recently, deposition precipitation has frequently been used for the preparation of finely dispersed gold particles at relatively low loadings. A facile and common proceeding starts with an aqueous solution of HAuCl₄ to arrive at 0.5–2 wt % loading.⁵⁵ The pH of the solution is raised using NaOH, followed by addition of the support under vigorous stirring, and heating to 70 °C. In general, not all gold is deposited from solution, and an investigation on the effects of pH during deposition for Au/TiO₂ revealed the uptake of gold was maximum at a pH around 6, close to the PZC of the TiO₂ support.^{56,57} However, this resulted in the formation of large Au particles, while a good compromise between particle size and uptake was obtained at pH 9. This technique has been applied to deposit Au on a variety of supports such as a hydrotalcite,⁵⁸ diamond,⁵⁹ SiO₂/TiO₂,⁶⁰ and Al₂O₃.⁶¹ However, several studies on the mechanism argue that it is technically not a deposition precipitation.^{56,62–65} Moreau et al. proposed that electrostatic adsorption takes place at a pH below the PZC for gold deposited on titania, while above the PZC a neutral Au(OH)₃·H₂O species adsorbs on two TiO⁻ surface sites.⁶⁵ Cellier et al. compared anion adsorption at pH 3 to deposition precipitation at pH 7 on two titania supports.⁶⁴ In both cases,

evidence of gold chloride complexes on the surface of the support was obtained, suggesting $\text{AuCl}_{4-x}(\text{OH})_x^-$ complexes had reacted with surface OH groups to form surface species, rather than forming a precipitate of the type $\text{Au}(\text{OH})_x\text{Cl}_{3-x}$. Moreover, when titania with a higher surface area was used, a higher Au loading was achieved, corroborating the mechanism of surface adsorption rather than precipitation. It has been argued that an adsorption equilibrium explains why not all Au precipitates from solution, although finite solubility of a precipitate offers an alternative explanation.

Zanella et al. already postulated a similar mechanism of gold surface complexation for the NaOH “deposition precipitation” method in 2002, and compared it with the more conventional deposition precipitation method using urea to slowly raise the pH for the preparation of a Au/TiO₂ catalyst with a nominal loading of 8 wt % Au.⁶³ Precipitation of all gold in solution was achieved using the urea deposition precipitation method, whereas a maximum Au loading of only 3 wt % was obtained using the NaOH method, suggesting the two involve different deposition pathways. Further study suggested that $\text{AuCl}(\text{OH})_3^-$, the dominant species at pH 8, reacts with the surface hydroxyl species in the NaOH method.⁶⁶ For the urea deposition method, a gold–urea or gold–urea derivative complex formed with a high N content, although the exact nature of the complex was not reported. It was postulated that initially some $\text{AuCl}_{4-x}(\text{OH})_x^-$ anions adsorbed on the positively charged support surface hydroxyl groups at low pH, which serve as nucleation sites for the precipitation of the gold–urea complex species in the first hour. These form relatively large particles, which fragment into smaller particles upon aging as the pH rises further (Figure 6).

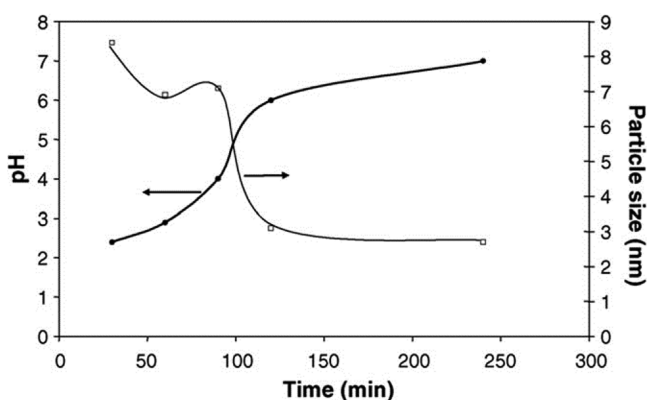


Figure 6. Time evolution of the pH and the Au particle size estimated by TEM during the preparation of 8 wt % Au/TiO₂ prepared by deposition precipitation using urea. Adapted with permission from ref 66. Copyright 2005 Elsevier.

The urea deposition precipitation method was further used to deposit Au on Al₂O₃, TiO₂, ZrO₂, and CeO₂ at loadings between 1 and 7 wt %.⁶⁷ In each case, small particles of around 2 nm size were found by transmission electron microscopy (TEM) analysis, and the synthesis was readily scaled up to 50 g without compromise. Moreover, it was concluded that, at a loading of 1 wt %, which was found to be below the absorption capacity of the supports investigated, all the gold was initially adsorbed by the support as $\text{AuCl}_{4-x}(\text{OH})_x^-$ species. This first adsorption step was then rapidly followed by a change of speciation by adsorbed gold–urea complex formation, so that again this technically is not a deposition precipitation. Using

this method, 1 wt % AuPd bimetallic particles were deposited on TiO₂ and Al₂O₃ with different Au/Pd ratios and very good incorporation of Pd into the Au particles.^{68–70}

A thermodynamic model has been proposed to rationalize the cluster size of Au particles during deposition precipitation using urea.⁷¹ A key part of the model is the dependency of the interfacial energy on the electrostatic interaction between the nanoparticles and support, which was related to the PZC of the support and the pH of the solution. The experimental data of 2 wt % Au deposited at a pH of 8 on different supports (Al₂O₃, PZC = 8; TiO₂, PZC = 6; SiO₂, PZC = 4) showed a decrease in particle size from 2.3 to 1.6 nm with decreasing support PZC. Even though further thermal treatments such as drying and calcination were not taken into account, and the authors acknowledged that the model provides only some qualitative trends, while the interactions involved are likely more complicated, the experimental results were in fair agreement with model predictions.

4. IMPREGNATION AND DRYING

4.1. Impregnation

Impregnation and drying is a frequently used preparation method among others due to its simple execution and low waste streams. The first step is contacting a metal precursor solution with a porous support. Common precursors include inorganic metal salts, such as metal sulfates, carbonates, chlorides, nitrates, or acetates, and organic metal complexes, such as metal acetylacetonates. The most commonly used solvent for inorganic salts is water because of the high solubility of many precursors, whereas organic solvents are mainly used for organometallic precursors. To prevent premature deposition of the metal precursor in bulk solution, concentrations below (super)saturation are required.

Two main impregnation methods are distinguished, namely, wet impregnation (WI), whereby an excess amount of solution is used, and pore volume impregnation (PVI), in which an amount to just fill the pore volume of the support is used. The latter method is also known as incipient wetness impregnation (IWI) or dry impregnation (DI), because the impregnated material keeps a dry character at a macroscopic scale. Uptake of the liquid into the pores of the support occurs due to the capillary pressure difference Δp across a hemispherical meniscus in a pore with radius r_p according to the Young–Laplace equation⁷²

$$\Delta p = (2\gamma_{lv}/r_p) \cos \theta \quad (2)$$

where γ_{lv} is the surface tension between the liquid and vapor interface and θ is the wetting angle between the solid and the liquid. If $\theta < 90^\circ$, the liquid is considered as wetting and will penetrate the support spontaneously, which is the case with water in combination with most oxidic supports. If the liquid is nonwetting ($\theta > 90^\circ$), the capillary pressure becomes negative and an external pressure is needed to force the liquid into the pores. This can occur for hydrophobic supports such as carbon materials, for which a less polar solvent such as ethanol or 2-propanol may be more appropriate, although this usually comes at the expense of a lower precursor solubility. From eq 2 it is clear the pressure difference depends inversely on the pore size, so that liquid is preferentially sucked up by the smallest pores. The rate at which the liquid fills the pores is generally fast and is often not considered critical for catalyst synthesis. According to the Washburn equation,⁷³ infiltration of a wetting liquid into

a porous body of a few millimeters can occur in seconds to minutes, as has been experimentally verified.⁷⁴ However, when the support is pretreated with the same solvent before loading of the precursor via wet impregnation, capillary forces do not play a role and the only driving force for the precursor to enter the support is diffusion, which can take significantly longer.⁷⁵

4.1.1. Pore Filling. Although pore filling occurs rapidly, whether all pores are filled after impregnation to incipient wetness has been questioned. Inhomogeneous MnO₂ and Fe distributions have been observed after calcination on SBA-15 and MCM-41, respectively, and attributed to inhomogeneous filling during impregnation.^{76,77} Direct imaging of the impregnated precursor solution is difficult, due to evaporation and decomposition induced by a high-intensity beam of an electron microscope. A first visualization of SBA-15 impregnated with a nickel nitrate hexahydrate solution was done by Sietsma et al. using cryo-TEM.⁷⁸ Frozen to $-197\text{ }^{\circ}\text{C}$, many pores were found empty after impregnation (Figure 7), which

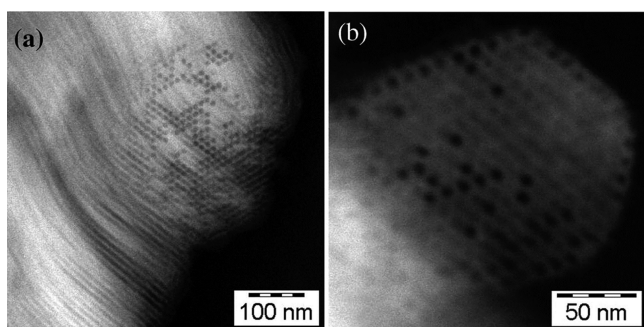


Figure 7. Cryo-HAADF-STEM (cryogenic high-angle annular dark field scanning transmission electron microscopy) images of the SBA-15 pore volume impregnated with an aqueous nickel nitrate solution and frozen to $-196\text{ }^{\circ}\text{C}$, showing several pores remained empty after impregnation. Adapted from ref 78. Copyright 2008 American Chemical Society.

was attributed to the relatively low hydroxyl density of SBA-15 compared to that of regular silica, resulting in incomplete wetting. However, it is also possible N₂ physisorption underestimated the total pore volume of the SBA-15, so that there was not enough liquid to fill all the pores. A more detailed cryo-TEM tomography study was performed by Eggenhuisen et al. on SBA-15 impregnated with cobalt nitrate or nickel nitrate solutions.⁷⁹ Although a few empty pores were found mainly on the external edge of the support particles, the majority were filled, and it was concluded that impregnation does lead to an almost homogeneous and complete pore filling. More quantitative measurements on larger samples by differential scanning calorimetry (DSC) have also provided evidence on the complete filling of porous supports (Figure 8).⁸⁰ Due to the downward shift in the melting point of liquid confined in nanopores, a distinction was possible between extraporous and intraporous liquid in the material. Incipient wetness impregnation of several ordered mesoporous silicas and silica gels with several solutions, including a eutectic nickel nitrate solution, resulted in fillings between 90% and 100%.

The two-solvent impregnation method, also known as the double-solvent technique, offers an alternative to ensure no material ends up at the outer surface of the support particle.⁷⁶ In this method, the support is first dispersed in an apolar solvent such as pentane or cyclohexane. Subsequently, an

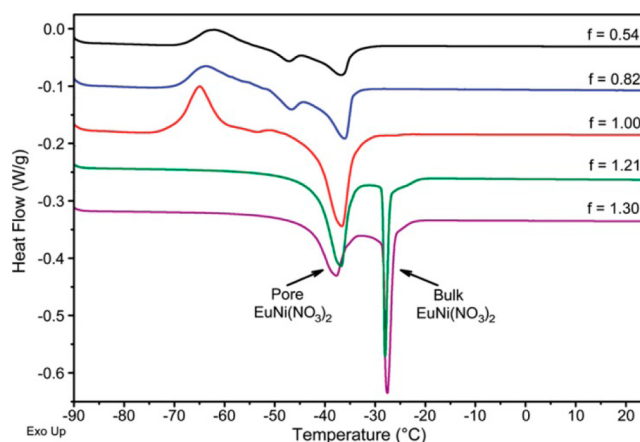


Figure 8. DSC measurements during the heating of a silica gel with 16 nm pores filled with a eutectic nickel nitrate solution (EuNi(NO₃)₂). The maximum filled fraction f is defined by $f = V_{\text{EuNi(NO}_3)_2} / V_{\text{SiO}_2 \text{ pores}}$. Due to confinement, the solution in the pores melts (endothermic peak) at a lower temperature compared to the extraporous or bulk solution. Even at a filling of 1.00, no bulk melting was detected, indicating all of the impregnation solution was located inside the pores. Adapted from ref 80. Copyright 2009 American Chemical Society.

aqueous solution containing the metal precursor is added. Due to the favorable wetting properties of the aqueous solvent, i.e., the aqueous phase has a lower contact angle θ , it replaces the apolar solvent in the mesopores of the support. However, inhomogeneous distributions inside the catalyst grains are often reported after drying and calcination when using this method,^{81–84} which is at least partly influenced by the choice of the apolar solvent. Van der Meer et al. studied pentane, hexane, heptane, and cyclohexane as apolar solvents for the production of Co₃O₄/SBA-15 from an aqueous solution of cobalt nitrate, followed by drying and calcination.⁸⁴ Use of cyclohexane resulted in large aggregates of cobalt particles a few hundred nanometers in size, whereas pentane resulted in relatively small aggregates several tens of nanometers in size. It was proposed that the aggregate size is influenced by the size of the aqueous droplets that form in the alkane phase, which is influenced by the interfacial tension between the polar and apolar solvents. This was lowest for pentane, resulting in the smallest droplets and subsequent aggregates.⁸⁵ Comparison of nickel acetate and nickel nitrate on MCM-41 (Ni loading of 1 and 5 wt %) showed more homogeneous distributions were obtained using nickel acetate, suggesting the thermal treatment after impregnation plays a significant role in the distribution of the precursor.⁸² In this case, it was postulated that nickel acetate exhibited stronger adsorption on the support surface, thereby limiting redistribution, whereas nickel nitrate redistributed during further treatment due to a weak interaction with the support, as will be discussed in the following sections. Also note that organic material present during subsequent thermal treatments can greatly affect the final dispersion of the catalyst, as discussed in section 4.4.1.

4.2. Adsorption

In general, adsorption of metal ions from aqueous solution onto a support plays an important role when low metal loadings are applied. Electrostatic adsorption requires the pH of the solution to be different from the PZC of the support to create adsorption sites in the form of charged surface hydroxyl

groups. This ability of support surface hydroxyl groups in water to become protonated or deprotonated also allows them to function as a pH buffer. When a γ -alumina with a surface area of 200 m²/g, pore volume of 0.5 mL/g, and surface hydroxyl density of 8 groups/nm² is impregnated to incipient wetness with an acidic solution of pH 3, only 1 of 5000 surface groups become protonated so that the surface will be negligibly charged. However, the pH of the solution will rise from 3 to that close to the PZC charge of the γ -alumina, about 8–9.⁸⁶ Therefore, adsorption is often low upon incipient wetness impregnation, especially with high precursor concentrations, and when adsorption is desired, wet impregnation is generally applied. It should be noted that the change in pH of the impregnating solution upon impregnation to incipient wetness is often not considered, even though many transition metals are hydrolyzed at high pH, which may result in premature precipitation of metal hydroxides.

Varying names are used for adsorption techniques, such as strong electrostatic adsorption (SEA), ion adsorption (IA), and equilibrium deposition filtration (EDF). All these methods are based on the same general principle. To achieve adsorption, wet impregnation is performed with a large excess of solution, a low concentration of the precursor, and a predetermined pH. The modes of deposition can be globally divided into two main modes of adsorption. Outer sphere complex formation concerns nonspecific, Coulombic or electrostatic interactions of the precursor with the support, whereby the support surface charge is compensated by a layer of charged metal ion complexes in solution. Inner sphere complex formation occurs when support surface groups become directly involved in binding the complex, e.g., when a surface oxygen or hydroxyl group enters the first coordination sphere of the metal complex. A detailed review on the fundamentals of adsorption can be found elsewhere.⁸⁷

4.2.1. Outer and Inner Sphere Complex Formation.

Adsorption via outer sphere complex formation concerns mainly electrostatic interactions, and has been formulated into a relatively simple model.⁸⁸ In general, multivalent ions preferentially adsorb over monovalent ions.⁸⁹ This type of adsorption is highly pH dependent; at a pH at the PZC, the net charge of the surface is zero and very limited or no adsorption takes place. Anions are adsorbed at a pH below the PZC, while cations are adsorbed when the pH is higher. Care should be taken not to use extreme pH values, whereby the high ionic strength of the solution diminishes the adsorption equilibrium constant, so that adsorption is actually reduced instead of improved. Moreover, support dissolution can be significant especially at a pH very different from the PZC of the support.

Recently, Regalbuto et al. used palladium, copper, cobalt, ruthenium, and nickel ammine complexes to obtain silica-supported catalysts at loadings between 1 and 3 wt %.⁹⁰ After deposition at a pH of 12, the catalysts were dried and directly reduced. Small particles between 1 and 3 nm in size were found, and calculations showed that these metal loadings were close to the maximum obtainable by electrostatic adsorption for the used silica with a surface area of 180 m²/g and a PZC of 4.0. It was postulated that the maximum loading mainly depends on the surface area of the support. A follow-up study focused on SBA-15 supports with different surface areas.⁹¹ Ammine complexes were used to deposit Pd nanoparticles of 1.3 nm size at a relatively high loading of 8.7 wt % on 1000 m²/g SBA-15, and 1.9 nm Pt particles were synthesized on SBA-15 with a 600 m²/g surface area with a loading of 9.2 wt %, showing high

surface areas were indeed beneficial for adsorption. Co particles were also synthesized using this method, but larger particles of 7 nm size at a loading of 5.1 wt % resulted. This was attributed to particle growth that occurred during the high reduction temperature of 800 °C needed to reduce the strongly adsorbing cobalt complexes, whereas the Pt and Pd catalysts were reduced at 350 °C or lower. Moreover, dissolution of the silica support was already observed at pH 9, and 25% of the SBA-15 silica was dissolved after 1 h at pH 10, the optimum pH for the uptake of metal cations. This led to a large increase in pore diameter and pore volume; however, this was not considered a problem due to the relatively thick walls of SBA-15. It was suggested to minimize the contact time to reduce this effect.

Recent studies have focused on adsorption on high surface area carbon supports to obtain high metal loadings. Hexachloroplatinate was deposited on several carbon xerogels with a BET surface area of 650 m²/g (at pH 11, PZC = 9.4), while platinum tetrammine was deposited on oxidized carbon (at pH 2.5, PZC = 2.4).⁹² The maximum loading of hexachloroplatinate was found to be 9.2 wt %, while that of platinum tetrammine was only 4 wt %, and scaled linearly with the mesoporous surface area of the support. It was hypothesized that the platinum ammine complexes, which retain two hydration sheaths, were too large to enter the micropores of the carbon, which was not a problem for the smaller hexachloroplatinate. In each case, small Pt particles between 1.1 and 1.3 nm in size were obtained. In another study, 2 nm Pt particles at a very high loading of 28 wt % were obtained on a carbon black material with a 1500 m²/g surface area using hexachloroplatinate at high pH.⁹³ Regalbuto et al. have shown for support material with a lower surface area that high loadings can be achieved by successive impregnation and reduction steps. On carbon xerogel with a surface area of about 600 m²/g, hexachloroplatinate was deposited at loadings of 7.5, 15.0, and 22.3 wt % for the first, second, and third steps, respectively.⁹⁴ Thus, it appeared the adsorbed metal ions formed small particles during reduction, thereby fully regenerating the adsorption sites, as has also been observed during atomic layer deposition (see section 5.3). Moreover, the particle size did not increase significantly upon additional treatments, but stayed constant at 2.0 nm, resulting in an increased particle density upon multiple deposition cycles.

Although short contact times (1 h) resulted in outer sphere complex formation, a longer contact time between platinum tetrammine and oxidized carbon at low pH gave rise to reduction of Pt concurrent with oxidation of the carbon surface.⁹³ Similarly, when trying to deposit cobalt on a carbon support at high pH, it was found that the cobalt ammine complex was completely converted to Co₃O₄ after 1 h, which did not occur on silica.⁹⁵ Reductive amination of the precursor took place, forming different precipitates depending on the pH (CoO at pH 9.2, Co₃O₄ at pH 9.8, and Co(OH)₄²⁻ at pH > 11 when NH₄OH was used as the base), so that the process is better described as a deposition precipitation. Moreover, at higher pH the cobalt ammine reacted to [Co(NH₃)₅Cl]Cl₂, which did not adsorb at all.⁹⁶ Nonetheless, particles of 5 nm size were obtained at a Co loading of 6.7 wt % at a pH of 10.

While in each of the previously discussed studies diluted slurries of a powdered support in a large excess of solvent were used, it was recently shown that significant adsorption is also possible during incipient wetness impregnation, in a modified method called charge-enhanced dry impregnation (CEDI).⁹⁷

To overcome the buffering effect and charge of the support, very high or low pH values were required (Figure 9). While

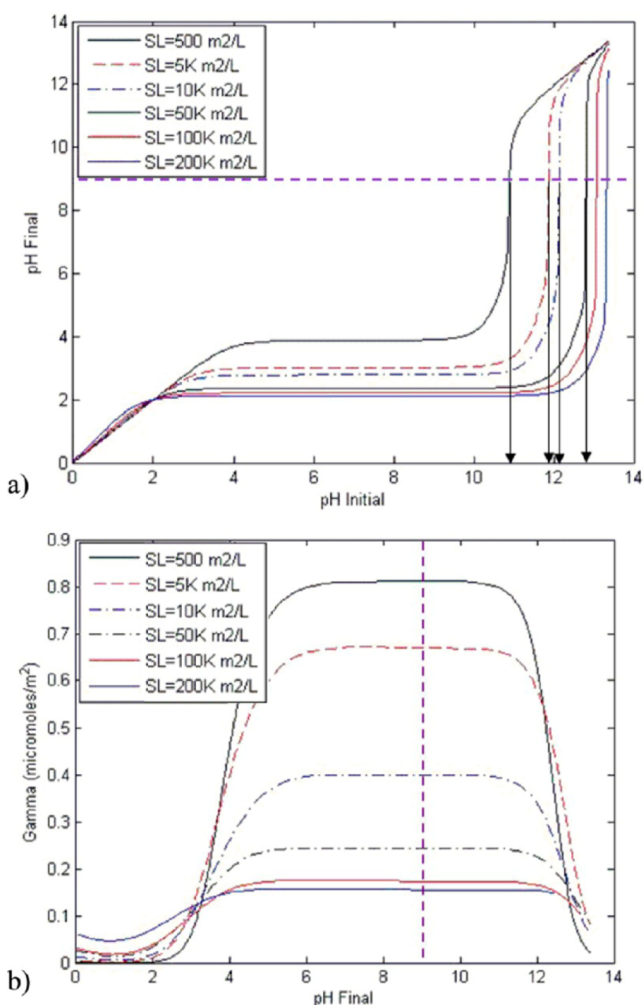


Figure 9. Estimation of the pH needed to obtain maximum cation adsorption for a material with PZC = 2: (a) difference in the initial pH of the solution and the final pH caused by buffering of the support, dependent on the surface loading (SL, defined as the amount of support surface area present in the slurry per liter), (b) cation uptake, dependent on the final pH and surface loading. The dashed blue line in (b) shows maximum uptake around a final pH of 9. In (a), it can be seen that, to obtain this final pH, the slurry should be at an initial pH of 9 for very low SL (a highly diluted slurry), whereas at high SL, such as is the case for incipient wetness impregnation, an initial pH of 13 can be required (the SL at incipient wetness for a material with a surface area of 200 m²/g and pore volume of 1 mL/g is 200K m²/L). Adapted from ref 97. Copyright 2013 American Chemical Society.

dissolution of the support could be an issue at such extreme pH, it was reasoned that the buffering effect of the support would result in relatively fast pH equilibration, so that the pH drops to a value where the surface is charged but dissolution is less problematic. Using this method, 2 wt % Pt was deposited on carbon (PZC = 2, pH 13), silica (PZC = 4, pH 13), and alumina (PZC = 8, pH 1). Small particles between 1.5 and 3 nm in size were obtained, much smaller compared to those from a conventional dry impregnation whereby the pH of the impregnating solution was not optimized. Thus, CEDI provides the advantage of obtaining high dispersions without high amounts of wastewater, albeit at relatively low metal loadings.

The principles of strong electrostatic adsorption have also been used to selectively deposit metals on specific surface sites. Using the difference in PZC between Co₃O₄ (PZC = 8) and TiO₂ (PZC = 4), manganese was selectively deposited on cobalt in a Co₃O₄/TiO₂ catalyst by using KMnO₄ at a pH of 1, whereby the TiO₂ was negligibly charged.⁹⁸ Scanning transmission electron microscopy–electron energy loss spectroscopy (STEM–EELS) showed MnO was located preferentially on the Co₃O₄ (Figure 10), while samples prepared by conven-

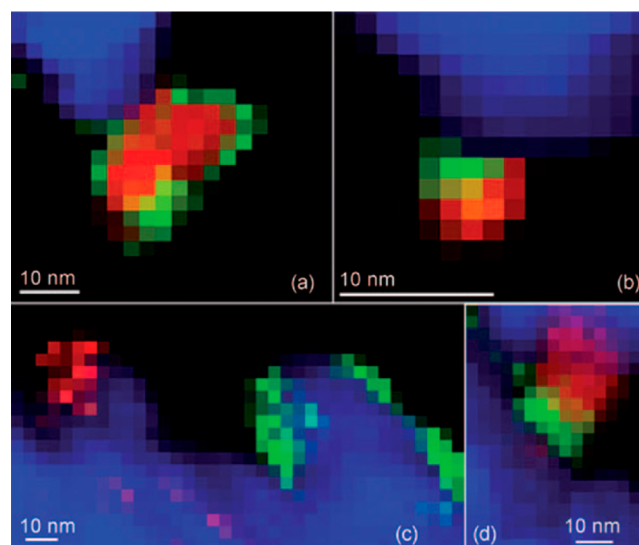


Figure 10. STEM–EELS map for Mn/Co/TiO₂. Strong electrostatic adsorption resulted in manganese (green) deposited on the cobalt (red) after calcination (a), which moved to the cobalt titania (blue) interface after reduction (b). By deposition via IWI, MnO was present on the TiO₂ support after calcination (c), which after reduction also migrated to the Co/TiO₂ interface (d). Adapted with permission from ref 99. Copyright 2010 Wiley.

tional incipient wetness impregnation whereby the pH was not regulated resulted in MnO dispersed all over the TiO₂ support.⁹⁹ However, reduction of the catalyst resulted in migration of the MnO in both cases to the Co/TiO₂ interface, which appeared to be thermodynamically favorable. Similar results were obtained for MnO/Co/SiO₂ and MnO/Rh/SiO₂, where MnO was preferentially adsorbed on Co₃O₄ or Rh₂O₃, respectively. However, no MnO migration was observed after reduction on the silica support.^{100,101}

Inner sphere complex formation concerns a chemical adsorption, whereby metal complexes are covalently coordinated to the hydroxyl groups (Figure 11). Because a charged complex is bonded to the support, this is generally compensated through the release or accumulation of protons by the support for a positive or negative metal complex, respectively, leading to a change in the pH of the impregnating solution. Therefore, to optimize procedures whereby inner sphere complex formation occurs, it is often important to actively regulate the pH during the equilibration procedure. In addition, adsorption can occur at a pH similar to the PZC, as described for Au on Al₂O₃ or TiO₂ (see section 3.2.1). The exact nature of adsorption depends on the support, precursor, and conditions, and often both inner and outer sphere complex formation can occur simultaneously.

In a series of papers, Lycourghiotis et al. investigated the method of adsorption on titania (PZC = 6.5, BET surface area

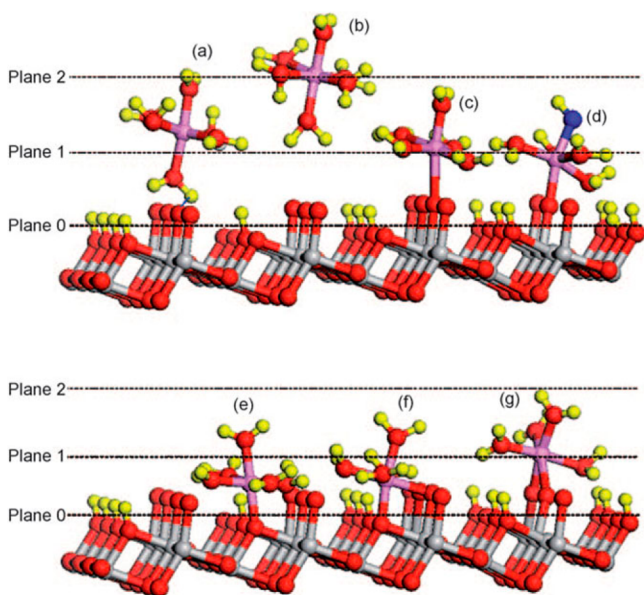


Figure 11. Schematic representation of various deposition possibilities of $\text{Co}(\text{H}_2\text{O})_6^{2+}$ on (101) anatase: (a) hydrogen bonding, (b) outer sphere complex formation via electrostatic adsorption, (c) inner sphere complex formation via monosubstitution of a H_2O ligand with a terminal surface oxygen atom, (d) monosubstitution with a hydrolyzed compound, (e) formation of a monosubstituted complex with a bridging surface oxygen, (f) formation of a disubstituted complex with one bridging and one terminal surface oxygen, (g) formation of a disubstituted complex with two terminal oxygen groups (Ti in gray, H in yellow, O in red, Co in pink, and oxygen of the hydrolyzed group in blue). Adapted with permission from ref 102. Copyright 2009 Wiley.

50 m^2/g) supported chromium, molybdenum, tungsten, cobalt, and nickel at various pH values ranging from below to above the PZC.^{102–106} It was found that CrO_4^{2-} , HCrO_4^- , and CrO_7^{2-} mainly adsorb through electrostatic forces to form outer sphere complexes, at a maximum of 1 wt % at pH 4.5.¹⁰⁵ However, the other metals all showed some form of covalent bonding of the metal precursor complex and the titania support. Mo and W complexes showed the highest adsorption of 3 and 10 wt %, respectively, at pH 4. Mainly mononuclear MoO_4^{2-} and WO_4^{2-} species were observed, whereby the complexes were formed via hydrogen bonds or substitution of one or two oxygen ligands with terminal oxygen groups of the titania. Polymeric species were also found in both cases when high initial concentrations and low pH were used, which adsorbed mainly through electrostatic forces. $\text{Co}(\text{H}_2\text{O})_6^{2+}$ and $\text{Ni}(\text{H}_2\text{O})_6^{2+}$ species preferentially adsorbed as mononuclear species, whereby one water ligand was replaced by a surface oxygen group, at a maximum of about 2 wt % at pH 7.5. In addition, one or more water ligands not bonding with the support could be hydrolyzed.

The knowledge of the type of species adsorbed at different pH values has allowed for the rational synthesis of supported catalysts. In the synthesis of 1.5 wt % $\text{MoO}_3/\text{TiO}_2$ catalysts, it was found that deposition at a constant pH of 6 resulted in much better dispersed catalysts as determined by XPS, which showed a $\text{Mo}/(\text{Mo} + \text{Ti} + \text{O})$ ratio of 2.2 compared to 1.3 for the catalyst prepared at pH 9.¹⁰⁷ It was postulated that the disubstituted MoO_4^{2-} that formed at pH 6, whereby two oxygen ligands of the precursor are replaced with terminal oxygen groups of the TiO_2 , was more stable to sintering during

subsequent calcination compared to the monosubstituted species which dominated at pH 9. Studies on $\text{Co}/\text{Al}_2\text{O}_3$ and $\text{Mo}/\text{Al}_2\text{O}_3$ illustrated the technique is not always easy, as deposition of large crystals or too strongly interacting species which were difficult to reduce also occurred depending on the conditions.^{108,109} Nonetheless, Kordulis et al. showed Co/Mo (2 wt %/17 wt %) bimetallic catalysts can be synthesized on an $\text{Al}_2\text{O}_3/\text{SiO}_2$ mixed support. Co-adsorption of ammonium heptamolybdate and cobalt nitrate at pH 5 resulted in the selective deposition of MoO_4^{2-} on the positively charged alumina, while the silica was negatively charged. Alternatively, Co was preferentially deposited on the silica surface, which resulted in fewer irreducible $\text{Co}/\text{Al}_2\text{O}_3$ sites. The resulting catalyst was over 10% more active for the hydrodesulfurization of thiophene compared to a similar one prepared via regular impregnation.

In the synthesis of 1 wt % Ni/SiO_2 catalysts using nickel ethylenediamine (en) complexes from nickel nitrate and ethylenediamine, the NiO species were controlled via different graftings of the nickel precursor complex.¹¹⁰ Both $\text{Ni}(\text{en})(\text{H}_2\text{O})_4$ and $\text{Ni}(\text{en})_2(\text{H}_2\text{O})_2$ were grafted onto the support via replacement of two H_2O ligands with surface hydroxyl groups. After calcination, grafted $\text{Ni}(\text{en})(\text{H}_2\text{O})_4$ gave rise to nickel phyllosilicate formation, eventually resulting in large nickel particles after reduction. However, grafted $\text{Ni}(\text{en})_2(\text{H}_2\text{O})_2$ brought about isolated Ni^{2+} ions after calcination, resulting in very small particles after reduction. This was attributed to the lack of free H_2O ligands in the adsorbed complex, so that it no longer reacted with other complexes or silicon-containing species.

4.2.2. Metal Distribution. Adsorption also plays a significant role in the metal distribution across macroscopic support grains or pellets.^{111,112} Although the pore filling with liquids of larger bodies occurs within a few seconds or minutes, adsorption on support sites often slows penetration of the precursor significantly. After short equilibration times, it is possible that metal precursor complexes are mostly adsorbed in the outer shell of the support body, resulting in an eggshell distribution. The details of an eggshell distribution will strongly depend on the equilibrium between adsorbed and solvated species. A longer equilibration time leads to diffusion of the metal complex toward the center of the catalyst body due to concentration gradients if the adsorption is at least to some extent reversible, so that eventually the system will converge to a homogeneous distribution. Addition of a second component that adsorbs more strongly than the precursor can result in egg-white or egg-yolk distributions (Figure 1). The additional component adsorbs in the outer shell, leaving no sites available for the metal precursor complex, which diffuses inward where more adsorption sites are available. Although this has been known for a long time, the subsequent drying step is also reported to have a large impact on the distribution, and direct monitoring of the distribution during impregnation is now possible by advanced spectroscopic techniques that have recently been developed.¹¹³

Using Raman spectroscopy, the impregnation of 3 mm γ - Al_2O_3 pellets (PZC = 9) with ammonium heptamolybdate (AHM) solutions at pH 5 or 9, leading to 15 wt % Mo, was followed over time.¹¹⁴ Because of the equilibrium between heptamolybdate and monomolybdate, $\text{Mo}_7\text{O}_{24}^{6-}$ was the predominant species at pH 5, while at pH 9 mainly MoO_4^{2-} was found. Upon impregnation with the solution at pH 9, close to the PZC of the γ - Al_2O_3 , the surface was minimally charged

and almost no interaction took place between the precursor and support, which led to a homogeneous MoO_4^{2-} distribution across the pellet after 10 min. With an impregnation solution of pH 5, the $\gamma\text{-Al}_2\text{O}_3$ was positively charged, and electrostatic adsorption of $\text{Mo}_7\text{O}_{24}^{6-}$ took place at the outer edges of the surface. At the same time, the buffering effect of $\gamma\text{-Al}_2\text{O}_3$ resulted in an increase in the pH and MoO_4^{2-} formation, which more easily diffused toward the inside of the pellet. Moreover, $(\text{NH}_4)_3[\text{Al}(\text{OH})_6\text{Mo}_6\text{O}_{18}]$ precipitated on the external surface, preventing a large part of the Mo from diffusing into the pellet altogether. When a $\gamma\text{-Al}_2\text{O}_3$ with a lower PZC of 8 was used, areas of high Mo concentrations were found throughout the pellet at long equilibration times with diagonally offset Raman spectroscopy and X-ray absorption tomography.^{115,116} These were attributed to the formation of $\text{Al}(\text{OH})_6\text{Mo}_6\text{O}_{18}^{3-}$ species throughout the support due to the lower buffering capacity of the alumina with PZC = 8 instead of 9 as in the previous study. This was mitigated by co-impregnation of a species that forms stable complexes with Mo^{6+} , such as citrate or H_3PO_4 , which resulted in homogeneous distributions after a sufficient time for equilibration.^{114,116}

The concentration of the precursor has also been found important, which can be explained by the limited adsorption capacity of a support surface. For $\text{Co}(\text{H}_2\text{O})_6^{2+}$ complexes impregnated on alumina, little interaction is expected between the positive complex and the protonated or neutral surface hydroxyls. Nonetheless, impregnation of a 3.85 mm $\gamma\text{-Al}_2\text{O}_3$ pellet with a low concentration (0.2 M) of $\text{Co}(\text{NO}_3)_2$ took 4 h for equilibration, as followed with ^1H magnetic resonance imaging (MRI),¹¹⁷ while in a different study impregnation of a 3 mm $\gamma\text{-Al}_2\text{O}_3$ pellet with a higher concentration (1.35 M) of $\text{Co}(\text{NO}_3)_2$ solution showed a homogeneous distribution already after 5 min.¹¹⁸ Bergwerff et al. further studied the impregnation of 0.2 M Co^{2+} by varying the pH and citric acid concentration using ^1H MRI.¹¹⁹ If no citric acid was added, a homogeneous distribution was obtained after 160 min at pH 1. Addition of citric acid at pH 1 did not lead to the formation of cobalt citrate complexes, so that competitive adsorption between $\text{Co}(\text{H}_2\text{O})_6^{2+}$ and free citric acid resulted in more rapid transport of Co^{2+} to the center of the 3.85 mm pellet, producing egg-yolk catalysts after 90 min of equilibration (Figure 12). At pH 5 and 9, cobalt citrate complexes formed which strongly adsorbed on the surface of the $\gamma\text{-Al}_2\text{O}_3$, resulting in eggshell distributions of varying degrees even after 48 h. However, addition of extra citrate to these solutions again resulted in competitive adsorption, so that the Co^{2+} complexes migrated toward the center more rapidly.

Nickel combined with ethylenediamine showed similar results. Upon impregnation of a 3 mm $\gamma\text{-Al}_2\text{O}_3$ pellet with 0.5 M $\text{Ni}(\text{H}_2\text{O})_6^{2+}$ and en at different Ni/en molar ratios (0, 1, 2, and 3), homogeneous $\text{Ni}(\text{H}_2\text{O})_6^{2+}$ and $\text{Ni}(\text{en})_3^{2+}$ distributions were found after 5 min for Ni/en ratios of 0 and 3, respectively.¹²⁰ At other ratios, $\text{Ni}(\text{en})_x(\text{H}_2\text{O})_{6-2x}^{2+}$ complexes formed which strongly adsorb, resulting in eggshell formations after 5 min, and a 2 h equilibrium period was necessary to obtain homogeneous distributions. On a 3.85 mm pellet, 5 min was not sufficient to obtain a homogeneous distribution upon impregnation of a 0.5 M $\text{Ni}(\text{H}_2\text{O})_6^{2+}$ solution.¹²¹ This relatively slow equilibration of weakly interacting species was attributed to partial hydrolysis and subsequent redissolution of nickel nitrate. While the PZC and surface area of this pellet were similar to those of the pellet used in the previous study, the

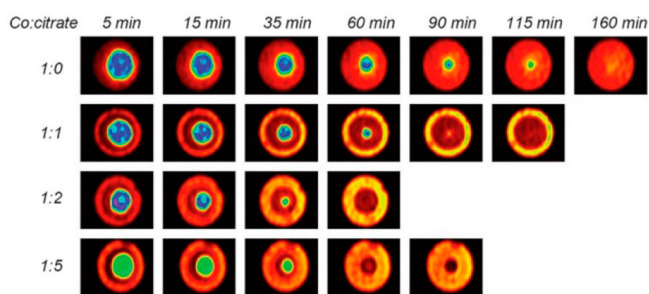


Figure 12. 2D ^1H MRI images recorded on an Al_2O_3 extrudate after impregnation with 0.2 M $\text{Co}(\text{NO}_3)_2(\text{aq})$ at pH 1 with different molar ratios of cobalt to citrate. The blue color indicates a low cobalt concentration, yellow indicates a medium cobalt concentration, and red indicates a high cobalt concentration. The higher the amount of citric acid, the faster cobalt migrated to the inside of the pellet, resulting in more concentrated egg yolks, while the eggshells with only medium cobalt concentrations (yellow) became larger. Adapted with permission from ref 119. Copyright 2008 Wiley.

difference might be attributed to the lower pore volume of the pellet, so that the amount of surface area per volume of impregnating solution doubled, allowing for more interaction with the support. Regardless, after 1 h a homogeneous distribution was found. Combined with ethylenediaminetetraacetic acid (EDTA) at a molar ratio of Ni/EDTA of 6 at pH 1 or 6, slight eggshell formations were found due to the formation and electrostatic adsorption of $\text{Ni}(\text{EDTA})^{2-}$ and $\text{Ni}(\text{EDTA-H})^-$ complexes in the external shell, while the remaining $\text{Ni}(\text{H}_2\text{O})_6^{2+}$ was homogeneously distributed throughout the rest of the pellet. Equilibration was faster at pH 1, for which less hydrolysis of $\text{Ni}(\text{H}_2\text{O})_6^{2+}$ species occurred. This difference in equilibration time based on pH was even more pronounced for $\text{Cr}(\text{H}_2\text{O})_6^{3+}$ complexes, where very defined eggshell profiles were formed at pH 4.5 due to hydrolysis of the precursor, while uniform distributions were obtained at pH 1.¹²² When CrO_4^{2-} complexes were used as the precursor, the roles were reversed. Strong electrostatic adsorption at low pH led to egg-white structures, while high pH led to limited interaction and therefore a homogeneous distribution. In this case, citric acid was found to limit hydrolysis of the Cr^{3+} complexes, while it also caused reduction of Cr^{6+} to Cr^{3+} , so that in most cases homogeneous distributions were obtained.

In the previous study, competitive adsorption was also studied using H_3PO_4 . This led to egg-yolk catalysts upon co-impregnation with Cr^{6+} species.¹²² Another example of competitive adsorption is Cl^- and PdCl_4^{2-} . Five minutes after impregnation, all PdCl_4^{2-} had hydrolyzed to $\text{PdCl}_2(\text{OH})_2^{2-}$ at the edge of the $\gamma\text{-Al}_2\text{O}_3$ pellet due to the basic surface OH groups, regardless of the Cl^- concentration and pH.¹²³ After 2 h, egg-white distributions were obtained at pH 1 because many sites at the edge of the pellet were protonated followed by adsorption of Cl^- , so that the $\text{PdCl}_2(\text{OH})_2^{2-}$ moved deeper into the pellet for adsorption on free sites. At pH 5, Cl^- adsorption was less favorable so that eggshell distributions were still detected. After 96 h each of the four main distributions (Figure 1) could be obtained depending on the conditions used. An egg-white distribution was obtained by strong and competitive Cl^- adsorption at low pH, which was limited to the outer shell of the pellet at low Cl^- concentration, while at higher Cl^- concentration more competitive adsorption resulted in an egg-yolk profile. At higher pH and low Cl^- concentration,

limited competitive adsorption resulted in an eggshell catalyst, while increasing the Cl^- concentration resulted in a more homogeneous distribution.

4.3. Drying

The drying step has long been known to have a strong influence on the final catalyst.^{112,124} Drying can be separated into three main stages, the increasing rate, constant rate, and falling rate periods. The increasing rate period concerns the time it takes for the system to attain the equilibrium drying temperature, which is slightly lower than the temperature set on the drying oven because evaporation is an endothermic process, but a pseudo steady state is generally achieved relatively rapidly. In the constant rate period, drying mainly occurs on the external surface of the drying grain or pellet. The system is in what is called a pendular state, whereby a continuous liquid exists throughout the particle, such that the solvent can be transported toward the external surface of the catalyst grain via capillary forces. If the precursor has a weak interaction with the support, it may be transported toward the external surface along with the solvent, resulting in a concentration buildup on the external rim of the support. As a consequence of the resulting concentration gradient, back-diffusion toward the inside of the grain can occur. At a certain time, the amount of solvent has been reduced to such an extent that capillary flow toward the external surface of the catalyst grain can no longer keep up with the rate of drying, and the drying front moves inward. As this happens, the drying rate slows as transport via the vapor is slower than via the liquid, and the liquid inside the pores becomes discontinuous, called the funicular state, so that isolated patches of liquid can form, and macroscopic redistribution at this stage becomes very limited.

As the solvent is removed during drying, the concentration of the precursor will rise, and once it reaches the critical supersaturation, precipitation will take place. Moreover, a chemical change of the precursor induced by dehydration, temperature, or a gas atmosphere can result in precipitation. As systems likely go through severe macroscopic redistribution across the catalyst grain or pellet during drying, precipitation can be important for the final macroscopic distribution of the active phase. It should be noted that many organic molecules such as citric acid or EDTA have previously been reported to change the viscosity of the impregnating solution.¹²⁵ This was recently shown in the preparation of 1–20 wt % Fe catalysts on $\alpha\text{-Al}_2\text{O}_3$ by Torres et al., who compared the effect of iron nitrate and ammonium iron citrate on the iron distribution of the final catalysts.¹²⁶ Iron particles of around 20 nm were found regardless of the precursor at loadings of 5 and 10 wt % Fe. However, iron nitrate resulted in high local loadings, while other parts of the support remained empty, whereas ammonium iron citrate led to a homogeneous distribution. This was attributed to the formation of a gel-like phase for the citrate precursor, thereby preventing redistribution. Addition of ethylene glycol (EG) in the preparation of 20 wt % Ni/MCM-41 catalysts prepared from nickel nitrate has been shown to prevent redistribution of nickel to the external surface during thermal treatment, which happened to a great extent when EG was not co-impregnated.¹²⁷ However, few other recent studies have been performed on the effects of the viscosity, although the addition of organic molecules has been used extensively to obtain a higher metal dispersion, which is discussed in the section on activation (4.4.1).

4.3.1. Drying of Strongly or Weakly Adsorbing Species. Since drying concerns movement of solvated species on a large scale, it is important to consider the degree of adsorption of the metal species in solution. Recently, Liu et al. modeled the effects of drying on porous bodies with different metal profiles after impregnation.⁷⁵ Although 0.25 M nickel nitrate was used as a case study, the developed methodology presented was not limited to specific active components or supports, and the interaction between the two could be parametrically varied. By varying the strength of adsorption of nickel nitrate to the support, and varying the nickel nitrate distribution after impregnation from homogeneous to eggshell, the effect of drying was studied. For a high adsorption strength, drying had little effect on the distribution, so that the main determining factor for the distribution was the impregnation step. A homogeneous distribution after impregnation remained homogeneous after drying, while eggshell distributions remained largely unchanged when the adsorption strength was high.

Recent improvements in spectroscopic techniques have enabled imaging of distributions after impregnation and drying, providing experimental evidence of the limited effect of drying on strongly adsorbing species. UV–vis and IR microspectroscopy showed nickel ethylenediamine complexes (0.5 M) with one or two en ligands grafted on γ -alumina did not redistribute during drying, whereas nonadsorbing $\text{Ni}(\text{en})_3^{2+}$ migrated toward the outside of the support.¹²⁰ Strongly adsorbing Pd species (0.1 M PdCl_4^- solution) on alumina were studied with UV–vis microspectroscopy, and were also found to retain the distribution they had obtained during impregnation after drying.¹²³ Using magnetic resonance imaging, cobalt nitrate at low concentration (0.2 M, pH 4) was found to adsorb sufficiently strongly to a γ -alumina surface to retain its eggshell distribution obtained during impregnation after drying.¹²⁸ Thus, these studies confirm that, for strongly adsorbing species, the drying step does not alter the macroscopic distribution of the precursor to a large degree.

For weakly adsorbing species and high concentrations, convection and back-diffusion during the drying step become very important. In the model of Liu et al., when the adsorption strength of nickel nitrate was reduced to a moderate value and assuming a homogeneous distribution after impregnation, drying could result in severe redistribution of the 0.25 M nickel nitrate solution on γ -alumina depending on the conditions.⁷⁵ Drying at 70 °C resulted in an almost homogeneous distribution. However, increasing the drying temperature to 300 °C resulted in eggshell distributions, because back-diffusion of nickel nitrate was not fast enough to compensate for the high drying rate. Similar results were obtained upon alteration of the humidity of the drying air; at 0.5% humidity, drying was relatively fast, resulting in an eggshell distribution, while drying in 10% humidity resulted in an almost homogeneous distribution. Finally, the size of the support pellet had a great influence on the distribution. A pellet diameter of 1 mm resulted in a moderate eggshell distribution whereby the concentration of nickel nitrate in the shell was 1.5 times higher than in the center of the pellet. For a 10 mm pellet, the concentration in the shell was almost 3 times higher compared to that in the center. The model was recently extended to a 3 mm γ -alumina pellet impregnated with nickel nitrate concentrations ranging from 0.005 to 4.0 M (Figure 13), and many of the results were compared to experimental data.^{129,130} A very low nickel nitrate concentration (0.005 M)

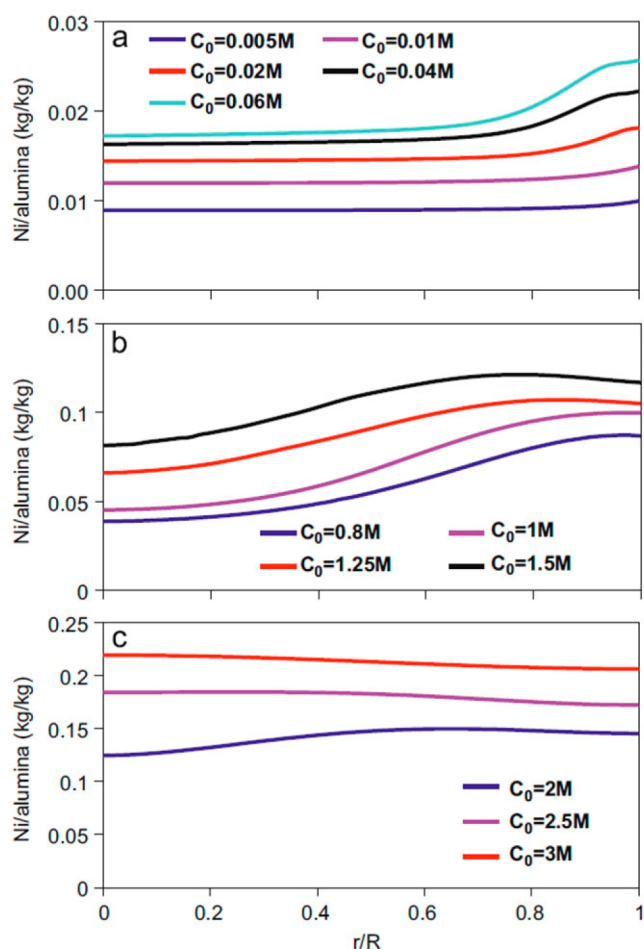


Figure 13. Simulated effect of the initial $\text{Ni}(\text{NO}_3)_2(\text{aq})$ concentration on the final metal profile across a 3 mm $\gamma\text{-Al}_2\text{O}_3$ pellet after drying at 80 °C, starting from a homogeneous distribution after impregnation: (a) low metal loadings, (b) moderate metal loadings, (c) high metal loadings. The loading of nickel is plotted as a function of the normalized radial distance r/R , whereby r is the distance from the center of the pellet and R is the pellet radius. Adapted with permission from ref 130. Copyright 2012 Elsevier.

resulted in homogeneous distributions after drying at 80 °C because most of the nickel nitrate remained adsorbed on the γ -alumina. At a slightly higher concentration (0.06 M), the amount of nickel nitrate exceeded the adsorption capacity of the support, and an eggshell distribution was obtained due to convective redistribution toward the edge of the pellet. Although back-diffusion gave rise to partial mitigation of this redistribution, the system entered the falling rate period relatively rapidly, so that film breakage occurred and material was no longer transported across large distances. At even higher concentrations (3 M), the precursor was also initially transported toward the outer edge of the pellet, but the concentration was so high that film breakage did not occur, so that sufficient back-diffusion time resulted in a homogeneous distribution. It should be noted that, in these model systems, only the solvent water was removed, leaving the nickel nitrate hexahydrate, which melts in its own crystal water above 56 °C, intact. Nonetheless, good agreement was found between the model predictions and real experiments, suggesting macroscopic distribution occurs mainly during the removal of the solvent, not removal of the crystal water of metal nitrates.

An interesting consequence of these considerations is that precursor material present on the external surface of the catalyst grain or pellet does not necessarily mean it will be deposited there during drying. If material remains on the external surface during impregnation, capillary flow can still pull it in when part of the pore volume becomes accessible again due to (partial) evaporation of the solvent, assuming the material on the external surface is still dissolved or can be molten. The latter case closely resembles melt infiltration, which will be discussed in detail in section 5.1.

Other experimental evidence on redistribution of the precursor during drying has been reported in recent years. Impregnation of a basic AHM solution (1.8 M, pH 9) onto γ -alumina resulted in little interaction with the support, so that redistribution toward the external portion of the pellet resulted in eggshell distributions.¹³¹ Alternatively, addition of H_3PO_4 to an impregnation of γ -alumina with AHM resulted in surface adsorption of PO_4^{3-} , so that the support surface was not significantly charged even at pH 2, together with complex formation of the form $\text{H}_x\text{P}_2\text{Mo}_5\text{O}_{23}^{6-x}$.¹¹⁶ While normally AHM would adsorb to the alumina surface at this low pH, the negatively charged complex only weakly interacted with the PO_4 surface groups, so that redistribution of the complexes also resulted in eggshell distributions. As mentioned earlier, weakly interacting $\text{Ni}(\text{en})_3$ complexes redistributed during drying, resulting in eggshell profiles.¹²⁰ Clearly, weakly interacting species can migrate over macroscopic distances during the drying step.

4.3.2. Metal Redistribution at the Nanoscale. Macroscopic distributions can be largely avoided by reducing the grain size of the support. This is often done in academia to rule out the effect of macroscopic distributions on the catalyst performance. However, even though support grains might be homogeneously distributed on the macroscale, inhomogeneities are frequently reported on the nanoscale. The active metal is often located in large clusters or aggregates, while a large part of the support remains empty. These aggregates can be much larger than the average pore diameter, and the nanoparticles often form an intricate network throughout the pore structure.¹³² Moreover, the crystallites inside these aggregates have been observed to have an overall crystallographic alignment, suggesting they are closely linked to each other or were at some point during their synthesis.¹³³ Methods to prevent this include modification of the support or co-impregnation of organic molecules.^{134,135} However, recent studies revealed these inhomogeneous distributions can be circumvented by careful control of the drying step.

Using Stöber silica spheres impregnated with nickel nitrate solutions, Banerjee et al. used environmental TEM to study the distribution of the nickel phases during preparation. It was shown that inhomogeneous distributions obtained after in situ drying of an aqueous solution largely remained after calcination and reduction, while use of ethanol as a solvent resulted in more homogeneous distributions, which was attributed to the lower surface tension of ethanol.¹³⁶ Munnik et al. used a silica gel (38–75 μm grains) impregnated with a 4.2 M aqueous cobalt nitrate solution, close to saturation, and opted for drying in a N_2 flow in a fluidized bed reactor at different temperatures instead of the often-practiced stagnant drying in a muffle oven, followed by calcination at 350 °C in a N_2 flow.¹⁶ While all of the samples displayed uniform cobalt distributions on the macroscale, drying at 25 °C followed by calcination resulted in 8 nm cobalt oxide particles clustered together in aggregates of

40 nm size. Increasing the drying temperature gradually reduced the aggregate size until at 100 °C the 8 nm particles were homogeneously distributed over the support and no aggregates were found. However, a further increase of the drying temperature to 150 °C resulted again in aggregate formation, up to 80 nm in size (Figure 14). This behavior was

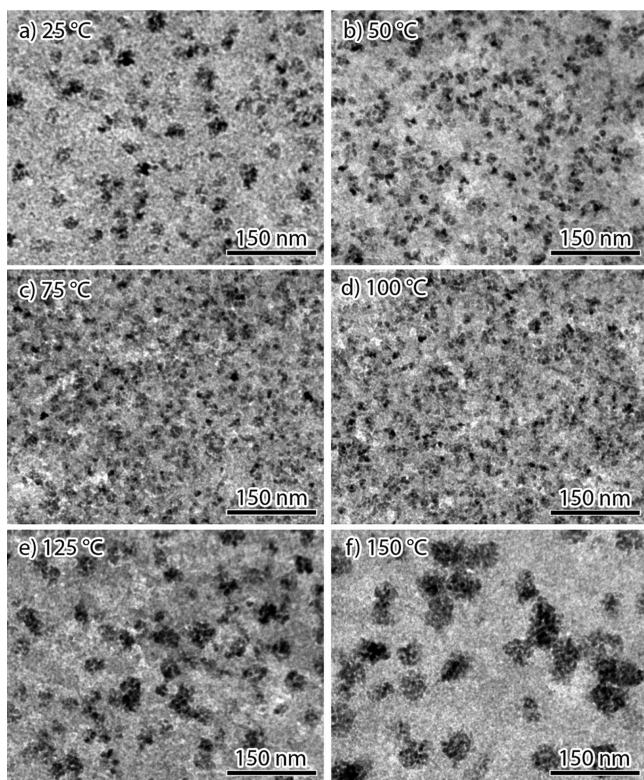


Figure 14. TEM images of calcined $\text{Co}_3\text{O}_4/\text{SiO}_2$ after drying treatments in a N_2 fluidized bed at different temperatures: (a) 25 °C, (b) 50 °C, (c) 75 °C, (d) 100 °C, (e) 125 °C, (f) 150 °C. Different extents of cobalt aggregation (black) were observed on the silica support (gray) depending on the drying temperature. The size of the primary cobalt oxide nanoparticles was ~ 9 nm in all cases. Adapted from ref 16. Copyright 2014 American Chemical Society.

further studied by performing a calcination in a gas flow of 1% NO/N_2 after the drying treatment, which resulted in immobilization of the cobalt nitrate precursor via cobalt hydroxynitrate formation, so that further redistribution after drying was not possible.¹³⁷ After drying at 25 °C and calcination in a NO/N_2 gas flow, 3–4 nm cobalt oxide particles were found in large irregularly shaped aggregates up to 200 nm in size. Increasing the drying temperature reduced the size of the aggregates, until at 100 °C a homogeneous distribution of 3–4 nm cobalt particles was obtained.¹³⁸ A further increase of the temperature resulted in 8 nm cobalt particles in increasingly large aggregates. It was postulated that aggregation originated from two separate mechanisms. At low temperature, precipitation of a cobalt nitrate species occurred when the concentration reached supersaturation. If the drying rate is low, nucleation of this species is relatively slow so that growth becomes very significant, resulting in large cobalt nitrate islands, while other areas on the support become depleted. Raising the temperature increased the drying rate, so that the nucleation rate increased and smaller islands were formed, eventually resulting in a homogeneous distribution at 100 °C.

This behavior shows a resemblance to what is observed in the drying of colloidal wet films^{139,140} and suggests that at low temperature aggregate formation is mainly a physical process. At temperatures above 100 °C, nucleation and growth of cobalt oxide due to decomposition of cobalt nitrate was found to occur during drying. As this mainly occurred in the presence of a large amount of water, either in liquid or vapor form, the cobalt nitrate was highly mobile and nucleation and growth of cobalt oxide resulted in increasingly larger aggregates.¹³⁸

The effect of precursor–support interactions was also investigated for a γ -alumina support. While stagnant drying in a muffle oven between 60 to 120 °C always resulted in 8 nm cobalt particles located in 30–60 nm aggregates after calcination in a N_2 flow, drying in a fluidized bed between 25 and 100 °C resulted in the 8 nm particles being uniformly distributed throughout the support after calcination.¹³⁸ At 150 °C, aggregates of 30–40 nm size were found, somewhat smaller than on silica. Thus, it appeared that the increased support–precursor interactions of the γ -alumina inhibited aggregate formation. Moreover, although drying in stagnant air always resulted in aggregates, drying using a N_2 flow resulted in uniform distributions, showing the importance of rapid removal of water during the drying process. It should be noted that fast drying can have a negative effect on the macroscopic distribution across catalyst grains when precipitation occurs without sufficient time for back-diffusion, as mentioned in the previous section and observed for silica with larger pores of 23 nm.

Aggregate formation due to a long retention time of water vapor has also been used for the synthesis of nanocast materials. Starting from iron nitrate, large iron oxide aggregates up to 2000 nm in size were synthesized on an ordered mesoporous silica support by covering up the sample container during a heat treatment to 150 °C.¹⁴¹ Similar results were found for cobalt, nickel, indium, manganese, cesium, and chromium oxides when starting from the respective metal nitrates, showing the importance of the water pressure during drying and decomposition of metal nitrate hydrates in general.

4.3.3. Alternative Drying Methods. While drying is most often performed in stagnant air in a regular muffle oven, other alternatives besides fluidized bed drying are available that alter the rate of drying or the drying process, and so influence the distribution of the active metal phase. In freeze-drying the precursor is frozen after impregnation, followed by sublimation of the immobilized solvent at reduced temperature and pressure. Eggenhuisen et al. performed freeze-drying on SBA-15 impregnated with nickel or cobalt nitrate by freezing in liquid nitrogen and drying at -55 °C under reduced pressure.⁷⁹ Using cryo-TEM tomography to visualize the dried samples, it was shown that freeze-drying resulted in homogeneous distributions of cobalt nitrate after drying, whereas inhomogeneous distributions were obtained after conventional drying at 60 °C (Figure 15). This difference in nanoscale distribution was largely maintained after a thermal activation was performed, illustrating the drying step is highly important for the final metal distribution at the nanoscale. The method was also shown to work on a silica gel for cobalt nitrate and nickel nitrate.^{24,142} However, freezing the precursor required great care.¹⁴² When a liquid is confined in nanometer-sized pores, the freezing and melting points can be greatly depressed. While a 4.2 M cobalt nitrate solution froze at about -30 °C, confinement in a silica gel with 8 nm pores caused a freezing point depression to -90 °C. Thus, to properly freeze and dry

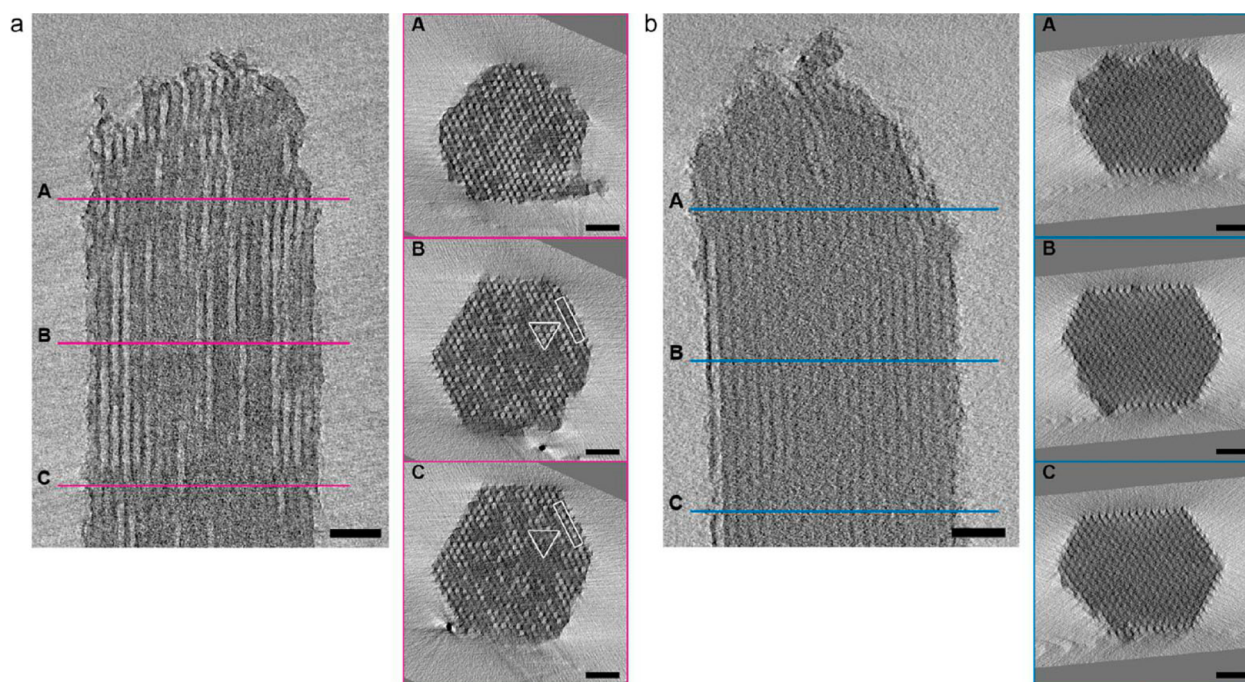


Figure 15. Cryo-TEM tomography results of $\text{Co}(\text{NO}_3)_2$ salt distribution in mesoporous SBA-15 after different drying treatments: (a) dried at $60\text{ }^\circ\text{C}$ in a muffle oven, showing an inhomogeneous distribution after drying (triangles and rectangles in (B) and (C) indicate examples of pores with inhomogeneous fillings), (b) dried by freeze-drying, showing a homogeneous distribution after drying. All scale bars are 50 nm. Lines A, B, and C indicate the positions of the cross-sections. Bright dots and lines are empty pores; dark areas are filled pores. Adapted from ref 79. Copyright 2013 American Chemical Society.

the impregnated sample, a temperature of $-90\text{ }^\circ\text{C}$ or lower should be applied. Therefore, although liquid nitrogen temperatures were sufficient to freeze the confined precursor, $-45\text{ }^\circ\text{C}$ was not sufficient to solidify the precursor, and redistribution was observed over the macroscopic catalyst grains, creating distinct eggshell distributions.

Microwave drying provides another alternative. It has the potential to speed up drying drastically due to the volumetric heating of the material, removing the need for heat transport from the outer edge of the particle toward the center. Liu et al. studied microwave drying on 3 mm pellets impregnated with different concentrations of nickel nitrate solutions from 0.1 to 2 M.¹³⁰ In all cases, homogeneous macroscopic distributions across the pellet were obtained. Moreover, the drying step was completed in a relatively short amount of time. It was proposed that uniform drying reduced convection so that more homogeneous distributions were obtained.

4.4. Activation

In the activation step the deposited metal precursor is converted into the active phase. Generally, this is done by a calcination step, resulting in the metal oxides, followed by a reduction if metallic particles are required. Next to metals, common active phases include metal oxides or metal sulfides.

4.4.1. Formation of the Active Phase. The activation treatment leads to the formation of nanoparticles, and often has a large influence on the final particle size. Moreover, although most treatments remain below the melting point of the active materials, the temperatures used can easily exceed the Hüttig temperature ($T_{\text{Hüttig}} = 0.3T_{\text{melt}}$), around which defect sites on metal particles become mobile, or even the Tammann temperature ($T_{\text{Tammann}} = 0.5T_{\text{melt}}$), whereby surface atoms become mobile, which can lead to particle growth via migration and coalescence of the particles or via Ostwald ripening.

Although direct reduction of many precursors can lead to well-dispersed catalysts, direct reduction is often highly exothermic and can lead to mixed metal–support phases. Moreover, it can produce a pyrophoric catalyst that needs to be passivated, often making it impractical for use on an industrial scale. Therefore, a calcination procedure is usually performed to form the pure metal oxide particles before further treatment such as reduction. Both the heating rate and air flow during calcination have been shown to be highly important for the preparation of 23 wt % $\text{Co}/\gamma\text{-Al}_2\text{O}_3$ catalysts for the Fischer–Tropsch synthesis. Heating rates between 0.1 and $1\text{ }^\circ\text{C}/\text{min}$ resulted in similarly active catalysts; however, higher heating rates of 4 and $8\text{ }^\circ\text{C}/\text{min}$ significantly reduced the activity when calcined to $250\text{ }^\circ\text{C}$.¹⁴³ Air flows of $1\text{ m}^3/(\text{kg}_{\text{Co}(\text{NO}_3)_2}\cdot\text{h})$, roughly corresponding to a gas hourly space velocity (GHSV) of 2000 h^{-1} , and higher during calcination resulted in similar catalysts with a cobalt surface area of $11\text{ m}^2/\text{g}$; however, at lower flows cobalt surface areas as low as $6\text{ m}^2/\text{g}$ were obtained. In a separate study, flows higher than the above-mentioned $1\text{ m}^3/(\text{kg}_{\text{Co}(\text{NO}_3)_2}\cdot\text{h})$ were used to investigate the gas composition and calcination temperature in the synthesis of 20 wt % $\text{Co}/\gamma\text{-Al}_2\text{O}_3$.¹⁴⁴ Although calcination at temperatures between 150 and $500\text{ }^\circ\text{C}$ for 10 h showed almost complete decomposition of the cobalt nitrate regardless of the temperature, dispersions of around 9% were found at $150\text{ }^\circ\text{C}$, whereas at $400\text{ }^\circ\text{C}$ this was slightly lower (7.5%). Upon testing the gas composition, only 50% steam/air produced lower cobalt dispersions, whereas little difference was observed between N_2 and air.

Sietsma et al. studied the calcination of nickel nitrate on SBA-15 (24 wt % Ni).¹⁴⁵ After drying at $120\text{ }^\circ\text{C}$, the precursor was found only inside the pores of the SBA-15 support, in the form of 9 nm crystallites of $\text{Ni}_3(\text{NO}_3)_2(\text{OH})_4$, similar to the pore size of the support. Thermal decomposition of this phase

in stagnant air resulted in severe redistribution and large particles on the external surface of the support (Figure 16). In a

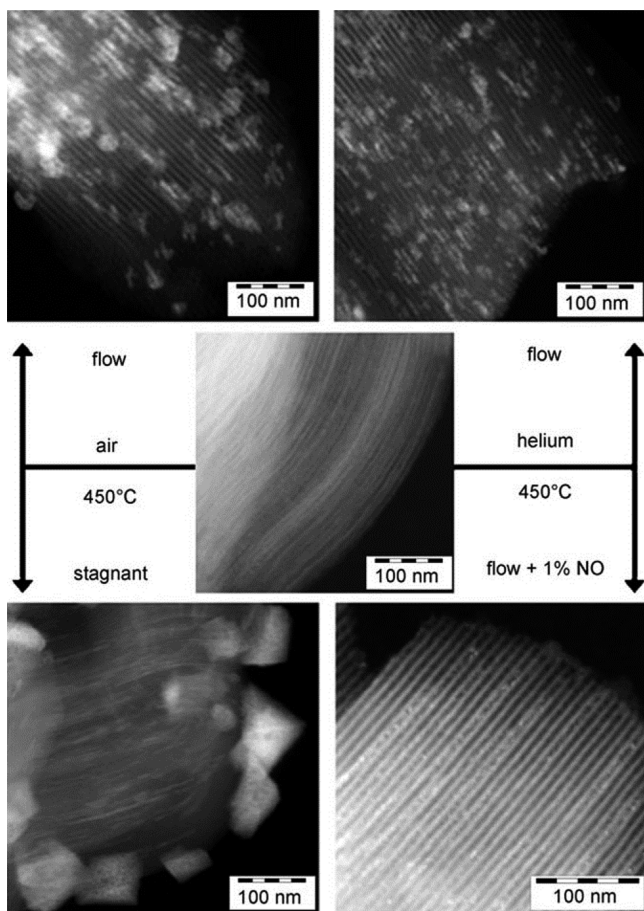


Figure 16. HAADF-STEM (high-angle annular dark field scanning transmission electron microscopy) images of Ni/SBA-15 after drying at 120 °C (center) and after calcination in different gas atmospheres at 450 °C. After drying, nanowires of basic nickel nitrate were observed exclusively inside the mesopores of SBA-15. Calcination in stagnant air resulted in large NiO crystals on the external surface of the support particle. Calcination in air or helium flow gave rise to smaller NiO particles, while calcination in 1% NO led to very small particles of about 4 nm. Adapted with permission from ref 145. Copyright 2007 Wiley.

flow of air, the particle size was decreased, and a further improvement was obtained in a flow of He, suggesting decomposition in a flow and an O₂-free environment was beneficial for the metal dispersion. The highest dispersion was obtained in a flow of 1% NO/He, which resulted exclusively in small 4 nm NiO particles inside the mesopores of the support. Further investigation on Ni/SBA-15 showed that addition of NO₂ or O₂ to the gas stream, both decomposition products of Ni₃(NO₃)₂(OH)₄, was detrimental for the metal dispersion and resulted in large particles and migration toward the external surface of the SBA-15 particles.⁷⁸ Moreover, NO concentrations as low as 0.1 vol % were already enough to reduce the NiO particle size from 11 to 4 nm at a GHSV of 24 500 h⁻¹. Reduction of the GHSV at a NO concentration of 1 vol % showed little impact until a GHSV of 7000 h⁻¹, while further reduction resulted in gradually larger particles.¹⁴⁶ Additional IR, MS, and isotopic labeling studies revealed that NO scavenges oxygen radicals from the nitrate during decomposition.¹⁴⁷ It

was proposed that when a nitrate group becomes unstable during the thermal treatment, NO reacts with the formed oxygen radical, thereby shifting the equilibrium toward NiO and so creating a NiO nucleus. As this occurs at lower temperatures and because a larger number of nuclei are present, many small particles result, and extensive sintering or migration is prevented. If NO is not present during decomposition, oxygen radicals will combine to form O₂. This was proposed as the rate-determining step, and moreover was postulated to be catalyzed by the formed NiO so that nucleation would start an autocatalytic process, causing the entire Ni₃(NO₃)₂(OH)₄ crystallite to rapidly decompose, resulting in large particles.

Wolters et al. further investigated the decomposition of scandium, manganese, iron, cobalt, nickel, copper, and zinc nitrates impregnated onto silica gel and SBA-15 at metal loadings between 6 and 16 wt %.¹⁴⁸ After impregnation with the 3 M metal nitrate solution, the samples were dried in a desiccator at room temperature to prevent premature decomposition of the nitrates, followed by thermal treatment in Ar or 1% NO/Ar at 1 °C/min. For all metals, addition of NO was found to lower the decomposition temperature significantly by about 50 °C. However, for Sc, Mn, Fe, and Zn, no crystalline phases were detected by XRD after decomposition in either Ar or NO/Ar flow. For Co, Ni, and Cu, addition of NO resulted in rapid hydrolysis of the metal nitrate to its respective metal hydroxynitrate, which resulted in significantly lower metal oxide particle sizes of 5, 4, and 7 nm after decomposition, respectively, compared to averages of 10, 12, or 23 nm obtained in air. By varying the pore size of the ordered mesoporous support between 2.5 and 10 nm, it was shown that the formed nickel hydroxynitrate crystallites obtained after drying were of a size similar to that of the pores, and that the size of the final NiO particles obtained after calcination depended on the original size of these crystallites.¹⁴⁹ Quick X-ray absorption spectroscopy on cobalt nitrate impregnated on silica at a Co loading of 10 wt % also revealed rapid formation of cobalt hydroxynitrate below 100 °C in the presence of 5% NO/He, which further decomposed to Co₃O₄ between 110 and 170 °C.¹⁵⁰ Furthermore, temperature-programmed calcination on cobalt nitrate melt infiltrated (see section 5.1) on γ-Al₂O₃, followed by drying at 85 °C in air, revealed the hydrolysis of cobalt nitrate during a NO thermal treatment and subsequent improved particle size after decomposition also occurred on γ-Al₂O₃.¹⁵¹ However, the resulting increase in cobalt specific surface area of up to 33% for catalysts prepared using NO was less compared to the increase with silica. Using temperature-programmed reduction–X-ray absorption fine structure (TPR–XAFS) spectroscopy, Jacobs et al. also observed that the effect of NO on the dispersion is larger on silica compared to γ-alumina, and attributed this to the strong interaction between γ-alumina and cobalt nitrate, which already results in relatively small particles.¹⁵² Therefore, it was postulated that the effect of NO would work best on supports such as silica that exhibit a weak interaction with the precursor.

Further study on the decomposition of copper nitrate impregnated on SBA-15 and silica gel (18 wt % Cu) confirmed the formation of copper hydroxynitrate at temperatures below 100 °C in the presence of 2 vol % NO, which subsequently decomposes directly into CuO at 200 °C, leading to small 6–8 nm particles.¹⁵³ However, when NO was not present, a higher copper dispersion was obtained in air flow with GHSV as low as 250 h⁻¹. Although large 30 nm CuO crystallites were detected

by XRD, N_2O chemisorption for the reduced catalyst revealed a relatively high Cu surface area of $90 \text{ m}^2/\text{g}_{\text{Cu}}$, indicating small particles dominated. From diffuse reflectance infrared Fourier transform (DRIFT) measurements during calcination, it was concluded that the high dispersion originated from the mobilization of copper nitrate anhydride, which rapidly redispersed over the support surface anchored by silanol groups, ultimately resulting in very small CuO particles. The large CuO particles were the result of a small amount of poorly dispersed copper hydroxynitrate which formed even in the absence NO. Such premature hydrolysis during the initial stages of the thermal treatment may be largely avoided by vacuum-drying at room temperature. When this was performed on SBA-15 impregnated with a 4 M copper nitrate solution for 12 h, no large crystallites were found after calcination at $500 \text{ }^\circ\text{C}$ in a N_2 flow ($\text{GHSV} = 1000 \text{ h}^{-1}$).¹⁵

4.4.2. Chelating Additives and Other Organic-Containing Precursors. Organic precursors or additives are frequently used for the synthesis of supported catalysts, in particular for hydrodesulfurization (HDS) catalysts such as alumina-supported CoMoS, NiMoS, CoWS, and NiWS. For these catalysts the active phase consists of MoS_2 or WS_2 slabs decorated with Co or Ni atoms located at the edges, which are commonly prepared by co-impregnation of the metal precursors followed by drying, calcination, and sulfidation. However, under standard conditions, sulfidation of cobalt or nickel occurs prior to that of molybdenum or tungsten, resulting in undesired Co_9S_8 or Ni_2S_3 phases. Chelating agents are used among others to retard sulfidation of cobalt and nickel, so that they are only sulfidized after MoS_2 or WS_2 phases have formed and the cobalt or nickel can be efficiently deposited at the edges of the slabs. For CoMoS catalysts, a moderately strong chelating agent such as nitrilotriacetic acid (NTA) offers sufficient retardation,¹⁵⁴ whereas NiMoS catalysts require slightly stronger complexing agents such as EDTA.¹⁵⁵ Because tungsten is sulfidized at a higher temperature than molybdenum, formation of CoWS and NiWS catalysts generally requires even stronger complexing agents.^{156,157}

More recently, research has focused on the use of chelating agents for the preparation of cobalt Fischer–Tropsch catalysts. In an extensive study, 5 wt % Co/SiO₂ catalysts were prepared by incipient wetness impregnation of cobalt nitrate and NTA, EDTA, or *trans*-1,2-diaminocyclohexane-*N,N,N',N'*-tetraacetic acid (CyDTA) at equal nitrate/chelate molar ratios and a pH of 9–10 to ensure chelation of $\text{Co}^{2+}(\text{aq})$.¹⁵⁸ After impregnation, samples were dried at $120 \text{ }^\circ\text{C}$, calcined in stagnant air at $450 \text{ }^\circ\text{C}$, and reduced at $500 \text{ }^\circ\text{C}$. A correlation was found between the cobalt dispersion and the complex formation constant of the chelating agent, showing increasingly smaller particles going from no chelate to NTA to EDTA to CyDTA. However, for EDTA and CyDTA, the particles were difficult to reduce due to the formation of cobalt silicates. Glycine, citric acid, aspartic acid, and triethylenetetramine-*N,N,N',N',N'',N''*-hexaacetic acid (TTHA) were tested in a separate study, but exhibited lower Co dispersion compared to NTA.¹⁵⁹ The catalytic activity of Co was correlated to the complex formation constants of the organic additives with Co^{2+} in a volcano-type plot (Figure 17), suggesting a moderately strong complexing agent offers the best compromise of obtaining small yet reducible particles. Further investigation on NTA showed a $\text{Co}^{2+}/\text{NTA}$ molar ratio of 1 resulted in the highest dispersion, and that a calcination temperature of $450 \text{ }^\circ\text{C}$ was optimal.¹⁶⁰

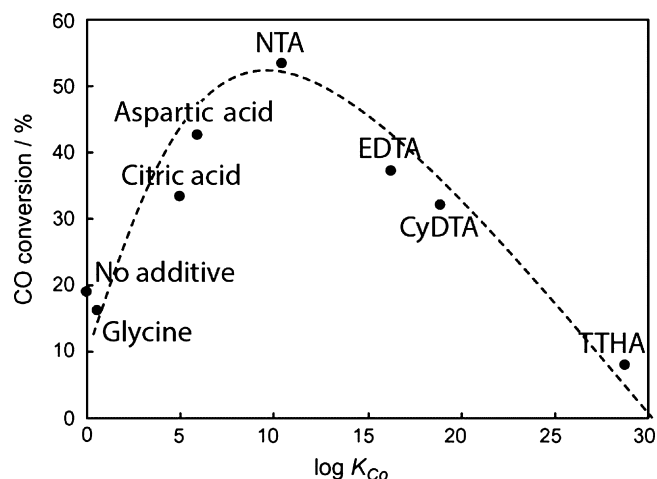


Figure 17. Relationship between the CO conversion in the Fischer–Tropsch synthesis of reduced Co catalysts and the complex formation constant of the organic acids and chelating agents used during the catalyst preparation. The CO conversion was proportional to the dispersion after reduction, which exhibited a similar relationship with $\log K_{\text{Co}}$. Adapted with permission from ref 160. Copyright 2009 Elsevier.

Due to the presence of chelating agents, the concentration of the impregnation solution and thereby the resulting metal loading are relatively low. To cope with this challenge, a stepwise impregnation was proposed, whereby silica was first impregnated with the chelating agent (NTA or CyDTA) and dried at $120 \text{ }^\circ\text{C}$, after which cobalt nitrate was impregnated with weight loadings up to 20 wt %. At these loadings both NTA- and CyDTA-prepared catalysts exhibited very good reducibility and similar activities.¹⁶¹ Further investigation of the 20 wt % Co catalyst with a Co/chelate ratio of 4 showed only one-fourth of the CyDTA was complexed with Co^{2+} in the dried material, resulting in the suppressed particle growth of Co_3O_4 during calcination through stabilization of small cobalt clusters that served as nuclei.¹⁶²

Glycols are a popular alternative to improve the dispersion of cobalt catalysts. Borg et al. prepared γ -alumina- and α -alumina-supported catalysts with Co loadings of 12, 20, and 30 wt % by impregnation with cobalt nitrate and different ratios of water/ethylene glycol as the solvent.¹³⁵ After impregnation, samples were dried at $110 \text{ }^\circ\text{C}$ and calcined in air at $300 \text{ }^\circ\text{C}$. On both supports, Co_3O_4 particles became smaller upon increasing the amount of ethylene glycol relative to water, from 16 nm to as low as 4 nm, and addition of EG resulted in more uniform particle distributions. The authors postulated that EG works as a surfactant, resulting in better wetting of the support, although the impact of EG on the drying and calcination steps was not excluded in this work. This glycol method was subsequently used to prepare a wide range of particle sizes on γ -, δ -, θ -, and α -aluminas.^{163,164}

The difference between straight chains (ethylene glycol, diethylene glycol (DEG), triethylene glycol (TEG)) or branched (glycerol, pentaerythritol) glycols has been investigated for the preparation of 10 and 20 wt % Co/SiO₂ catalysts at different Co/glycol molar ratios between 0 and 1.^{165,166} After impregnation, the samples were dried at $120 \text{ }^\circ\text{C}$ and calcined in stagnant air at $450 \text{ }^\circ\text{C}$. A reduction in crystallite size from 35 to 10 nm was observed; however, the resulting Co_3O_4 crystallite sizes did not depend on the specific glycol, but rather on the atomic ratio of carbon to Co^{2+} (Figure 18), while no further

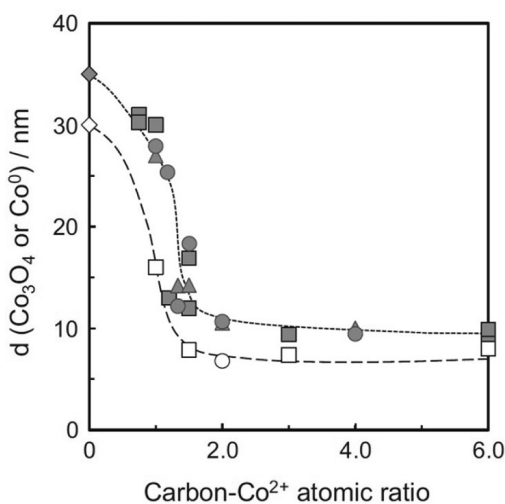


Figure 18. Impact of the amount of atomic carbon relative to Co^{2+} present in the impregnating solution for the preparation of 20 wt % Co/SiO_2 . Closed symbols represent Co_3O_4 measurements after calcination and open symbols metallic Co after reduction. Key: circles, EG; triangles, DEG; squares, TEG. Adapted with permission from ref 165. Copyright 2011 Elsevier.

improvement was found above a carbon/Co ratio of 2. FTIR investigation of TEG samples suggested a polymer-complex-like species was formed during calcination through ester polymerization of TEG with its derivatives, thereby preventing excessive growth of particles. Other sugar additives have been used with mixed success. Co-impregnation of sorbitol for the preparation of 10 wt % Co/SiO_2 samples has led to poorly reducible cobalt,¹⁶⁷ while addition of sucrose did not change the reducibility of 6–8 wt % Co/SiO_2 .¹⁶⁸ In the latter case, the catalysts were also promoted with Ru or Re, suggesting a reduction promotor may be necessary when using sugar-derived additives.

Organic precursors are a popular alternative to inorganic metal salts. Cobalt nitrate and acetate have been compared for the preparation of 10 wt % Co/SiO_2 catalysts by incipient wetness, drying at 90 °C, and calcination at 400 °C.¹⁶⁹ Cobalt nitrate exhibited an endothermic calcination, favoring the formation of agglomerated 20 nm Co_3O_4 crystallites, while acetate decomposed exothermically during calcination, resulting in the formation of cobalt silicates, which hamper reduction. Comparison of cobalt nitrate, acetate, and chloride for the synthesis of 20 wt % Co/AlPO_4 by impregnation, drying at 110 °C, and calcination at 500 °C showed similar results, while cobalt chloride gave rise to very large 35–160 nm crystallites.¹⁷⁰ Nickel nitrate and acetate have been compared for the deposition of 1 or 5 wt % Ni/MCM-41 by the two-solvent impregnation. After drying at 90 °C and calcination in an air flow at 500 °C, nickel acetate was shown to produce smaller NiO particles compared to nickel nitrate, while only a limited amount of nickel silicate was found.⁸² Wet impregnated nickel glycinate on γ -alumina at a nickel loading of 15 or 28 wt % resulted in 5–30 nm nickel particles after drying at 80 °C and calcination at 500 °C in an argon flow.¹⁷¹ Using the glycinate precursor, both hexagonal close-packed (hcp) and face-centered cubic (fcc) Ni phases were detected, whereas normally fcc is the dominant phase. Incipient wetness impregnation of γ -alumina has been performed with nickel ethylenediamine nitrate or nickel nitrate hexahydrate (14–15

wt % Ni), followed by drying at 100 °C, calcination at 500 °C, and reduction at 500 °C.¹⁷² The Ni(en) precursor resulted in a metallic nickel surface area of 13 $\text{m}^2/\text{g}_{\text{cat}}$, whereas nickel nitrate resulted in 6 $\text{m}^2/\text{g}_{\text{cat}}$. Moreover, Ni(en) did not lead to formation of nickel aluminate, whereas this was found in significant amounts for nitrate samples. These results show that although organic precursors can result in smaller particles, the conditions during thermal treatment and the nature of the support have a large influence on the formation of mixed metal–support phases which are difficult to reduce, which was more severe for cobalt than for nickel precursors.

4.4.3. Plasma Activation. Although thermal activation treatments are conventionally used to decompose and reduce the metal precursors, cold plasma techniques are receiving increased attention. Especially glow discharge plasma is of interest, due to its ability to provide reduced catalysts when working with noble-metal precursors without the need for a reducing agent. In glow discharge plasma, the sample is loaded into a special reactor, followed by evacuation of the reaction chamber to around 100 Pa. After this the gas is introduced, often H_2 , Ar, or N_2 , and a voltage is applied to generate the plasma. Using this method, 2–3 wt % Pt, Pd, Ag, or Au was prepared on TiO_2 , $\gamma\text{-Al}_2\text{O}_3$, or HZSM-5 following impregnation with an aqueous solution of H_2PtCl_6 , PdCl_2 , AgNO_3 , or HAuCl_4 .¹⁷³ Directly after impregnation, Ar glow discharge plasma was performed to produce the reduced materials. The treatment led to Pd, Pt, and Ag particles of 2, 4, and 6 nm size, respectively, a factor of 2–3 smaller compared to those of samples reduced in H_2 at 300 °C. A systematic study on 2 wt % Pt/ TiO_2 revealed it took 60 min to fully reduce the sample, and even O_2 usage led to a net reducing plasma, although some oxides were also formed. Ar glow discharge plasma has also been used to produce 3.5 wt % Pd/ $\gamma\text{-Al}_2\text{O}_3$ after impregnation and drying at 110 °C.¹⁷⁴ Compared to a regular calcination and reduction treatment at 500 °C, a factor of 2 smaller particles were obtained (3.2 vs 7.5 nm). One weight percent Ir/ $\gamma\text{-Al}_2\text{O}_3$ was prepared after impregnation with H_2IrCl_6 followed by Ar glow discharge plasma.¹⁷⁵ Even after annealing at 600 °C in Ar, only 1 nm particles were found, while conventional reduction in H_2 resulted in 3 nm particles. AuPd bimetallic particles on SBA-15 have also been prepared using this method by incipient wetness impregnation of HAuCl_4 and $\text{Pd}(\text{NO}_3)_2$ at a total metal loading of 4 wt %.¹⁷⁶ After impregnation, Ar glow discharge plasma was used to decompose the precursors. The resulting material exhibited nanoparticles with Pd-rich shells and Au cores, whereas conventionally prepared samples contained homogeneous PdAu alloy particles, showing the potential for producing tailored bimetallics.

Succession of N_2 and H_2 plasmas has also been used after impregnation and drying. Unpromoted and Pt-promoted 15 wt % $\text{Co}/\gamma\text{-Al}_2\text{O}_3$ catalysts were prepared by impregnation and drying at 100 °C.¹⁷⁷ Even though a H_2 plasma was used, X-ray absorption near-edge structure (XANES) and extended X-ray absorption fine structure (EXAFS) data showed that the cobalt nitrate decomposed not into metallic Co but rather into Co_3O_4 , suggesting the type of gas only plays a minor role; however, no crystallinity was detected by XRD. Upon subsequent thermal reduction, 6–7 nm Co particles were obtained related to improved reducibility of the plasma-treated sample as compared to a conventionally calcined sample that led to 10 nm particles. Unpromoted and Ru-promoted 10 wt % Co/SiO_2 catalysts have also been prepared via this method after impregnation and drying at 90 °C.¹⁷⁸ It was found that the

resulting Co_3O_4 particles depended on the power used during glow discharge. At 60 V, 8.5 nm particles formed, with good reducibility and performance in the Fischer–Tropsch reaction. Particles as small as 5.7 nm were found after treatment at 120 V; however, this was accompanied by formation of cobalt silicate, which led to catalysts with lower activity. It was proposed that the plasma promotes crystal nucleation, so that a relatively high nucleation to growth ratio can be achieved, resulting in relatively small particles. Slightly smaller nickel particles have also been reported in 8 wt % Ni/MgO– Al_2O_3 materials after impregnation and drying at 110 °C.¹⁷⁹

Glow discharge plasma has also been used as an additional pretreatment step to improve catalysts. Five weight percent Ni/ $\gamma\text{-Al}_2\text{O}_3$ has been prepared by impregnation and drying at 110 °C, followed by decomposition in Ar plasma and a subsequent thermal calcination step.¹⁸⁰ An improved stability was found during the dry reforming of methane, which was attributed to a stronger metal–support interaction induced by the plasma treatment. A similar improved interaction was also suggested for the production of up to 2 wt % Pt/TiO₂ by including an Ar glow discharge plasma step between drying and thermal calcination.¹⁸¹ In the above-mentioned studies, the plasma treatment lasted between 1 and 2 h. This is shorter than most conventional thermal activation procedures and a potential benefit of cold plasma techniques. However, to our knowledge, no studies have been performed on the minimum duration of the plasma treatment needed for completeness and of the decomposition or the penetration power of the treatment for applications in larger catalyst bodies or pellets.

Other cold plasma techniques have been investigated. Dielectric barrier discharge (DBD) plasma under atmospheric conditions was used in the synthesis of 20 wt % Co/SiO₂ after incipient wetness impregnation and drying at 100 °C.¹⁸² However, the resulting catalyst exhibited similar activity in the Fischer–Tropsch synthesis compared to conventionally calcined catalysts, and TEM images showed 50 nm aggregates were formed in the DBD method, so more research is needed to make this a viable alternative. Microwave plasma has been used for the preparation of 5 or 10 wt % Ni/CeO₂ by wet impregnation and drying at 100 °C.¹⁸³ Catalysts prepared with a power of 250 W exhibited a dispersion similar to that of samples conventionally prepared by calcination. The samples formed by microwave plasma exhibited a greatly increased stability, which was again attributed to enhanced metal–support interactions. However, during the microwave treatment, a large decrease in support surface area and a large increase in pore diameter were observed, which did not occur during conventional thermal calcination. This was attributed to removal of residual carbon that remained after synthesis of the CeO₂ support. However, this may significantly influence the formed phase.

5. EMERGING TECHNIQUES

5.1. Melt Infiltration

In melt infiltration, a metal or metal precursor salt is physically mixed with the support structure, and subsequently heated above the melting temperature of the metal (salt). This results in the melt being sucked into the pores of the support by capillary forces, whereby an important condition is that the melt and decomposition temperatures should be sufficiently different. As such, this preparation method exhibits many similarities to impregnation and drying (section 4), and similar

physical principles of support wetting and capillary pressure and flow are important.¹⁸⁴ In specific cases melt infiltration can provide an attractive alternative due to the relatively simple procedure and no need for solvent. Besides melt infiltration, the method is known by other names such as the solid–solid method, solid-state impregnation, and the solvent-free method.

Melt infiltration for the synthesis of catalysts has been mostly performed with transition-metal nitrate hydrates. These exhibit low melting points since melting occurs as dissolution in their own crystal water, generally between 50 and 100 °C (Table 2),

Table 2. Example of Melting Temperatures of Several Metal Precursors¹⁸⁵

precursor	T_{melt}^a (°C)	precursor	T_{melt}^a (°C)
$\text{Co}(\text{NO}_3)_2 \cdot 6\text{H}_2\text{O}$	55	$\text{Fe}(\text{NO}_3)_3 \cdot 9\text{H}_2\text{O}$	47
$\text{Ni}(\text{NO}_3)_2 \cdot 6\text{H}_2\text{O}$	56	$\text{Ag}(\text{NO}_3)$	210
$\text{Cu}(\text{NO}_3)_2 \cdot 3\text{H}_2\text{O}$	114	$\text{Fe}(\text{acac})_2$	190
$\text{Cr}(\text{NO}_3)_3 \cdot 9\text{H}_2\text{O}$	66	$(\text{NH}_4)_2\text{Cr}_2\text{O}_7$	n/a ^b

^aIt is noted that many metal nitrates start to lose part of the crystal water at temperatures slightly above the melting temperature.

^bDecomposes before melting.

while use of metal precursors without crystal water is generally less successful. For example, physical mixing of MCM-41 and $\text{Ni}(\text{NO}_3)_2 \cdot 6\text{H}_2\text{O}$ followed by heating to 500 °C caused infiltration of the nickel nitrate into the pores of the support, resulting in small NiO particles.⁸² However, when nickel acetate and MCM-41 were physically mixed, no infiltration was observed during thermal treatment, and all of the acetate remained outside the pores. Care has to be taken to prevent decomposition of the precursor prior to entrance into the pores. Physical mixing of a hydrated $\text{Fe}(\text{NO}_3)_3$ salt (hydration not specified) and MCM-41, followed by heating to 400 °C at 5 °C/min and further heating to 700 °C, resulted in sharp XRD patterns related to crystallites over 40 nm in size present on the external surface of the MCM-41 primary particles.¹⁸⁶ It is likely that the high-temperature ramp applied caused decomposition of the iron nitrate before it completely filled the mesopores of the support. However, many small particles were also observed, indicating melt infiltration was partly successful. One millimole of $\text{Co}(\text{NO}_3)_2 \cdot 6\text{H}_2\text{O}$, $\text{Ni}(\text{NO}_3)_2 \cdot 6\text{H}_2\text{O}$, $\text{Ce}(\text{NO}_3)_3 \cdot 6\text{H}_2\text{O}$, or $\text{Cr}(\text{NO}_3)_3 \cdot 9\text{H}_2\text{O}$ physically mixed with 0.15 g of SBA-15 or KIT-6 and heated to 500 °C at a rate of 1 °C/min resulted in large interconnected networks inside the pores of the support, which formed porous single-crystal networks after removal of the silica.¹⁸⁷ A similar procedure attempted with $\text{Pb}(\text{NO}_3)_2$ and $(\text{NH}_4)_2\text{Cr}_2\text{O}_7$ revealed these precursors did not infiltrate the silica supports, which was explained by decomposition of the precursor without melting. Physical mixing of $\text{Ce}(\text{NO}_3)_3 \cdot 6\text{H}_2\text{O}$, $\text{Ni}(\text{NO}_3)_2 \cdot 6\text{H}_2\text{O}$, or $\text{Co}(\text{NO}_3)_2 \cdot 6\text{H}_2\text{O}$ with SBA-15 at lower loadings (0.3 mmol for 0.1 g) followed by calcination to 450 °C did not result in large interconnected networks but rather in small 4–7 nm particles.¹⁸⁸ This suggests the loading may be relevant for the formation of large crystals, or that there was a significant difference between the interconnectivity of the used SBA-15 supports.

In the previous studies, infiltration and decomposition of the metal nitrate hydrate precursors was performed in a single step. However, when decomposition starts while infiltration is still ongoing, it is possible that material decomposes on the external surface of the support, or that the formed metal oxide nuclei are continuously supplied with additional metal nitrate hydrate,

causing the grow of large crystals forming a network throughout the pores of the support. As this is undesirable for catalysis, the infiltration and decomposition step should ideally be separated. In a detailed study, three different SBA-15's, MCM-41, and a silica gel were melt infiltrated with $\text{Co}(\text{NO}_3)_2 \cdot 6\text{H}_2\text{O}$ by heating to 60°C in a sealed Teflon-lined autoclave for 24 h.¹⁸⁹ Afterward, XRD did not detect any crystalline material, suggesting all the $\text{Co}(\text{NO}_3)_2 \cdot 6\text{H}_2\text{O}$ was taken up by the pores of the support. In contrast, when the same procedure was performed in an open crucible, sharp $\text{Co}(\text{NO}_3)_2 \cdot 4\text{H}_2\text{O}$ peaks were observed indicative of partial decomposition of $\text{Co}(\text{NO}_3)_2 \cdot 6\text{H}_2\text{O}$, which then remained on the external surface of the support. After calcination in a flow of N_2 , large Co_3O_4 particles were found on the external surface when an open crucible was used for infiltration, while no such particles were observed after melt infiltration in a closed autoclave. Making use of the difference in melting point between intraporous ($5\text{--}20^\circ\text{C}$) and extraporous (53°C) $\text{Co}(\text{NO}_3)_2 \cdot 6\text{H}_2\text{O}$, the maximum loading was studied by DSC.¹⁸⁹ Up to a loading of $1.4 \text{ g}_{\text{Co}(\text{NO}_3)_2 \cdot 6\text{H}_2\text{O}}/\text{g}_{\text{SBA-15}}$, only intraporous $\text{Co}(\text{NO}_3)_2 \cdot 6\text{H}_2\text{O}$ was observed, whereas, above this, both extraporous and intraporous $\text{Co}(\text{NO}_3)_2 \cdot 6\text{H}_2\text{O}$ was found (Figure 19). This amount corresponded to a pore filling

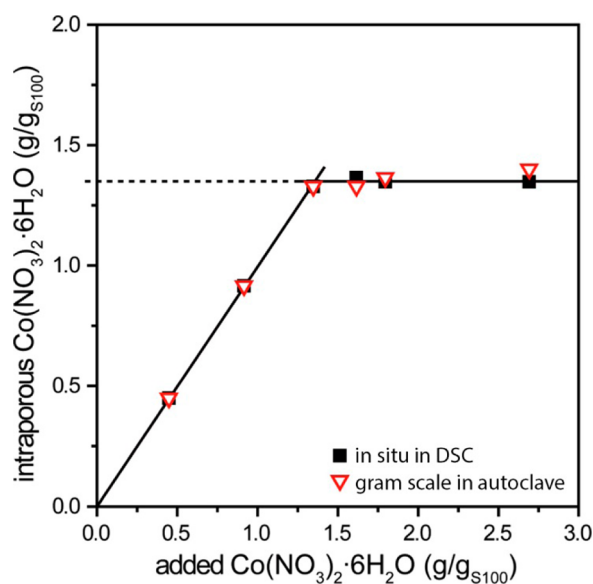


Figure 19. Amount of intraporous $\text{Co}(\text{NO}_3)_2 \cdot 6\text{H}_2\text{O}$ per gram of SBA-15 as a function of the amount added in the physical mixture. Squares indicate preparation in situ in DSC measurement cups, while triangles indicate preparation ex situ in a closed autoclave at 60°C . Up to 1.4 g of added $\text{Co}(\text{NO}_3)_2 \cdot 6\text{H}_2\text{O}$ was all found inside the pores after melt infiltration, whereas further addition did not increase the intraporous loading. Adapted from ref 189. Copyright 2010 American Chemical Society.

of 75% assuming the density of crystalline $\text{Co}(\text{NO}_3)_2 \cdot 6\text{H}_2\text{O}$. However, due to the lack of an XRD signal, it was proposed that the $\text{Co}(\text{NO}_3)_2 \cdot 6\text{H}_2\text{O}$ was not crystalline but rather an amorphous phase with a lower density, so that a close to 100% filling was more likely. This methodology of melt infiltration in an autoclave was subsequently utilized to produce a variety of highly loaded Co/SiO_2 (20 wt %) and Ni/SiO_2 (21 wt %) catalysts by using calcination in N_2 or 1% NO/N_2 gas flows,^{24,142} and a similar method was used to form a bimetallic Co/Rh catalyst on $\gamma\text{-Al}_2\text{O}_3$ (20 and 1 wt %, respectively).¹⁵¹

Also $\text{Cu}\text{--}\text{Ce}$ bimetallic materials have been synthesized using melt infiltration. $\text{Cu}(\text{NO}_3)_2 \cdot 2.5\text{H}_2\text{O}$ and $\text{Ce}(\text{NO}_3)_3 \cdot 6\text{H}_2\text{O}$ were first mixed at 120°C in a closed vial, after which silica hollow spheres were added for infiltration followed by calcination at 550°C .¹⁹⁰ The molar ratio between the copper and ceria nitrates was varied, while in each case the total salt volume was kept below the pore volume of the support. However, when Cu/Ce ratios higher than 1 were used, large $\text{Cu}(\text{NO}_3)_2 \cdot 2.5\text{H}_2\text{O}$ crystals were detected after infiltration, suggesting extraporous $\text{Cu}(\text{NO}_3)_2 \cdot 2.5\text{H}_2\text{O}$ was still present. This was also observed after calcination, where large 100 nm CuO crystallites were detected. When the ratios were reversed, no extraporous salt was found. Another similar study successfully prepared $\text{Cu}\text{--}\text{Ce}/\text{SBA-15}$ using melt infiltration, which exhibited better mixing between copper and ceria compared to that with wet impregnation.¹⁹¹

Besides metal nitrates, acetylacetonate (acac) precursors have also been used for melt infiltration. $\text{Mo}(\text{acac})_3$ and $\text{Fe}(\text{acac})_3$ were used to prepare $\text{Fe}/\text{KIT-6}$, $\text{Mo}/\text{KIT-6}$, and $\text{Mo}\text{--}\text{Fe}/\text{KIT-6}$ at loadings between 0.3 and 1.5 wt % by physically mixing the salt and support and heating to 500°C for 5 h.¹⁹² However, this may have caused a large amount of pores to be blocked, as a reduction in BET surface area from 600 to $60 \text{ m}^2/\text{g}$ was observed accompanied by a reduction in pore volume from 0.8 to 0.15 mL/g , suggesting the melting point and decomposition temperature of these precursors are too close to each other for an efficient melt infiltration procedure. $\text{Pt}(\text{acac})_2$ has also been introduced into an Al-SBA-15 material by physical mixing, followed by a thermal treatment at 100°C for 24 h, 180°C for 0.5 h ($5^\circ\text{C}/\text{min}$), and 400°C for 6 h ($10^\circ\text{C}/\text{min}$).¹⁹³ A homogeneous distribution of the 1 wt % Pt was obtained, with small 1 nm particles similar to those in the preparation by wet impregnation. However, 180°C is close to the boiling point of $\text{Pt}(\text{acac})_2$, so that this form of solid-state impregnation concerns vapor deposition rather than melt infiltration.

Due to the absence of solvent that needs to be removed and the increased viscosity of molten metal salts compared to aqueous solutions, melt infiltration can have an effect on the distribution of the active phase during the loading step. For example, although the surface tensions of a cobalt nitrate solution and molten $\text{Co}(\text{NO}_3)_2 \cdot 6\text{H}_2\text{O}$ at 60°C were found to be similar, the viscosity of the melt was over 10 times higher.¹⁹⁴ Melt infiltration of a 2.7 mm silica pellet by $(\text{NO}_3)_2 \cdot 6\text{H}_2\text{O}$ at 60°C for 30 s resulted in penetration of the outer 0.1–0.2 mm, whereas solution impregnation resulted in a homogeneous distribution. Similarly, melt infiltration of $\text{Ni}(\text{NO}_3)_2 \cdot 6\text{H}_2\text{O}$ into a 3 mm alumina pellet for 2–5 min, followed by cooling to room temperature, resulted in distinct eggshells as determined by micro X-ray fluorescence (micro-XRF), while infiltration over 10 or 30 min, or an aging step at 65°C , resulted in more homogeneous distributions.¹⁹⁵ Some inhomogeneities did remain, attributed to the precipitation of nickel tetrahydrate on the alumina, which has a higher melting point.

The absence of additional solvent can limit redistribution during subsequent thermal steps if enough time is allowed for a homogeneous distribution during melt infiltration. As described in section 4.3.3, freeze-drying of a 4 M aqueous solution of cobalt nitrate inside the pores of the silica gel required temperatures below -90°C to freeze.¹⁴² At -45°C , the material was not completely frozen and extensive redistribution was observed in the form of eggshell catalysts and large aggregates. However, when $\text{Co}(\text{NO}_3)_2 \cdot 6\text{H}_2\text{O}$ was melt infiltrated, a freezing temperature of only -20°C was required

to solidify the confined precursor. Thus, when freeze-drying was performed at $-45\text{ }^{\circ}\text{C}$, a homogeneous distribution was obtained after melt infiltration (Figure 20). A more

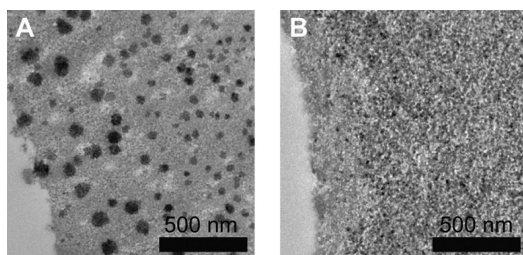


Figure 20. TEM images of $\text{Co}_3\text{O}_4/\text{SiO}_2$ prepared via incipient wetness impregnation (A) and melt infiltration (B) followed by freeze-drying at $-45\text{ }^{\circ}\text{C}$ and calcination in N_2 flow at $350\text{ }^{\circ}\text{C}$. The impregnated sample was not fully solidified, resulting in severe aggregation and redistribution of the metal nitrate toward the external surface of the silica grain, whereas the melt-infiltrated sample exhibited a homogeneous distribution due to the fully frozen precursor. Adapted with permission from ref 142. Copyright 2013 Elsevier.

homogeneous distribution was also obtained after drying of Co/SiO_2 with large pores in a N_2 flow at $150\text{ }^{\circ}\text{C}$, which resulted in eggshell catalysts after incipient wetness impregnation but in homogeneous distributions after melt infiltration.¹³⁸

5.2. Colloidal Synthesis

Colloidal synthesis provides unique opportunities to control the size, shape, and composition of nanoparticles in the liquid phase and has been reviewed previously.^{196,197} The nanoparticles are generally formed by stepwise induction of a change in conditions in an otherwise homogeneous solution of the metal precursor. This results in a nucleation burst, followed by growth of the nanoparticles from the remaining precursor in solution. Ligands present in the solution play an essential role in stabilizing the nanoparticles against aggregation, coalescence, and growth, while they may also influence the shape of the nanoparticles.¹⁹⁸ Even though the synthesis of colloidal nanoparticles has been studied extensively also for catalysis¹⁹⁹ (see also reviews on electrocatalysis,²⁰⁰ the oxygen reduction reaction,²⁰¹ or size and shape selectivity²⁰²), few studies focus on deposition of the preformed particles on a support, even though this step is crucial for obtaining active and stable heterogeneous catalysts. Moreover, different colloidal synthesis methods and the variety of stabilizing ligands that have to be removed before or after deposition make generalization of the available literature difficult. Here we do not repeat earlier reviews on nanoparticle synthesis but rather focus on recent studies that address the challenge of deposition of nanoparticles on a support.

Wet impregnation is commonly applied to deposit the colloids onto a support due to the relatively low nanoparticle concentrations in colloidal solutions necessary to prevent aggregation and precipitation. It can take a long time for all particles to migrate into the pores of the support because diffusivity of colloidal nanoparticles is relatively slow, which can be stimulated through use of sonication. The drying step can have a large influence on the distribution of the nanoparticles when particles are not strongly bound to the support, as has been demonstrated for the drying of colloidal wet films.¹⁴⁰ Significant redistribution toward the external surface of the grains is possible since evaporation of the solvent in porous bodies usually occurs on the external surface (see section 4.3).

Even so, few studies report the distribution of nanoparticles at the nanoscale and even less the macroscopic distribution across support grains. Co nanoparticles deposited on SBA-15 by wet impregnation followed by extensive washing resulted in aggregation of particles in some areas, while other areas of the support remained empty.²⁰³ Similarly, iron oxide particles of 2–10 nm size deposited by wet impregnation on $\gamma\text{-Al}_2\text{O}_3$ showed similarly inhomogeneous distributions with particles aggregated and preferentially deposited on the external surface of the support.²⁰⁴ The same particles deposited on MCM-41 with a pore size of 3 nm exhibited homogeneous distributions, but were exclusively deposited on the external surface, not surprising considering the relatively small pore size in relation to the size of the nanoparticles. However, eggshell catalysts have also been observed on carbon model supports with pore sizes larger than the colloidal particles. Focused ion beam scanning electron microscopy (FIB-SEM) on a model carbon support with pore sizes between 75 and 250 nm impregnated with 15–30 nm Pd particles revealed almost exclusively eggshell distributions.²⁰⁵ Penetration of the pores was possible when a vacuum impregnation was performed; however, the resulting metal distribution remained inhomogeneous.

Deposition of nanoparticles often relies on electrostatic interactions, van der Waals interactions, or polar bonds involving the stabilizing ligands of the particles on one hand, and the support surface groups on the other hand. Electrostatic interactions have been shown to play an important role in 4 nm Pd colloids stabilized with poly(vinylpyrrolidone) (PVP).²⁰⁶ These were found to be negatively charged between pH 2 and pH 8. When deposited by a wet impregnation at pH 3 on differently treated CNFs with PZCs ranging from 2.2 to 7.7, a maximum uptake (3.9 wt %) occurred for CNFs with high PZCs, whereas supports with a PZC around 2–3 exhibited almost no uptake (0.5 wt %). Thus, the supports with a low PZC and concomitant high surface oxygen content that were negatively charged at pH 3 repelled the negatively charged colloids, whereas the high PZC carbon supports with low oxygen content attracted the colloids. The uptake of PtO_2 colloidal particles prepared by the polyol method and stabilized by glycolate exhibited a similar dependency on the carbon support.^{207,208} Uptake of PtO_2 nanoparticles varied greatly from 1.5 to 19 wt %. However, since deposition of the oxidic particles was performed at pH 9–10, electrostatic interaction was unlikely. It was proposed that the particles adsorbed preferentially on carbene-type or surface defect sites. Moreover, similar to the Pd metal particles, uptake was improved by removing oxygen groups from the support, which were thought to weaken the adsorption strength.

Kimura et al. found the adsorption capacity of TiO_2 for Pt colloids stabilized with PVP to be very high, good for Al_2O_3 and MgO , and poor on SiO_2 .²⁰⁹ However, adsorption on TiO_2 was not dependent on the pH of the solution between pH 2 and pH 10, suggesting nonspecific interactions (van der Waals or polar) played an important role. At high loadings (10 wt %), an increase in particle size was observed, suggesting the support did not directly bind with all particles at these high loadings, leading to aggregation. Similar results have been reported for other Pd and Pt particles, which started to form aggregates at higher loadings.²¹⁰ Moreover, extra addition of the used stabilizing agent hexadecyl(2-hydroxyethyl)-dimethylammonium dihydrogen phosphate reduced the uptake of the metal nanoparticles likely due to competitive adsorption,

suggesting the adsorption of ligands was competing with the surface deposition of nanoparticles.

Immobilization of Au_{11}^{3+} particles with 0.8 nm diameter stabilized with triphenylphosphine (TPP) has been found to depend on the solvent.²¹¹ The highest uptake on silica was observed when pure dichloromethane (DCM) was used, whereas a gradual decrease in uptake occurred upon mixing with ethanol. It was proposed that the binding with the TPP ligands occurred via weak interactive forces between the permanent dipole of the silica OH surface groups and the induced dipole within the ligand layer. At increasing ethanol concentration, the attractive force between the two became weaker due to the increased electrical permittivity caused by ethanol. However, although uptake was less when a DCM/ethanol mixture was used, smaller particle sizes were also obtained, which was attributed to a more homogeneous distribution due to the weaker interaction in the presence of ethanol. The stability of Au particles also depends on the stabilizing ligand. When the electrostatic stabilizer tetrakis-(hydroxypropyl)phosphonium chloride (THPC) was used, smaller particles were deposited on a carbon support compared to those deposited when poly(vinyl alcohol) (PVA), a steric stabilizer, was used.²¹² However, when Pd was subsequently added from a Na_2PdCl_4 solution in the presence of PVA and H_2 , THPC-stabilized particles exhibited more extensive growth compared to the PVA-stabilized particles.

The charge of the stabilizing agent also plays a large role. For the deposition of 10 nm Ag particles stabilized with 3-mercaptopropionic acid (MPA) onto $\gamma\text{-Al}_2\text{O}_3$, the pH of the impregnating solution influenced the final particle size.²¹³ At pH 3.7, MPA was negatively charged, causing repulsion between nanoparticles, whereas attraction with the positively charged support caused direct deposition of the nanoparticles. However, at a pH of 2.9, MPA was almost negligibly charged, causing particles to assemble together due to hydrogen bonding and resulting in average particles of 26 nm after calcination at 550 °C (Figure 21).

After deposition of the particles on the support, care has to be taken to remove the stabilizing and structure-directing ligands or surfactants. Thermal decomposition of the ligands is most common. However, depending on the ligand, this can require high temperatures at which sintering of the metal particles becomes significant. For example, for nickel particles

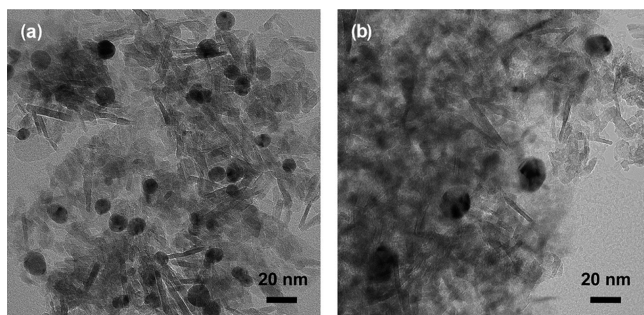


Figure 21. TEM images of Ag particles deposited on $\gamma\text{-Al}_2\text{O}_3$ at different pH values, followed by calcination at 550 °C and reduction at 200 °C: (a) pH 3.7, (b) pH 2.9. At pH 3.7 the originally 10 nm Ag colloids are unchanged after deposition due to the electrostatic repulsion of the MPA ligands, whereas at pH 2 severe sintering occurs due to the negligible charge of MPA at this pH. Adapted from ref 213. Copyright 2009 American Chemical Society.

capped with a mixture of oleic acid, trioctylamine, and trioctylphosphine deposited on SiO_2 , activation at 150 and 350 °C in H_2 was not sufficient to remove all the ligands.²¹⁴ Even at 500 °C not all ligands were removed, while at this temperature particles exhibited significant sintering, growing from 5.3 to 20 nm.

Alternatively, the ligands may be extracted using solvents after deposition. In this case, the particles should exhibit a high affinity for the support to prevent excessive redistribution, or a solvent other than the solvent during deposition may be used. This was first demonstrated on 3 nm gold colloids capped with PVA after aqueous deposition on TiO_2 .²¹⁵ A conventional thermal treatment was compared to aqueous solvent extraction. Refluxing in water at 90 °C for 60 min resulted in removal of 20% PVA, and no gold was found in the washing solution, while the particle size showed a minor increase from 3.0 to 4.8 nm. After a calcination treatment at 300 °C, all PVA was removed; however, the particle size increased to 6.1 nm. Further removal of ligands using the washing treatment was difficult; nonetheless, the washed material was 5 times more active in the CO oxidation reaction. Although this cannot be explained solely from the particle size difference between the two methods, it shows washing may be beneficial compared to thermal treatment even if not all ligands can be removed. Copper particles capped with cetyltrimethylammonium bromide (CTAB) were successively deposited on a γ -alumina via a similar method.²¹⁶ The 4.6 nm copper particles were impregnated using an aqueous solution, followed by washing with ethanol to remove the CTAB. After subsequent activation at 300 °C in H_2 , only a minor increase in particle size to 5.2 nm was observed. However, the ligand removal was not quantified, nor was potential loss of copper during washing commented on. Unfortunately, the removal of ligands after deposition of the colloidal metal nanoparticles is rarely studied in detail, even though it is crucial to obtain active catalysts and deserves more attention.

Microemulsions provide a different way to produce finely dispersed colloidal nanoparticles, whereby nanoparticles are synthesized in the aqueous cores of the surfactant reverse micelles. Deposition of these nanoparticles can often be done by destabilizing the microemulsion in the presence of a support by addition of, for example, THF. However, the resulting supported metal dispersion can suffer compared to that of the nanoparticles in solution. Moreover, synthesis of reverse micelle Co_3O_4 particles directly in contact with a $\gamma\text{-Al}_2\text{O}_3$ support resulted in large amounts of cobalt aluminate, which gave rise to cumbersome catalyst activation.²¹⁷ A study on neutral (sodium bis(2-ethylhexyl) sulfosuccinate, AOT) or ionic (poly(oxyethylene) (8) octylphenyl ether, TT) surfactants for the production of Co_3O_4 particles showed the particle size was only slightly influenced by the surfactant.²¹⁸ However, a great improvement in dispersion was observed when the silica support was first silylated. This resulted in a decrease in Co particle size from 16 to 6.5 nm (TT) or from 15 to 5 nm (AOT) after reduction. It was concluded that the increased interaction between the hydrophobic silylated support and the micelles reduced the degree of aggregation in the liquid medium, thereby improving the dispersion and possibly the distribution.

Although investigation on the kinetics of particle formation is difficult and rarely attempted, Finke et al. elucidated the kinetics of Pt nanoparticle formation from a H_2PtCl_6 solution in the presence of $\gamma\text{-Al}_2\text{O}_3$ for the synthesis of 1 wt % Pt/

Al_2O_3 .²¹⁹ By using the hydrogenation activity of Pt, the nanoparticle formation was inferred from the simultaneous hydrogenation reaction of cyclohexene with hydrogen. Through use of a high-precision pressure transducer, real-time information on the loss in H_2 pressure provided unique kinetic data on the nanoparticle formation, assuming the reaction was structure insensitive. H_2PtCl_6 was first impregnated using ethyl acetate as the solvent, dried at room temperature in vacuum, and subsequently added to a solution of cyclohexene in ethanol. By applying a H_2 pressure at 22 °C, the Pt precursor was reduced to Pt(0), forming supported nanoparticles which immediately started to convert cyclohexene to cyclohexane. The rate-determining step was assumed to be formation of the growing nanoparticle, so that the catalyzed reaction was used as a probe for the rate of formation. Further study suggested a sigmoidal growth behavior that fit a two-step mechanism for nanoparticle formation of slow nucleation and autocatalytic surface growth first discovered for nanoparticle formation in solution.²²⁰ Because of the good fit to the two-step mechanism, it was proposed that many of the insights obtained for nucleation and growth in solution also hold in the presence of a support.

A more detailed study was subsequently performed for the synthesis of 1 wt % Ir/ $\gamma\text{-Al}_2\text{O}_3$ catalysts.²²¹ Similarly, $[\text{Ir}(\text{1,5-COD})\text{Cl}]_2$ was first deposited on γ -alumina using ethyl acetate and dried, followed by formation of the Ir nanoparticles in acetone at 22 °C under hydrogen pressure, which was monitored by the hydrogenation reaction of cyclohexene. Again, the system showed an excellent fit to the two-step mechanism of nucleation followed by autocatalytic surface growth, producing 3 nm iridium particles with a relatively narrow particle size distribution. Further investigation showed nucleation occurred bimolecularly from the precursor in solution, followed by rapid capture of the nuclei by the $\gamma\text{-Al}_2\text{O}_3$ surface and further autocatalytic growth of the supported particles.^{222,223} However, when a 5-fold decrease of the Ir(1,5-COD)Cl/ $\gamma\text{-Al}_2\text{O}_3$ precatalyst was used, a different growth behavior was observed, resulting in iridium particles of 1.7 nm with a relatively broad particle size distribution.²²⁴ This led to the proposal of a four-step mechanism (Figure 22), whereby Ir(0) nuclei are first formed, which subsequently grow autocatalytically from additional precursor in solution to form larger $\text{Ir}(0)_n$ clusters, but can also aggregate. These larger aggregated clusters can again grow autocatalytically from the precursor in solution, but will likely not aggregate with other nuclei due to their limited mobility when they are deposited on the support surface. The new model showed an excellent fit with experimental data; however, whether the individual steps occur in solution or on the support surface was not reported, and the reason for the change from a two-step to a four-step mechanism at lower concentration is subject to further research.

Finally, it is noted that in recent years colloidal techniques have been used for synthesizing a porous support shell around preformed nanoparticles. While these are relevant for catalysis and catalyst preparation, their discussion is beyond the scope of the present review, and they have recently been reviewed elsewhere.^{225–227}

5.3. Atomic Layer Deposition

Atomic layer deposition (ALD) has shown increased use for the preparation of catalysts.²²⁸ ALD, also known as atomic layer epitaxy (ALE) or molecular layering, is based on the irreversible

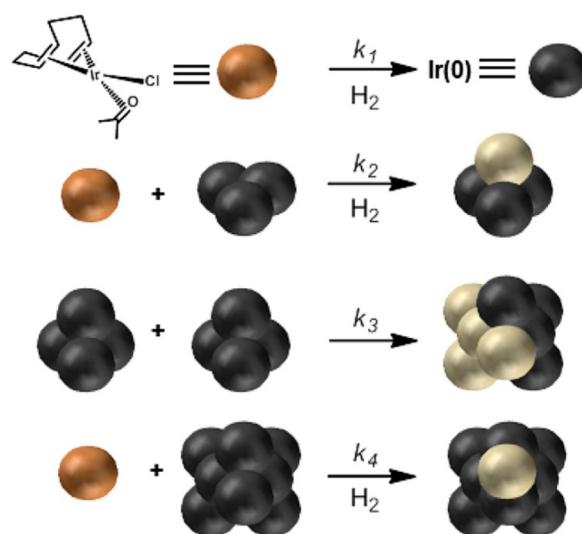


Figure 22. Schematic representation of the four-step mechanism for nanoparticle formation and agglomeration. Ir(1,5-COD)Cl is first reduced to Ir(0) nuclei, which subsequently grow autocatalytically by addition of more Ir(1,5-COD)Cl to form $\text{Ir}(0)_n$. Two such $\text{Ir}(0)_n$ clusters can aggregate to form one larger cluster, while further growth of such large clusters is limited to autocatalytic growth via addition of Ir(1,5-COD)Cl. Adapted from ref 224. Copyright 2014 American Chemical Society.

and self-limiting reaction between molecules in the gas phase and a surface, so that a uniform monolayer is formed. In general, it entails reaction of a vapor-phase metal precursor with support surface groups such as terminal hydroxyls, followed by purging and a second reaction, often with oxygen or hydrides of the nonmetal elements such as water, ammonia, or hydrogen sulfide, for the formation of metals and metal oxides, nitrides, or sulfides. This second reaction also regenerates surface sites, often in the form of hydroxyl groups, so that multiple ALD cycles can be performed successively to deposit more material in a layer by layer fashion to produce increasingly thick films.²²⁹ The technique principally deposits sequential (mono)layers of material; however, transition metals and especially noble metals tend to agglomerate to form small particles even after one cycle due to the stable metal–metal bonds.

Early detailed studies on atomic layer deposition for catalyst preparation mainly concerned 2,2,6,6-tetramethyl-3,5-heptanedionato (thd) ligands for precursors such as $\text{Cu}(\text{thd})_2$,²³⁰ $\text{Pd}(\text{thd})_2$,^{230,231} and $\text{Rh}(\text{thd})_2$,²³¹ while acac precursors such as $\text{Ni}(\text{acac})_2$,²³² $\text{Co}(\text{acac})_2$,²³³ $\text{Co}(\text{acac})_3$,^{233,234} $\text{Cr}(\text{acac})_3$,²³⁵ and $\text{VO}(\text{acac})_2$ ²³⁶ were also used. Selective adsorption on SiO_2 and Al_2O_3 surfaces occurred via an exchange reaction between surface OH groups and ligands, although recently steric hindrance was found to play a role in the deposition of $\text{Co}(\text{acac})_2$ and $\text{Co}(\text{acac})_3$.²³⁷ The remaining acac or thd ligands were decomposed in oxygen, hydrogen, or water vapor. Multiple cycles were mainly used for Co and Ni, which exhibited a linear increase in metal loading along with an increase in particle size for one to ten cycles. Multiple cycles of $\text{VO}(\text{OC}_3\text{H}_9)_3$ on silica were less successful, because the V-catalyzed decomposition of the $\text{VO}(\text{OC}_3\text{H}_9)_3$ precursor complex caused uncontrolled deposition in later cycles.²³⁸

ALD can be an efficient deposition method for the production of finely dispersed metal particles for catalysis due to the self-limiting deposition reaction, allowing for a homogeneous distribution even in highly porous and

heterogeneous support bodies, which would not be possible with other, non-self-limiting methods. However, the actual penetration depth of the gas is highly dependent on the support material and partial pressure of the precursor. For example, on a very low density silica aerogel, ZnO was deposited from $\text{Zn}(\text{C}_2\text{H}_5)_2$ homogeneously penetrating hundreds of micrometers,²³⁹ while a copper layer formed by $[\text{Cu}(\text{S}^{\text{Bu-Me-amd}})]_2$ penetrated only up to 10 μm due to the 2 orders of magnitude lower partial pressure of the Cu precursor.²⁴⁰ Similar results were also obtained for deposition of Pt on carbon aerogel from (methylcyclopentadienyl)trimethylplatinum (MeCpPtMe_3).²⁴¹ It was postulated that, next to diffusion, adsorption–desorption equilibrium of the precursor and reaction product molecules also plays an important role depending on the support.

Feng et al. used silica with a grain size between 75–200 μm as a support for deposition of Pd.²⁴² Prior to Pd deposition, the silica was first coated by a 0.5 nm thick layer of Al_2O_3 using trimethylaluminum (TMA), or ZnO using diethyl zinc at 200 $^\circ\text{C}$, while water was used to decompose the precursors. Subsequently, 1.5–2.5 wt % Pd was deposited by one or two cycles of palladium hexafluoroacetylacetonate ($\text{Pd}(\text{hfac})_2$) and formalin (formaldehyde and methanol in water). On the basis of a time-dependent deposition study, it was concluded that diffusion of the precursor into the support was the limiting step for these materials and conditions. On the Al_2O_3 -coated silica, 1–2 nm Pd particles were found distributed uniformly across the support particles by scanning electron microscopy–energy-dispersive X-ray (SEM–EDX) spectroscopy, while no particles were detected on ZnO, suggesting an alloy formation. Using up to 25 cycles, it was found that the Pd particle size increased almost linearly from 1.1 to 2.9 nm on Al_2O_3 -coated silica.²⁴³ Moreover, an induction time was observed for the uptake of Pd, which increased after several cycles. It was postulated that when $\text{Pd}(\text{hfac})_2$ is deposited, $\text{Al}(\text{hfac})^*$ species are formed which are not removed during subsequent formalin exposure, and thus are poisoning the surface.²⁴⁴ The formalin treatment only removed hfac ligands on the Pd and replaced them with hydrogen adatoms, which formed new nucleation sites for further Pd cycles, resulting in an increased Pd uptake as particles became larger due to an increasing amount of nucleation sites for additional $\text{Pd}(\text{hfac})_2$. A similar growth behavior was observed on MgO and TiO_2 layers; however, no Pd particles were observed on pure silica, suggesting a limited reactivity of the Si–OH hydroxyl groups with $\text{Pd}(\text{hfac})_2$.²⁴³

A study of the deposition of Pt on $\gamma\text{-Al}_2\text{O}_3$, TiO_2 , and SrTiO_3 using MeCpPtMe_3 and H_2 or N_2 cycles showed the Pt precursor can be adsorbed on oxidic supports at temperatures as low as 100 $^\circ\text{C}$, and is decomposed at 200 $^\circ\text{C}$ in H_2 or 300 $^\circ\text{C}$ in N_2 to form metallic Pt particles.²⁴⁵ Even though a prolonged time was necessary for adsorption of MeCpPtMe_3 at 100 $^\circ\text{C}$, at 300 $^\circ\text{C}$ premature decomposition resulted in Pt deposition throughout the reactor. During decomposition of the precursor in H_2 or N_2 , mobile Pt species formed that aggregated into small clusters, forming Pt particles of 1–2 nm. The hydroxyl groups during these treatments were also regenerated, so that additional cycles may be performed. It was observed that the MeCpPtMe_3 precursor preferentially adsorbs on surface hydroxyl groups and not on metallic Pt, and that the Pt particle size did not increase much upon subsequent cycles. When O_2 was used to decompose the precursor, PtO formed, which interacted with MeCpPtMe_3 via reductive adsorption, resulting in an increase in Pt particle size. However, this only occurred when MeCpPtMe_3 already occupied most of the

surface hydroxyls, and was less noticeable for high surface area supports under the used conditions. Pt on silica gel (30–75 μm grain size) has also been prepared while keeping the substrate at 325 $^\circ\text{C}$.²⁴⁶ Even though the previous study mentioned 300 $^\circ\text{C}$ as an upper temperature, homogeneous distributions were reported on cross-sectioned silica particles. Three, five, or ten cycles of Pt precursor and O_2 were used to deposit 1.6, 2.3, or 12 wt % Pt, respectively, with particle sizes between 1 and 2.5 nm.

Mixed PtRu particles on Al_2O_3 were synthesized using alternating cycles of MeCpPtMe_3 and (2,4-dimethylpentadienyl)(ethylcyclopentadienyl)ruthenium ($\text{Ru}(\text{DER})$), decomposing the precursor with oxygen in between. Two cycles of $\text{Ru}(\text{DER})/\text{O}_2$ were followed by one cycle of $\text{MeCpPtMe}_3/\text{O}_2$ and one cycle of $\text{Ru}(\text{DER})/\text{O}_2$ for a final 1:1 molar ratio, and resulted in 1–2 nm particles with good mixing of Ru and Pt as determined by EXAFS analysis.²⁴⁷ PtPd bimetallic particles have also been synthesized using ALD on SiO_2 covered with Al_2O_3 or TiO_2 supports, creating 1–2 nm particles.²⁴⁸ However, as soon as a reduction treatment was performed, the particles rearranged to a Pt core/Pd shell nanostructure independent of the deposition sequence.

Although most studies have been performed on noble-metal nanoparticles, non-noble-metal particles can also be synthesized. Co_3O_4 was deposited on Al_2O_3 -coated and uncoated silica gel to 25 wt % using bis(cyclopentadienyl)cobalt and ozone.²⁴⁹ Using ALD, the particle size was reduced 2-fold compared to that obtained with incipient wetness impregnation, from 10–11 to 5–6 nm. However, IWI-prepared catalysts were more active for the Fischer–Tropsch reaction. This was attributed to retarded reduction of Co_3O_4 to Co for catalysts prepared by ALD, which was mitigated somewhat by Pt addition.

5.3.1. ALD for Nanoparticle Stabilization. Next to the active metal, a method has been developed in which an additional oxidic support layer was deposited by an extra step during ALD, referred to as ABC atomic layer deposition.²⁵⁰ The nature of Pd deposition from $\text{Pd}(\text{hfac})_2$ was especially suitable for this. In step A, $\text{Pd}(\text{hfac})_2$ was adsorbed on Al_2O_3 , whereby some hfac ligands dissociated and adsorbed on the alumina to prevent total coverage of Pd. Next, step B entailed ALD of TMA, which did not adsorb on the Pd precursor but did decompose the $\text{Al}(\text{hfac})^*$ species, and deposited a new layer of alumina on the support. In step C, the adsorbed TMA was decomposed by water, creating new surface sites for Pd adsorption in the next ABC cycle while keeping the existing adsorbed $\text{Pd}(\text{hfac})$ intact, so that further growth of these particles was not possible (note $\text{Pd}(\text{hfac})_2$ was decomposed by formalin, not water). This resulted in a very narrow size distribution of 1 nm particles for up to 15 cycles and 6.6 wt % Pd.²⁴³ However, this method is only possible if the precursor in step A does not adsorb on all sites, and reactants in step B and C do not react with the precursor from step A but do create new adsorption sites.

Deposition of a covering and stabilizing layer after synthesis of the supported metal particles has been completed is also possible. Feng et al. deposited Pd by ALD on an Al_2O_3 -covered silica gel, and subsequently coated this with additional Al_2O_3 by several ALD cycles using TMA and water at 200 $^\circ\text{C}$.²⁵¹ The resulting catalysts were tested in the decomposition of methanol, and showed significantly more active catalysts after 1–16 Al_2O_3 ALD cycles. This was attributed to more stable catalysts already after one cycle; whereas the uncoated catalyst

exhibited particle growth from 1.4 to 2.3 nm, the Al_2O_3 -coated catalysts did not exhibit any particle growth. When more than 16 cycles were used, the activity greatly decreased, attributed to coverage of the entire Pd particle by Al_2O_3 . It was found that initial Al_2O_3 cycles preferentially adsorbed on the Pd edge, step, and corner sites, whereas the catalytic activity comes from Pd(111), which was left unchanged. Further investigation showed that the Pd remained accessible because CH_3 species were adsorbed on Pd after the first ALD cycle, blocking it for further adsorption of TMA in the subsequent cycle, and therefore preventing formation of a monolayer (Figure 23).²⁵²

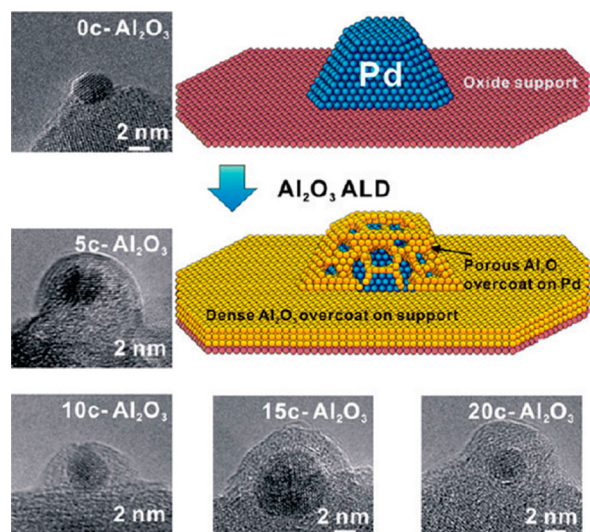


Figure 23. Schematic representation of the deposition of a porous alumina layer on Pd particles supported on an oxidic support, and TEM images of spherical alumina-supported Pd particles with different numbers of Al_2O_3 layers deposited on top, represented by the number of cycles (xc). An increasingly thick layer was observed with increasing cycles; however, the particles remained accessible for catalysis. Adapted from ref 252. Copyright 2012 American Chemical Society.

One study showed that, even after 45 ALD cycles with a resulting Al_2O_3 layer of 8 nm thickness, the Pd was still largely accessible and very resistant to coking and sintering in the dehydrogenation of ethane to ethylene at 650 °C.^{253,254}

The principle of blocking part of the nanoparticle by adsorption of a specific molecule so that a porous rather than solid layer is formed was further investigated on Pd deposited on θ - Al_2O_3 by ALD.²⁵⁵ After investigation of several blocking agents, octadecanethiol was chosen due to its relatively strong binding to the Pd particles and relatively large 2 nm length, while it does not react with TMA and therefore should remain on the surface of the Pd nanoparticles during ALD deposition of Al_2O_3 . CO adsorption after 21 cycles showed that Pd remained accessible when the blocking agent was used during ALD, whereas unprotected nanoparticles were completely covered in the sample prepared without octadecanethiol.

Coating of 1.7 nm Pt particles deposited by ALD on mesoporous silica has also been performed. A total of 10, 20, 30, or 40 cycles of TMA and ethylene glycol were performed for layers of 1, 2, 3, or 4 nm thickness, respectively.²⁵⁶ After 20 cycles, all Pt was found to be covered. However, an oxidation step at 400 °C in air created porosity in the Al_2O_3 layer. The resulting material had a Pt dispersion of 38%, significantly lower than that of the original material (65%) (Figure 24). However, when the materials were exposed to a temperature of 800 °C,

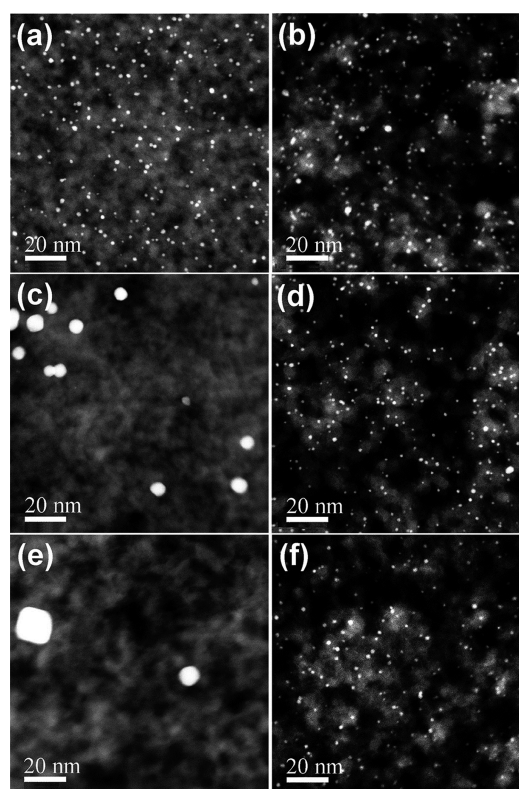


Figure 24. HAADF-STEM (high-angle annular dark field scanning transmission electron microscopy) images of Pt/silica catalysts after calcination for 4 h at 400 (a, b), 600 (c, d), and 800 (e, f) °C. The uncoated catalyst exhibited significant sintering, especially at higher temperatures (a, c, e), whereas the Al_2O_3 -coated catalyst prepared using 40 ALD cycles exhibited negligible particle growth (b, d, f). Adapted from ref 256. Copyright 2011 American Chemical Society.

the uncoated Pt catalyst exhibited significant sintering and a reduced dispersion of 4%, whereas the Pt sample coated with 20 cycles of Al_2O_3 exhibited much better stability and 27% dispersion. When 40 cycles were used, sintering was even almost nil.

It should be noted that ALD of a stabilizing layer can also be realized on existing materials which have not been created by ALD. For example, ALD was used to deposit an Al_2O_3 layer on a 3 nm Cu/ γ - Al_2O_3 catalyst prepared by incipient wetness impregnation of copper nitrate.²⁵⁷ After reduction, the catalyst exhibited 86 $\mu\text{mol/g}$ surface Cu sites. After deposition of an Al_2O_3 layer by 45 cycles of TMA and water, no Cu surface sites were found. However, a thermal treatment at 700 °C in air created porosity in the layer, resulting in 23 $\mu\text{mol/g}$ Cu surface sites. During the liquid-phase hydrogenation of furfural, this catalyst did not exhibit any particle growth, whereas the uncoated catalyst showed particle growth from 3 to 5 nm after catalysis. A similar improvement in nanoparticle stability was obtained for a Cu/ SiO_2 material coated by application of 30 cycles of TMA and water, followed by calcination at 700 °C in air.²⁵⁸ Prior to the alumina coating, the catalyst displayed 34 $\mu\text{mol/g}$ Cu surface sites. After coating, no sites were detected, whereas 15 $\mu\text{mol/g}$ surface sites were recovered after accessibility was recreated by calcination at 700 °C. To image the pores in the alumina overcoat, a layer of NbO_x was applied by 20 alternating ALD cycles of $\text{Nb}(\text{OCH}_2\text{CH}_3)_5$ and H_2O , which was previously shown to provide a uniform 1 nm thick niobia layer in the pores of SBA-15.²⁵⁹ Using STEM-EELS, the

penetration depth of NbO_x was found to be significantly larger after calcination of the overcoat at 700 °C, indicating the presence of pores before NbO_x deposition.²⁵⁸

Similar deposition of a protective layer by ALD on preformed material is playing an increasingly important role, for example, for the stabilization of photocathodes for the photoelectrochemical water reduction. In particular, Cu_2O is an attractive p-type oxide for photoelectrochemical hydrogen production; however, it is unstable in water. Recently, it was shown that protective Al-doped zinc oxide and titanium oxide layers deposited by ALD provided a stabilizing effect.²⁶⁰ Similarly, alumina ALD has been performed to coat LiCoO_2 for lithium ion battery electrodes, which also exhibited improved stability after extensive charge–discharge cycling compared to the untreated material.²⁶¹

6. CONCLUSION AND OUTLOOK

In this review, we have summarized the progress in conventional and new techniques for the synthesis of supported catalysts that has been obtained in recent years. Detailed studies of coprecipitation have provided new insights into the precipitation mechanism and effect of subsequent thermal activation treatments, while alternative precursors, precipitating agents, and thermal treatments provide promising alternatives for “greener” coprecipitation methods. Deposition precipitation is used to produce highly loaded metal catalysts, but shows an increased usage for the preparation of low-loaded, highly dispersed (noble)-metal catalysts. However, research has revealed that the physicochemical processes that take place at low loadings resemble adsorption rather than precipitation.

Impregnation and drying remains the most studied preparation technique. Detailed study of impregnated ordered materials has shown complete pore filling with aqueous solutions and oxidic supports, and an enhanced understanding of adsorption on support surfaces has improved the ability to rationally synthesize well-dispersed supported metal catalysts. The development of microspectroscopic tools enabled the study of (the development of) gradients and chemical speciation in macroscopic catalyst bodies during impregnation and drying processes, whereas models have been developed and experimentally verified that predict the distribution of the metal precursor across catalyst grains for both high and low precursor loadings. In addition, the development of the nanoscale metal distribution, which has been a long-standing challenge in the synthesis of catalysts, was recently studied. Thermal decomposition of the metal salt precursor, in particular the role of the gas composition or use of chelating agents, has also been systematically studied to elucidate the effects on particle size and particle distribution.

Besides these, several new or rejuvenated approaches were noticed. First, melt infiltration is a promising and facile technique for the preparation of catalysts with high metal loadings that bears many similarities to impregnation and drying, and as such could benefit from the extensive knowledge obtained recently on this method. Second, the synthesis of colloids in solution leads to unique control over particle size, shape, and composition and yields extensive literature. However, deposition of the formed colloids onto a support is critical but has been less studied. Third, the kinetics of particle growth in the presence of a support have been studied in real time for the first time using in situ catalytic measurements of the emerging catalyst. Fourth, atomic layer deposition is showing promise especially for deposition of nanoparticles, but

also for deposition of a stabilizing layer onto supported catalysts, for which further insight into the stabilizing effect and ability to obtain porous layers is desired.

On the basis of literature described in this review, it is clear that single (monometallic) particle properties can be largely controlled. To further advance the field of catalyst preparation, more detailed studies on the kinetics of particle formation¹³ for each of the preparation methods, as well as systematic studies to control the collective properties of the nanoparticles,¹⁵ and the controlled formation of bimetallic and core–shell particles,²⁶² are greatly desired. To achieve this, the development of in situ spectroscopic and microscopic techniques will be critical. In particular, X-ray-based techniques²⁶³ and liquid-cell TEM²⁶⁴ offer possibilities to study the genesis of particles in real time, while other advanced electron microscopy techniques such as cryo-TEM⁷⁹ and electron tomography²⁶⁵ offer information on the distribution of the precursor at different stages during preparation. Furthermore, surface science studies provide increased understanding of the influence of support hydroxylation and the preparation method,^{266,267} while X-ray²⁶⁸ and microbalance^{269,270} techniques offer increasingly accurate information on the adsorption of complexes on flat surfaces. Model supports are also essential since 2D model supports provide an excellent platform to study morphological and compositional changes of nanoparticles,²⁷¹ while 3D model supports are excellent to study the synthesis,⁷⁹ distribution, and stability²⁷² of metal nanoparticles in a more realistic environment, and other synthesis methods such as electrodeposition allow for precise control of the material.²⁷³ Combination of these and other techniques will provide key insights to further the rationalization of the synthesis of supported catalysts.

AUTHOR INFORMATION

Corresponding Author

*E-mail: K.P.deJong@uu.nl.

Notes

The authors declare no competing financial interest.

Biographies



Peter Munnik received his M.Sc. at Utrecht University in 2010. During his studies, he successfully completed an internship at the University of Sydney, Australia, and graduated cum laude with his thesis on the decomposition of supported transition-metal nitrates. Thereafter, he became a Ph.D. student in the Inorganic Chemistry and Catalysis group at Utrecht University under the supervision of K. P. de Jong and P. E. de Jongh, focusing on the synthesis–structure–performance

relationships of supported metal catalysts. He graduated cum laude in 2014 and is presently employed by Shell Global Solutions.



Petra E. de Jongh received her Ph.D. in photoelectrochemistry from Utrecht University in 1999, and worked for 5 years as a senior scientist and project leader at Philips Research Laboratories. Since 2004, she has been a member of the Inorganic Chemistry and Catalysis group of the Debye Institute for Nanomaterials Science at Utrecht University, where she was appointed Chair of Inorganic Nanomaterials in 2014. Her present research interest is supported nanoparticles and nanoporous materials, and the impact of nanosizing and confinement, especially for applications in heterogeneous catalysis and energy storage and conversion.



Krijn P. de Jong received his B.Sc. (1976), M.Sc. (1978), and Ph.D. (1982) in chemistry, all cum laude, at Utrecht University. In 1987, he also obtained an M.Sc. degree in chemical engineering from Twente University. From 1982 to 1997, he was with Shell Research working on catalyst preparation, heavy oil conversion, environmental processes, zeolite catalysis, and synthesis gas production and conversion. In 1997, he was appointed as Professor of Inorganic Chemistry and Catalysis at Utrecht University. His current research interests are catalyst synthesis, electron tomography of nanostructured catalysts, hydrocarbon conversions over zeolites, catalysts for liquid-phase catalysis, and conversion of synthesis gas to fuels and chemicals.

ACKNOWLEDGMENTS

PM acknowledges financial support from NWO-TOP-700.57.341, PEDJ from NWO-VICI-016.130.344 and KPdj from the European Research Council, ERC Advanced Grant no. 338846.

REFERENCES

- (1) Behrens, M.; Studt, F.; Kasatkin, I.; Kühl, S.; Hävecker, M.; Abild-Pedersen, F.; Zander, S.; Girgsdies, F.; Kurr, P.; Knief, B.-L.; Tovar, M.; Fischer, R. W.; Nørskov, J. K.; Schlögl, R. *Science* **2012**, *336*, 893.
- (2) Babich, I. V.; Moulijn, J. A. *Fuel* **2003**, *82*, 607.
- (3) Brown, D. E.; Edmonds, T.; Joyner, R. W.; McCarroll, J. J.; Tennison, S. R. *Catal. Lett.* **2014**, *144*, 545.
- (4) Torres Galvis, H. M.; Bitter, J. H.; Khare, C. B.; Ruitenbeek, M.; Dugulan, A. I.; de Jong, K. P. *Science* **2012**, *335*, 835.
- (5) Besson, M.; Gallezot, P.; Pinel, C. *Chem. Rev.* **2014**, *114*, 1827.
- (6) Huber, G. W.; Iborra, S.; Corma, A. *Chem. Rev.* **2006**, *106*, 4044.
- (7) Guo, X.; Fang, G.; Li, G.; Ma, H.; Fan, H.; Yu, L.; Ma, C.; Wu, X.; Deng, D.; Wei, M.; Tan, D.; Si, R.; Zhang, S.; Li, J.; Sun, L.; Tang, Z.; Pan, X.; Bao, X. *Science* **2014**, *344*, 616.
- (8) Transparency Market Research. Refinery (FCC, Hydrocracking, Catalytic Reforming), Synthesis, Polymer & Environmental Catalyst Market—Global Industry Analysis by Material (Zeolites, Metal, Others), by Type (Homogenous & Heterogeneous), Catalyst Regeneration (Off-Site & On-Site), Size, Share, Growth, Trends and Forecast 2012–2018, 2013. www.transparencymarketresearch.com/global-refinery-catalyst-market.html (accessed on January 2, 2015).
- (9) Freedonia Group. World Catalysts, 2013. www.freedoniagroup.com/world-catalysts.html (accessed on January 2, 2015).
- (10) Rabo, J. A. *Stud. Surf. Sci. Catal.* **1993**, *75*, 1.
- (11) De Jong, K. P. *CatTech* **1998**, *2*, 87.
- (12) Schwarz, J. A.; Contescu, C.; Contescu, A. *Chem. Rev.* **1995**, *95*, 477.
- (13) Mondloch, J. E.; Bayram, E.; Finke, R. G. *J. Mol. Catal. A* **2012**, *355*, 1.
- (14) Bartholomew, C. H. *Appl. Catal.* **2001**, *212*, 17.
- (15) Prieto, G.; Zečević, J.; Friedrich, H.; de Jong, K. P.; de Jongh, P. E. *Nat. Mater.* **2013**, *12*, 34.
- (16) Munnik, P.; de Jongh, P. E.; de Jong, K. P. *J. Am. Chem. Soc.* **2014**, *136*, 7333.
- (17) Van Santen, R. A. *Acc. Chem. Res.* **2009**, *42*, 57.
- (18) Lundwall, M. J.; McClure, S. M.; Wang, X.; Wang, Z.; Chen, M.; Goodman, D. W. *J. Phys. Chem. C* **2012**, *116*, 18155.
- (19) Bezemer, G. L.; Bitter, J. H.; Kuipers, H. P. C. E.; Oosterbeek, H.; Holeywijn, J. E.; Xu, X. D.; Kapteijn, F.; van Dillen, J. A.; de Jong, K. P. *J. Am. Chem. Soc.* **2006**, *128*, 3956.
- (20) Den Breejen, J. P.; Radstake, P. B.; Bezemer, G. L.; Bitter, J. H.; Frøseth, V.; Holmen, A.; de Jong, K. P. *J. Am. Chem. Soc.* **2009**, *131*, 7197.
- (21) Farmer, J. A.; Campbell, C. T. *Science* **2010**, *329*, 933.
- (22) Cao, A.; Vesper, G. *Nat. Mater.* **2010**, *9*, 75.
- (23) Holby, E. F.; Sheng, W.; Shao-Horn, Y.; Morgan, D. *Energy Environ. Sci.* **2009**, *2*, 865.
- (24) Munnik, P.; Velthoen, M.; de Jongh, P. E.; de Jong, K. P.; Gommers, C. *J. Angew. Chem., Int. Ed.* **2014**, *53*, 9493.
- (25) Li, W.; Yue, Q.; Deng, Y.; Zhao, D. *Adv. Mater.* **2013**, *25*, 5129.
- (26) Corma, A.; García, H.; Llabrés i Xamena, F. X. *Chem. Rev.* **2010**, *110*, 4606.
- (27) Pierre, A. C.; Pajonk, M. *Chem. Rev.* **2002**, *102*, 4243.
- (28) Hiemstra, T.; Venema, P.; Riemsdijk, W. *J. Colloid Interface Sci.* **1996**, *184*, 680.
- (29) Kosmulski, M. *J. Colloid Interface Sci.* **2011**, *353*, 1.
- (30) Barradas, S.; Caricato, E. A.; van Berge, P. J.; van de Loosdrecht, J. *Stud. Surf. Sci. Catal.* **2002**, *143*, 55.
- (31) Burattin, P.; Che, M.; Louis, C. *J. Phys. Chem. B* **1998**, *102*, 2722.
- (32) Kaluza, S.; Schröter, M. K.; Naumann d'Alnoncourt, R.; Reinecke, T.; Muhler, M. *Adv. Funct. Mater.* **2008**, *18*, 3670.
- (33) Kaluza, S.; Behrens, M.; Schiefenhövel, N.; Knief, B.; Fischer, R.; Schlögl, R.; Muhler, M. *ChemCatChem* **2011**, *3*, 189.
- (34) Villacampa, J. I.; Royo, C.; Romeo, E.; Montoya, J. A.; Del Angel, P.; Monzón, A. *Appl. Catal., A* **2003**, *252*, 363.
- (35) Shroff, M. D.; Kalakkad, D. S.; Coulter, K. E.; Kohler, S. D.; Harrington, M. S.; Jackson, N. B.; Sault, A. G.; Datye, A. K. *J. Catal.* **1995**, *156*, 185.

- (36) Behrens, M.; Schlögl, R. Z. *Anorg. Allg. Chem.* **2013**, 639, 2683.
- (37) Behrens, M.; Brennecke, D.; Girgsdies, F.; Kissner, S.; Trunschke, A.; Nasrudin, N.; Zakaria, S.; Idris, N. F.; Hamid, S. B. A.; Kniep, B.; Fischer, R.; Busser, W.; Muhler, M.; Schlögl, R. *Appl. Catal., A* **2011**, 392, 93.
- (38) Baltes, C.; Vukojevic, S.; Schuth, F. *J. Catal.* **2008**, 258, 334.
- (39) Zander, S.; Seidlhofer, B.; Behrens, M. *Dalton Trans.* **2012**, 41, 13413.
- (40) Behrens, M. *J. Catal.* **2009**, 267, 24.
- (41) Simson, G.; Prasetyo, E.; Reiner, S.; Hinrichsen, O. *Appl. Catal., A* **2013**, 450, 1.
- (42) Zhang, X.; Zhong, L.; Guo, Q.; Fan, H.; Zheng, H.; Xie, K. *Fuel* **2010**, 89, 1348.
- (43) Kowalik, P.; Konkol, M.; Kondracka, M.; Próchniak, W.; Bicki, R.; Wiercioch, P. *Appl. Catal., A* **2013**, 452, 139.
- (44) Budiman, A.; Ridwan, M.; Kim, S. M.; Choi, J.-W.; Yoon, C. W.; Ha, J.-M.; Suh, D. J.; Suh, Y.-W. *Appl. Catal., A* **2013**, 462–463, 220.
- (45) Li, Z.; Yan, S.; Fan, H. *Fuel* **2013**, 106, 178.
- (46) Behrens, M.; Kissner, S.; Girgsdies, F.; Kasatkin, I.; Hermerschmidt, F.; Mette, K.; Ruland, H.; Muhler, M.; Schlögl, R. *Chem. Commun.* **2011**, 47, 1701.
- (47) Prieto, G.; de Jong, K. P.; de Jongh, P. E. *Catal. Today* **2013**, 215, 142.
- (48) De Jong, K. P.; Geus, J. W. *Appl. Catal.* **1982**, 4, 41.
- (49) Lok, C. M. *Stud. Surf. Sci. Catal.* **2004**, 147, 283.
- (50) Bitter, J. H.; van der Lee, M. K.; Slotboom, A. G. T.; van Dillen, J. A.; de Jong, K. P. *Catal. Lett.* **2003**, 89, 139.
- (51) Fang, B.; Chaudhari, N. K.; Kim, M.-S.; Kim, J. H.; Yu, J.-S. *J. Am. Chem. Soc.* **2009**, 131, 15330.
- (52) Kim, M.-S.; Lim, S.; Chaudhari, N. K.; Fang, B.; Bae, T.-S.; Yu, J.-S. *Catal. Today* **2010**, 158, 354.
- (53) Bezemer, G. L.; Radstake, P. B.; Koot, V.; van Dillen, J. A.; Geus, J. W.; de Jong, K. P. *J. Catal.* **2006**, 237, 291.
- (54) Eschemann, T. O.; Bitter, J. H.; de Jong, K. P. *Catal. Today* **2014**, 228, 89.
- (55) Moreau, F.; Bond, G. C. *Appl. Catal., A* **2006**, 302, 110.
- (56) Moreau, F.; Bond, G.; Taylor, A. J. *Catal.* **2005**, 231, 105.
- (57) Moreau, F.; Bond, G. C. *Catal. Today* **2007**, 122, 215.
- (58) Fang, W.; Chen, J.; Zhang, Q.; Deng, W.; Wang, Y. *Chemistry* **2011**, 17, 1247.
- (59) Martin, R.; Navalon, S.; Delgado, J. J.; Calvino, J. J.; Alvaro, M.; Garcia, H. *Chemistry* **2011**, 17, 9494.
- (60) Lim, S. H.; Phonthammachai, N.; Zhong, Z.; Teo, J.; White, T. J. *Langmuir* **2009**, 25, 9480.
- (61) Yazid, H.; Adnan, R.; Farrukh, M. A.; Hamid, S. A. *J. Chin. Chem. Soc.* **2011**, 58, 593.
- (62) Souza, K. R.; de Lima, A. F. F.; de Sousa, F. F.; Appel, L. G. *Appl. Catal., A* **2008**, 340, 133.
- (63) Zanella, R.; Giorgio, S.; Henry, C. R.; Louis, C. J. *Phys. Chem. B* **2002**, 106, 7634.
- (64) Cellier, C.; Lambert, S.; Gaigneaux, E. M.; Poleunis, C.; Ruaux, V.; Eloy, P.; Lahousse, C.; Bertrand, P.; Pirard, J.-P.; Grange, P. *Appl. Catal., B* **2007**, 70, 406.
- (65) Moreau, F.; Bond, G. C. *Catal. Today* **2007**, 122, 260.
- (66) Zanella, R.; Delannoy, L.; Louis, C. *Appl. Catal., A* **2005**, 291, 62.
- (67) Hugon, A.; El Kolli, N.; Louis, C. *J. Catal.* **2010**, 274, 239.
- (68) Hugon, A.; Delannoy, L.; Krafft, J.; Louis, C. *J. Phys. Chem. C* **2010**, 114, 10823.
- (69) Ward, T.; Delannoy, L.; Hahn, R.; Kendell, S.; Pursell, C. J.; Louis, C.; Chandler, B. D. *ACS Catal.* **2013**, 3, 2644.
- (70) Cárdenas-Lizana, F.; Gómez-Quero, S.; Hugon, A.; Delannoy, L.; Louis, C.; Keane, M. A. *J. Catal.* **2009**, 262, 235.
- (71) Murzin, D. Y.; Simakova, O. A.; Simakova, I. L.; Parmon, V. N. *React. Kinet. Mech. Catal.* **2011**, 104, 259.
- (72) Van Honschoten, J. W.; Brunets, N.; Tas, N. R. *Chem. Soc. Rev.* **2010**, 39, 1096.
- (73) Washburn, E. W. *Phys. Rev.* **1921**, 17, 273.
- (74) Haneveld, J.; Tas, N. R.; Brunets, N.; Jansen, H. V.; Elwenspoek, M. *J. Appl. Phys.* **2008**, 104, 014309.
- (75) Liu, X.; Khinast, J. G.; Glasser, B. J. *Chem. Eng. Sci.* **2008**, 63, 4517.
- (76) Imperor-Clerc, M.; Bazin, D.; Appay, M.; Beaunier, P.; Davidson, A. *Chem. Mater.* **2004**, 16, 1813.
- (77) Moreno, M. S.; Weyland, M.; Midgley, P. A.; Bengoa, J. F.; Cagnoli, M. V.; Gallegos, N. G.; Alvarez, A. M.; Marchetti, S. G. *Micron* **2006**, 37, 52.
- (78) Sietsma, J. R. A.; Meeldijk, J. D.; Versluijs-Helder, M.; Broersma, A.; van Dillen, J. A.; de Jongh, P. E.; de Jong, K. P. *Chem. Mater.* **2008**, 2921.
- (79) Eggenhuisen, T. M.; Friedrich, H.; Nudelman, F.; Zečević, J.; Sommerdijk, N. A. J. M.; de Jongh, P. E.; de Jong, K. P. *Chem. Mater.* **2013**, 25, 890.
- (80) Eggenhuisen, T. M.; van Steenberghe, M. J.; Talsma, H.; de Jongh, P. E.; de Jong, K. P. *J. Phys. Chem. C* **2009**, 113, 16785.
- (81) Cornu, C.; Bonardet, J. L.; Casale, S.; Davidson, A.; Ambramson, S.; Andre, G.; Porcher, F.; Grcic, I.; Tomasic, V.; Vujec, D.; Koprivanac, N. *J. Phys. Chem. C* **2012**, 116, 3437.
- (82) Marceau, E.; Che, M.; Čejka, J.; Zukal, A. *ChemCatChem* **2010**, 2, 413.
- (83) Boubekr, F.; Davidson, A.; Casale, S.; Massiani, P. *Microporous Mesoporous Mater.* **2011**, 141, 157.
- (84) Van der Meer, J.; Bardez-Giboire, I.; Bart, F.; Albouy, P.; Wallez, G.; Davidson, A. *Microporous Mesoporous Mater.* **2009**, 118, 183.
- (85) Van der Meer, J.; Bardez-Giboire, I.; Mercier, C.; Revel, B.; Davidson, A.; Denoyel, R. *J. Phys. Chem. C* **2010**, 114, 3507.
- (86) Park, J.; Regalbuto, J. R. *J. Colloid Interface Sci.* **1995**, 175, 239.
- (87) Bourikas, K.; Kordulis, C.; Lycourghiotis, A. *Catal. Rev.* **2006**, 48, 363.
- (88) Hao, X.; Spieker, W. A.; Regalbuto, J. R. *J. Colloid Interface Sci.* **2003**, 267, 259.
- (89) Agashe, K.; Regalbuto, J. R. *J. Colloid Interface Sci.* **1997**, 185, 174.
- (90) Jiao, L.; Regalbuto, J. R. *J. Catal.* **2008**, 260, 329.
- (91) Jiao, L.; Regalbuto, J. R. *J. Catal.* **2008**, 260, 342.
- (92) Lambert, S.; Job, N.; Dsouza, L.; Pereira, M.; Pirard, R.; Heinrichs, B.; Figueiredo, J.; Pirard, J.; Regalbuto, J. R. *J. Catal.* **2009**, 261, 23.
- (93) Hao, X.; Barnes, S.; Regalbuto, J. R. *J. Catal.* **2011**, 279, 48.
- (94) Job, N.; Lambert, S.; Chatenet, M.; Gommès, C. J.; Maillard, F.; Berthon-Fabry, S.; Regalbuto, J. R.; Pirard, J.-P. *Catal. Today* **2010**, 150, 119.
- (95) Dsouza, L.; Jiao, L.; Regalbuto, J. R.; Miller, J.; Kropf, A. *J. Catal.* **2007**, 248, 165.
- (96) Dsouza, L.; Regalbuto, J. R.; Miller, J. *J. Catal.* **2008**, 254, 157.
- (97) Zhu, X.; Cho, H.; Pasupong, M.; Regalbuto, J. R. *ACS Catal.* **2013**, 3, 625.
- (98) Feltes, T. E.; Espinosa-Alonso, L.; de Smit, E.; D'Souza, L.; Meyer, R. J.; Weckhuysen, B. M.; Regalbuto, J. R. *J. Catal.* **2010**, 270, 95.
- (99) Feltes, T. E.; Zhao, Y.; Klie, R. F.; Meyer, R. J.; Regalbuto, J. R. *ChemCatChem* **2010**, 2, 1065.
- (100) Zhao, Y.; Feltes, T. E.; Regalbuto, J. R.; Meyer, R. J.; Klie, R. F. *Catal. Sci. Technol.* **2011**, 1, 1483.
- (101) Liu, J.; Tao, R.; Guo, Z.; Regalbuto, J. R.; Marshall, C. L.; Klie, R. F.; Miller, J. T.; Meyer, R. J. *ChemCatChem* **2013**, 5, 3665.
- (102) Petsi, T.; Panagiotou, G. D.; Garoufalis, C. S.; Kordulis, C.; Stathi, P.; Deligiannakis, Y.; Lycourghiotis, A.; Bourikas, K. *Chem.—Eur. J.* **2009**, 15, 13090.
- (103) Panagiotou, G. D.; Petsi, T.; Bourikas, K.; Kordulis, C.; Lycourghiotis, A. *J. Catal.* **2009**, 262, 266.
- (104) Panagiotou, G. D.; Petsi, T.; Bourikas, K.; Kalamounias, A. G.; Boghosian, S.; Kordulis, C.; Lycourghiotis, A. *J. Phys. Chem. C* **2010**, 114, 11868.
- (105) Petsi, T.; Panagiotou, G. D.; Bourikas, K.; Kordulis, C.; Voyiatzis, G. A.; Lycourghiotis, A. *ChemCatChem* **2011**, 3, 1072.

- (106) Bourikas, K.; Stavropoulos, J.; Garoufalos, C. S.; Kordulis, C.; Petsi, T.; Lycourghiotis, A. *Chem.—Eur. J.* **2011**, *17*, 1201.
- (107) Bourikas, K.; Vakros, J.; Fountzoula, C.; Kordulis, C.; Lycourghiotis, A. *Catal. Today* **2007**, *128*, 138.
- (108) Zacharaki, I.; Kontoyannis, C. G.; Boghosian, S.; Lycourghiotis, A.; Kordulis, C. *Catal. Today* **2009**, *143*, 38.
- (109) Li, H.; Li, M.; Chu, Y.; Liu, F.; Nie, H. *Fuel* **2014**, *116*, 168.
- (110) Sun, K.-Q.; Marceau, E.; Che, M. *Phys. Chem. Chem. Phys.* **2006**, *8*, 1731.
- (111) Lee, S. Y.; Aris, R. *Catal. Rev.: Sci. Eng.* **1985**, *27*, 207.
- (112) Neimark, A. V.; Kheifetz, L. I.; Felonov, V. B. *Ind. Eng. Chem. Prod. Res. Dev.* **1981**, *439*.
- (113) Espinosa-Alonso, L.; Beale, A. M.; Weckhuysen, B. M. *Acc. Chem. Res.* **2010**, *43*, 1279.
- (114) Bergwerff, J. A.; Visser, T.; Leliveld, B. R. G.; Rossenaar, B. D.; de Jong, K. P.; Weckhuysen, B. M. *J. Am. Chem. Soc.* **2004**, *126*, 14548.
- (115) Zandbergen, M. W.; Jacques, S. D. M.; Weckhuysen, B. M.; Beale, A. M. *Angew. Chem., Int. Ed.* **2012**, *51*, 957.
- (116) Gibson, E. K.; Zandbergen, M. W.; Jacques, S. D. M.; Biao, C.; Cernik, R. J.; Brien, M. G. O.; Di Michiel, M.; Weckhuysen, B. M.; Beale, A. M. *ACS Catal.* **2013**, *3*, 339.
- (117) Bergwerff, J. A.; Lysova, A. A.; Espinosa-Alonso, L.; Koptuyg, I. V.; Weckhuysen, B. M. *Angew. Chem., Int. Ed.* **2007**, *46*, 7224.
- (118) Van de Water, L. G. A.; Bezemer, G. L.; Bergwerff, J. A.; Versluijs-Helder, M.; Weckhuysen, B. M.; de Jong, K. P. *J. Catal.* **2006**, *242*, 287.
- (119) Bergwerff, J. A.; Lysova, A. A.; Espinosa-Alonso, L.; Koptuyg, I. V.; Weckhuysen, B. M. *Chem.—Eur. J.* **2008**, *14*, 2363.
- (120) Espinosa-Alonso, L.; de Jong, K. P.; Weckhuysen, B. M. *J. Phys. Chem. C* **2008**, *112*, 7201.
- (121) Espinosa-Alonso, L.; Lysova, A. A.; de Peinder, P.; de Jong, K. P.; Koptuyg, I. V.; Weckhuysen, B. M. *J. Am. Chem. Soc.* **2009**, *131*, 6525.
- (122) Zandbergen, M. W.; Beale, A. M.; Weckhuysen, I. B. M. *ChemCatChem* **2012**, *4*, 217.
- (123) Espinosa-Alonso, L.; de Jong, K. P.; Weckhuysen, B. M. *Phys. Chem. Chem. Phys.* **2010**, *12*, 97.
- (124) Lekhal, A.; Glasser, B. J.; Khinast, J. G. *Chem. Eng. Sci.* **2001**, *56*, 4473.
- (125) Van Dillen, J. A.; Terorde, R.; Lensveld, D.; Geus, J.; de Jong, K. P. *J. Catal.* **2003**, *216*, 257.
- (126) Torres Galvis, H. M.; Koeken, A. C. J.; Bitter, J. H.; Davidian, T.; Ruitenbeek, M.; Dugulan, A. I.; de Jong, K. P. *Catal. Today* **2013**, *215*, 95.
- (127) Qiu, S.; Zhang, X.; Liu, Q.; Wang, T.; Zhang, Q.; Ma, L. *Catal. Commun.* **2013**, *42*, 73.
- (128) Lysova, A. A.; Bergwerff, J. A.; Espinosa-Alonso, L.; Weckhuysen, B. M.; Koptuyg, I. V. *Appl. Catal., A* **2010**, *374*, 126.
- (129) Liu, X.; Khinast, J. G.; Glasser, B. J. *Ind. Eng. Chem. Res.* **2010**, *49*, 2649.
- (130) Liu, X.; Khinast, J. G.; Glasser, B. J. *Chem. Eng. Sci.* **2012**, *79*, 187.
- (131) Bergwerff, J. A.; Jansen, M.; Leliveld, B. R. G.; Visser, T.; de Jong, K. P.; Weckhuysen, B. J. *Catal.* **2006**, *243*, 292.
- (132) Arslan, I.; Walmsley, J. C.; Rytter, E.; Bergene, E.; Midgley, P. A. *J. Am. Chem. Soc.* **2008**, *130*, 5716.
- (133) Borg, Ø.; Walmsley, J. C.; Dehghan, R.; Tanem, B. S.; Blekkan, E. A.; Eri, S.; Rytter, E.; Holmen, A. *Catal. Lett.* **2008**, *126*, 224.
- (134) van de Loosdrecht, J.; Datt, M.; Visagie, J. L. *Top. Catal.* **2013**, *57*, 430.
- (135) Borg, Ø.; Dietzel, P. D. C.; Spjelkavik, A. I.; Tveten, E. Z.; Walmsley, J. C.; Diplas, S.; Eri, S.; Holmen, A.; Rytter, E. *J. Catal.* **2008**, *259*, 161.
- (136) Banerjee, R.; Crozier, P. A. *J. Phys. Chem. C* **2012**, *116*, 11486.
- (137) Wolters, M.; Munnik, P.; Bitter, J. H.; de Jongh, P. E.; de Jong, K. P. *J. Phys. Chem. C* **2011**, *115*, 3332.
- (138) Munnik, P.; Krans, N. A.; de Jongh, P. E.; de Jong, K. P. *ACS Catal.* **2014**, *4*, 3219.
- (139) Stannard, A.; Martin, C. P.; Pauliac-Vaujour, E.; Moriarty, P.; Thiele, U. *J. Phys. Chem. C* **2008**, *112*, 15195.
- (140) Stannard, A. *J. Phys.: Condens. Matter* **2011**, *23*, 083001.
- (141) Sun, X.; Shi, Y.; Zhang, P.; Zheng, C.; Zheng, X.; Zhang, F.; Zhang, Y.; Guan, N.; Zhao, D.; Stucky, G. D. *J. Am. Chem. Soc.* **2011**, *133*, 14542.
- (142) Eggenhuisen, T. M.; Munnik, P.; Talsma, H.; de Jongh, P. E.; de Jong, K. P. *J. Catal.* **2013**, *297*, 306.
- (143) Van de Loosdrecht, J.; Barradas, S.; Caricato, E. A.; Ngwenya, N. G.; Nkwanyana, P. S.; Rawat, M.; Sigwebela, B. H.; van Berge, P. J.; Visagie, J. L. *Top. Catal.* **2003**, *26*, 121.
- (144) Borg, Ø.; Blekkan, E. A.; Eri, S.; Akporiaye, D.; Vigerust, B.; Rytter, E.; Holmen, A. *Top. Catal.* **2007**, *45*, 39.
- (145) Sietsma, J. R. A.; Meeldijk, J. D.; den Breejen, J. P.; Versluijs-Helder, M.; van Dillen, J. A.; de Jongh, P. E.; de Jong, K. P. *Angew. Chem., Int. Ed.* **2007**, *46*, 4547.
- (146) Sietsma, J. R. A.; Friedrich, H.; Broersma, A.; Versluijs-Helder, M.; Jos van Dillen, A.; de Jongh, P. E.; de Jong, K. P. *J. Catal.* **2008**, *260*, 227.
- (147) Wolters, M.; Daly, H.; Goguet, A.; Meunier, F. C.; Hardacre, C.; Bitter, J. H.; de Jongh, P. E.; de Jong, K. P. *J. Phys. Chem. C* **2010**, *114*, 7839.
- (148) Wolters, M.; Andrade, I. C. A. C.; Munnik, P.; Bitter, J. H.; de Jongh, P. E.; de Jong, K. P. *Stud. Surf. Sci. Catal.* **2010**, *175*, 69.
- (149) Wolters, M.; van Grotel, L. J. W.; Eggenhuisen, T. M.; Sietsma, J. R. A.; de Jong, K. P.; de Jongh, P. E. *Catal. Today* **2011**, *163*, 27.
- (150) Hong, J.; Marceau, E.; Khodakov, A. Y.; Griboval-Constant, A.; La Fontaine, C.; Briois, V. *Chem.—Eur. J.* **2012**, *2802*.
- (151) Becker, H.; Turek, T.; Güttel, R. *Catal. Today* **2013**, *215*, 8.
- (152) Jacobs, G.; Ma, W.; Davis, B. H.; Cronauer, D. C.; Jeremy Kropf, A.; Marshall, C. L. *Catal. Lett.* **2010**, *140*, 106.
- (153) Munnik, P.; Wolters, M.; Gabriëlsson, A.; Pollington, S. D.; Headdock, G.; Bitter, J. H.; de Jongh, P. E.; de Jong, K. P. *J. Phys. Chem. C* **2011**, *115*, 14698.
- (154) Coulier, L.; de Beer, V. H. J.; van Veen, J. A. R.; Niemantsverdriet, J. W. *Top. Catal.* **2000**, *13*, 99.
- (155) Coulier, L.; de Beer, V. H. J.; van Veen, J. A. R.; Niemantsverdriet, J. W. *J. Catal.* **2001**, *197*, 26.
- (156) Kishan, G.; van Veen, J. A. R.; Niemantsverdriet, J. W. *Top. Catal.* **2004**, *29*, 103.
- (157) Kishan, G.; Coulier, L.; de Beer, V. H. J.; van Veen, J. A. R.; Niemantsverdriet, J. W. *J. Catal.* **2000**, *196*, 180.
- (158) Mochizuki, T.; Hara, T.; Koizumi, N.; Yamada, M. *Appl. Catal., A* **2007**, *317*, 97.
- (159) Mochizuki, T.; Hara, T.; Koizumi, N.; Yamada, M. *Catal. Lett.* **2007**, *113*, 165.
- (160) Koizumi, N.; Mochizuki, T.; Yamada, M. *Catal. Today* **2009**, *141*, 34.
- (161) Mochizuki, T.; Hongo, D.; Satoh, T.; Koizumi, N.; Yamada, M. *Catal. Lett.* **2008**, *121*, 52.
- (162) Koizumi, N.; Ibi, Y.; Hongo, D.; Hamabe, Y.; Suzuki, S.; Hayasaka, Y.; Shindo, T.; Yamada, M. *J. Catal.* **2012**, *289*, 151.
- (163) Rane, S.; Borg, Ø.; Yang, J.; Rytter, E.; Holmen, A. *Appl. Catal., A* **2010**, *388*, 160.
- (164) Rane, S.; Borg, Ø.; Rytter, E.; Holmen, A. *Appl. Catal., A* **2012**, *437–438*, 10.
- (165) Koizumi, N.; Suzuki, S.; Niiyama, S.; Ibi, Y.; Shindo, T.; Yamada, M. *Appl. Catal., A* **2011**, *395*, 138.
- (166) Koizumi, N.; Suzuki, S.; Niiyama, S.; Shindo, T.; Yamada, M. *Catal. Lett.* **2011**, *141*, 931.
- (167) Hong, J.; Marceau, E.; Khodakov, A. Y.; Griboval-Constant, A.; La, C.; Briois, V.; Chernavskii, P. A. *Catal. Today* **2011**, *175*, 528.
- (168) Girardon, J. S.; Quinet, E.; Gribovalconstant, A.; Chernavskii, P.; Gengembre, L.; Khodakov, A. Y. *J. Catal.* **2007**, *248*, 143.
- (169) Girardon, J. S.; Lermontov, A. S.; Gengembre, L.; Chernavskii, P. A. *J. Catal.* **2005**, *230*, 339.
- (170) Bae, J. W.; Kim, S.-M.; Kang, S.-H.; Chary, K. V. R.; Lee, Y.-J.; Kim, H.-J.; Jun, K.-W. *J. Mol. Catal. A* **2009**, *311*, 7.

- (171) Rodríguez-González, V.; Marceau, E.; Beaunier, P.; Che, M.; Train, C. *J. Solid State Chem.* **2007**, *180*, 22.
- (172) Marceau, E.; Löfberg, A.; Giraudon, J.-M.; Négrier, F.; Che, M.; Leclercq, L. *Appl. Catal., A* **2009**, *362*, 34.
- (173) Zou, J.-J.; Zhang, Y.; Liu, C.-J. *Langmuir* **2006**, *22*, 11388.
- (174) Liang, X.; Liu, C.; Kuai, P. *Green Chem.* **2008**, *10*, 1318.
- (175) Zhao, Y.; Pan, Y.; Xie, Y.; Liu, C. *Catal. Commun.* **2008**, *9*, 1558.
- (176) Chen, Y.; Wang, H.; Liu, C.-J.; Zeng, Z.; Zhang, H.; Zhou, C.; Jia, X.; Yang, Y. *J. Catal.* **2012**, *289*, 105.
- (177) Chu, W.; Wang, L. N.; Chernavskii, P. A.; Khodakov, A. Y. *Angew. Chem., Int. Ed.* **2008**, *47*, 5052.
- (178) Hong, J.; Chu, W.; Chernavskii, P. A.; Khodakov, A. Y. *J. Catal.* **2010**, *273*, 9.
- (179) Yu, X.; Zhang, F.; Wang, N.; Hao, S.; Chu, W. *Catal. Lett.* **2013**, *144*, 293.
- (180) Zhu, X.; Huo, P.; Zhang, Y.; Cheng, D.; Liu, C. *Appl. Catal., B* **2008**, *81*, 132.
- (181) Zou, J.-J.; He, H.; Cui, L.; Du, H.-Y. *Int. J. Hydrogen Energy* **2007**, *32*, 1762.
- (182) Huang, C.; Bai, S.; Lv, J.; Li, Z. *Catal. Lett.* **2011**, *141*, 1391.
- (183) Odedairo, T.; Chen, J.; Zhu, Z. *J. Phys. Chem. C* **2013**, *117*, 21288.
- (184) De Jongh, P. E.; Eggenhuisen, T. M. *Adv. Mater.* **2013**, *25*, 6672.
- (185) *Handbook of Chemistry and Physics*, 92nd ed.; CRC Press: Boca Raton, FL, 2012.
- (186) Schüth, F.; Wingen, A.; Sauer, J. *Microporous Mesoporous Mater.* **2001**, *45*, 465.
- (187) Yue, W.; Zhou, W. *Chem. Mater.* **2007**, *19*, 2359.
- (188) Tang, C.; Zhang, H.; Sun, C.; Li, J.; Qi, L.; Quan, Y.; Gao, F.; Dong, L. *Catal. Commun.* **2011**, *12*, 1075.
- (189) Eggenhuisen, T. M.; den Breejen, J. P.; Verdoes, D.; de Jongh, P. E.; de Jong, K. P. *J. Am. Chem. Soc.* **2010**, *132*, 18318.
- (190) Li, X.; Quek, X.-Y.; Michel Ligthart, D. A. J.; Guo, M.; Zhang, Y.; Li, C.; Yang, Q.; Hensen, E. J. M. *Appl. Catal., B* **2012**, *123–124*, 424.
- (191) Tang, C.; Sun, J.; Yao, X.; Cao, Y.; Liu, L.; Ge, C.; Gao, F.; Dong, L. *Appl. Catal., B* **2014**, *146*, 201.
- (192) Boulaoued, A.; Fechet, I.; Donnio, B.; Bernard, M.; Turek, P.; Garin, F. *Microporous Mesoporous Mater.* **2012**, *155*, 131.
- (193) Medina-Mendoza, A. K.; Cortés-Jácome, M. A.; Toledo-Antonio, J. A.; Angeles-Chávez, C.; López-Salinas, E.; Cuauhtémoc-López, I.; Barrera, M. C.; Escobar, J.; Navarrete, J.; Hernández, I. *Appl. Catal., B* **2011**, *106*, 14.
- (194) Iglesia, E.; Soled, S. L.; Baumgartner, J. E.; Reyes, S. C. *J. Catal.* **1995**, *153*, 108.
- (195) Liu, X.; Khinast, J. G.; Glasser, B. J. *Ind. Eng. Chem. Res.* **2014**, *53*, 5792.
- (196) Tao, A. R.; Habas, S.; Yang, P. *Small* **2008**, *4*, 310.
- (197) Casavola, M.; Buonsanti, R.; Caputo, G.; Davide, P. *Eur. J. Inorg. Chem.* **2008**, 837.
- (198) Park, J.; Joo, J.; Kwon, S. G.; Jang, Y.; Hyeon, T. *Angew. Chem., Int. Ed.* **2007**, *46*, 4630.
- (199) Jia, C.-J.; Schüth, F. *Phys. Chem. Chem. Phys.* **2011**, *13*, 2457.
- (200) You, H.; Yang, S.; Ding, B.; Yang, H. *Chem. Soc. Rev.* **2013**, *42*, 2880.
- (201) Guo, S.; Zhang, S.; Sun, S. *Angew. Chem., Int. Ed.* **2013**, *52*, 8526.
- (202) An, K.; Somorjai, G. A. *ChemCatChem* **2012**, *4*, 1512.
- (203) Gross, A. F.; Diehl, M. R.; Beverly, K. C.; Richman, E. K.; Tolbert, S. H. *J. Phys. Chem. B* **2003**, *107*, 5475.
- (204) Hondow, N.; Fuller, R. O. *J. Colloid Interface Sci.* **2014**, *417*, 396.
- (205) Witte, P. T.; Boland, S.; Kirby, F.; van Maanen, R.; Bleeker, B. F.; de Winter, D. A. M.; Post, J. A.; Geus, J. W.; Berben, P. H. *ChemCatChem* **2013**, *5*, 582.
- (206) Zhu, J.; Zhao, T.; Kvande, I.; Chen, D.; Zhou, X.; Yuan, W. *Chin. J. Catal.* **2008**, *29*, 1145.
- (207) Kvande, I.; Zhu, J.; Zhao, T.-J.; Hammer, N.; Rønning, M.; Raaen, S.; Walmsley, J. C.; Chen, D. *J. Phys. Chem. C* **2010**, *114*, 1752.
- (208) Muthuswamy, N.; de la Fuente, J. L. G.; Ochal, P.; Giri, R.; Raaen, S.; Sunde, S.; Rønning, M.; Chen, D. *Phys. Chem. Chem. Phys.* **2013**, *15*, 3803.
- (209) Kimura, K.; Einaga, H.; Teraoka, Y. *Catal. Today* **2011**, *164*, 88.
- (210) Witte, P. T.; Berben, P. H.; Boland, S.; Boymans, E. H.; Vogt, D.; Geus, J. W.; Donkervoort, J. G. *Top. Catal.* **2012**, *55*, 505.
- (211) Liu, Y.; Tsunoyama, H.; Akita, T.; Tsukuda, T. *J. Phys. Chem. C* **2009**, *113*, 13457.
- (212) Villa, A.; Wang, D.; Su, D.; Veith, G. M.; Prati, L. *Phys. Chem. Chem. Phys.* **2010**, *12*, 2183.
- (213) Mori, K.; Kumami, A.; Tomonari, M.; Yamashita, H. *J. Phys. Chem. C* **2009**, *113*, 16850.
- (214) Rinaldi, R.; Porcari, A. D. M.; Rocha, T. C. R.; Cassinelli, W. H.; Ribeiro, R. U.; Bueno, J. M. C.; Zanchet, D. *J. Mol. Catal. A* **2009**, *301*, 11.
- (215) Lopez-Sanchez, J. A.; Dimitratos, N.; Hammond, C.; Brett, G. L.; Kesavan, L.; White, S.; Miedziak, P.; Tiruvalam, R.; Jenkins, R. L.; Carley, A. F.; Knight, D.; Kiely, C. J.; Hutchings, G. J. *Nat. Chem.* **2011**, *3*, 551.
- (216) Lin, J.-H.; Gulians, V. V. *ChemCatChem* **2011**, *3*, 1426.
- (217) Fischer, N.; Minnermann, M.; Baeumer, M.; van Steen, E.; Claeys, M. *Catal. Lett.* **2012**, *142*, 830.
- (218) Martínez, A.; Prieto, G. *Catal. Commun.* **2007**, *8*, 1479.
- (219) Mondloch, J. E.; Yan, X.; Finke, R. G. *J. Am. Chem. Soc.* **2009**, *131*, 6389.
- (220) Watzky, M. A.; Finke, R. G. *J. Am. Chem. Soc.* **1997**, *119*, 10382.
- (221) Mondloch, J. E.; Wang, Q.; Frenkel, A. I.; Finke, R. G. *J. Am. Chem. Soc.* **2010**, *132*, 9701.
- (222) Mondloch, J. E.; Finke, R. G. *J. Am. Chem. Soc.* **2011**, *133*, 7744.
- (223) Mondloch, J. E.; Finke, R. G. *ACS Catal.* **2012**, *2*, 298.
- (224) Kent, P.; Mondloch, J. E.; Finke, R. G. *J. Am. Chem. Soc.* **2014**, *136*, 1930.
- (225) Li, G.; Tang, Z. *Nanoscale* **2014**, *6*, 3995.
- (226) An, K.; Somorjai, G. A. *Catal. Lett.* **2014**, 233.
- (227) Ma, Z.; Dai, S. *ACS Catal.* **2011**, *1*, 805.
- (228) Stair, P. C. *Top. Catal.* **2012**, *55*, 93.
- (229) Miiikulainen, V.; Leskelä, M.; Ritala, M.; Puurunen, R. L. *J. Appl. Phys.* **2013**, *113*, 021301.
- (230) Molenbroek, A. M.; Haukka, S.; Clausen, B. S. *J. Phys. Chem. B* **1998**, *102*, 10680.
- (231) Lashdaf, M.; Hatanpää, T.; Krause, A. O. I.; Lahtinen, J.; Lindblad, M.; Tiitta, M. *Appl. Catal., A* **2003**, *241*, 51.
- (232) Lindblad, M.; Peter, L.; Suntola, T. *Catal. Lett.* **1994**, *27*, 323.
- (233) Backman, L.; Rautiainen, A.; Lindblad, M.; Krause, A. O. I. *Appl. Catal., A* **2000**, *191*, 55.
- (234) Backman, L. B.; Rautiainen, A.; Krause, A. O. I.; Lindblad, M. *Catal. Today* **1998**, *43*, 11.
- (235) Haukka, S.; Lakomaa, E.; Suntola, T. *Appl. Surf. Sci.* **1994**, *75*, 220.
- (236) Keränen, J.; Auroux, A.; Ek, S.; Niinistö, L. *Appl. Catal., A* **2002**, *228*, 213.
- (237) Backman, L. B.; Rautiainen, A.; Lindblad, M.; Krause, A. O. I. *Appl. Catal., A* **2009**, *360*, 183.
- (238) Keranen, J.; Guimon, C.; Iiskola, E.; Auroux, A.; Niinistö, L. *J. Phys. Chem. B* **2003**, *107*, 10773.
- (239) Kucheyev, S. O.; Biener, J.; Wang, Y. M.; Baumann, T. F.; Wu, K. J.; van Buuren, T.; Hamza, A. V.; Satcher, J. H.; Elam, J. W.; Pellin, M. J. *Appl. Phys. Lett.* **2005**, *86*, 083108.
- (240) Kucheyev, S. O.; Biener, J.; Baumann, T. F.; Wang, Y. M.; Hamza, A. V.; Li, Z.; Lee, D. K.; Gordon, R. G. *Langmuir* **2008**, *24*, 943.
- (241) King, J. S.; Wittstock, A.; Biener, J.; Kucheyev, S. O.; Wang, Y. M.; Baumann, T. F.; Giri, S. K.; Hamza, A. V.; Baeumer, M.; Bent, S. F. *Nano Lett.* **2008**, *8*, 2405.

- (242) Feng, H.; Elam, J. W.; Libera, J. A.; Setthapun, W.; Stair, P. C. *Chem. Mater.* **2010**, *22*, 3133.
- (243) Lu, J.; Stair, P. C. *Langmuir* **2010**, *26*, 16486.
- (244) Goldstein, D. N.; George, S. M. *Appl. Phys. Lett.* **2009**, *95*, 143106.
- (245) Setthapun, W.; Williams, W. D.; Kim, S. M.; Feng, H.; Elam, J. W.; Rabuffetti, F. A.; Poepelmeier, K. R.; Stair, P. C.; Stach, E. A.; Ribeiro, F. H.; Miller, J. T.; Marshall, C. L. *J. Phys. Chem. C* **2010**, *114*, 9758.
- (246) Li, J.; Liang, X.; King, D. M.; Jiang, Y.-B.; Weimer, A. W. *Appl. Catal., B* **2010**, *97*, 220.
- (247) Christensen, S. T.; Feng, H.; Libera, J. L.; Guo, N.; Miller, J. T.; Stair, P. C.; Elam, J. W. *Nano Lett.* **2010**, *10*, 3047.
- (248) Lei, Y.; Liu, B.; Lu, J.; Lobo-Lapidus, R. J.; Wu, T.; Feng, H.; Xia, X.; Mane, A. U.; Libera, J. A.; Greeley, J. P.; Miller, J. T.; Elam, J. W. *Chem. Mater.* **2012**, *24*, 3525.
- (249) Cronauer, D. C.; Elam, J. W.; Kropf, A. J.; Marshall, C. L.; Gao, P.; Hopps, S.; Jacobs, G.; Davis, B. H. *Catal. Lett.* **2012**, *142*, 698.
- (250) Lu, J.; Stair, P. C. *Angew. Chem., Int. Ed.* **2010**, *49*, 2547.
- (251) Feng, H.; Lu, J.; Stair, P. C.; Elam, J. W. *Catal. Lett.* **2011**, *141*, 512.
- (252) Lu, J.; Liu, B.; Greeley, J. P.; Feng, Z.; Libera, J. A.; Lei, Y.; Bedzyk, M. J.; Stair, P. C.; Elam, J. W. *Chem. Mater.* **2012**, *24*, 2047.
- (253) Lu, J.; Fu, B.; Kung, M. C.; Xiao, G.; Elam, J. W.; Kung, H. H.; Stair, P. C. *Science* **2012**, *335*, 1205.
- (254) Fu, B.; Lu, J.; Stair, P. C.; Xiao, G.; Kung, M. C.; Kung, H. H. *J. Catal.* **2013**, *297*, 289.
- (255) Ray, N. A.; Van Duyne, R. P.; Stair, P. C. *J. Phys. Chem. C* **2012**, *116*, 7748.
- (256) Liang, X.; Li, J.; Yu, M.; McMurray, C. N.; Falconer, J. L.; Weimer, A. W. *ACS Catal.* **2011**, *1*, 1162.
- (257) O'Neill, B. J.; Jackson, D. H. K.; Crisci, A. J.; Farberow, C. A.; Shi, F.; Alba-Rubio, A. C.; Lu, J.; Dietrich, P. J.; Gu, X.; Marshall, C. L.; Stair, P. C.; Elam, J. W.; Miller, J. T.; Ribeiro, F. H.; Voyles, P. M.; Greeley, J.; Mavrikakis, M.; Scott, S. L.; Kuech, T. F.; Dumesic, J. A. *Angew. Chem., Int. Ed.* **2013**, *52*, 13808.
- (258) Alba-Rubio, A. C.; O'Neill, B. J.; Shi, F.; Akatay, C.; Canlas, C.; Li, T.; Winans, R.; Elam, J. W.; Stach, E. A.; Voyles, P. M.; Dumesic, J. A. *ACS Catal.* **2014**, *4*, 1554.
- (259) Pagan-Torres, Y. J.; Gallo, J. M. R.; Wang, D.; Pham, H. N.; Libera, J. A.; Marshall, C. L.; Elam, J. W.; Datye, A. K.; Dumesic, J. A. *ACS Catal.* **2011**, *1*, 1234.
- (260) Paracchino, A.; Laporte, V.; Sivula, K.; Grätzel, M.; Thimsen, E. *Nat. Mater.* **2011**, *10*, 456.
- (261) Scott, I. D.; Jung, Y. S.; Cavanagh, A. S.; Yan, Y.; Dillon, A. C.; George, S. M.; Lee, S.-H. *Nano Lett.* **2011**, *11*, 414.
- (262) Calderone, V. R.; Shiju, N. R.; Curulla-Ferré, D.; Chambrey, S.; Khodakov, A. Y.; Rose, A.; Thiessen, J.; Jess, A.; Rothenberg, G. *Angew. Chem., Int. Ed.* **2013**, *52*, 4397.
- (263) Filez, M.; Poelman, H.; Ramachandran, R. K.; Dendooven, J.; Devloo-Casier, K.; Fonda, E.; Detavernier, C.; Marin, G. B. *Catal. Today* **2014**, *229*, 2.
- (264) Evans, J. E.; Jungjohann, K. L.; Browning, N. D.; Arslan, I. *Nano Lett.* **2011**, *11*, 2809.
- (265) Zečević, J.; de Jong, K. P.; de Jongh, P. E. *Curr. Opin. Solid State Mater. Sci.* **2013**, *17*, 115.
- (266) Sterrer, M.; Freund, H.-J. *Catal. Lett.* **2013**, *143*, 375.
- (267) Xu, Y.; Yang, J.; Demura, M.; Hara, T.; Hirano, T.; Matsushita, Y.; Tanaka, M.; Katsuya, Y. *Appl. Catal., A* **2014**, *478*, 165.
- (268) Park, C.; Fenter, P.; Sturchio, N.; Regalbuto, J. *Phys. Rev. Lett.* **2005**, *94*, 076104.
- (269) Blanchard, J.; Hervier, A.; Costentin, G.; Regalbuto, J.; Louis, C.; Boujday, S. *Catal. Today* **2014**, *235*, 245.
- (270) Hervier, A.; Blanchard, J.; Costentin, G.; Regalbuto, J.; Louis, C.; Boujday, S. *Chem. Commun.* **2014**, *50*, 2409.
- (271) Thüne, P. C.; Weststrate, C. J.; Moodley, P.; Saib, A. M.; van de Loosdrecht, J.; Miller, J. T.; Niemantsverdriet, J. W. *Catal. Sci. Technol.* **2011**, *1*, 689.
- (272) Prieto, G.; Shakeri, M.; de Jong, K. P.; de Jongh, P. E. *ACS Nano* **2014**, *8*, 2522.
- (273) Stephens, I. E. L.; Bondarenko, A. S.; Perez-Alonso, F. J.; Calle-Vallejo, F.; Bech, L.; Johansson, T. P.; Jepsen, A. K.; Frydendal, R.; Knudsen, B. P.; Rossmeisl, J.; Chorkendorff, I. *J. Am. Chem. Soc.* **2011**, *133*, 5485.